ISSN 1000-9620

Marine Science Bulletin

海洋通报

Volume 9 • Number 1 2007

ISSN 1000-9620

NATIONAL MARINE DATA AND
INFORMATION SERVICE OF CHINA

NOAA
U.S. NATIONAL OCEANIC AND ATMOSPHERIC ADMINISTRATION
DEPARTMENT OF COMMERCE

MARINE SCIENCE BULLETIN

Vol.9 No.1 May, 2007

LIBRARY
JAN 30 2008
National Oceanic & Atmospheric Administration
U.S. Dept. of Commerce

CONTENTS

A Numerical Study on the Effects of Orography During the Landfall Process of Typhoon Haitang ..... ZHANG Jianhai et al. (3)

The Study on the Localization of Acid Phosphatase Activity During Spermiogenesis in Chinese Mitten-Handed Crab, Eriocheir sinensis ..... LIU Guirong et al. (13)

Structural Determination of Three Sphingolipids from Two Marine-derived Mangrove Endophytic Fungal Strains ..... ZHU Feng et al. (20)

Study on Remote Sensing of Water Depths Based on BP Artificial Neural Network ..... WANG Yanjiao et al. (26)

Dinoflagellate Cysts Records from Core Samples of Modern Marine Sediment at the Luoyuan Bay Mouth ..... SUN Aimei et al. (36)

Development of Sedimentary Environment in the Northeastern South China Sea Since the Last Glacial Stage ..... HUANG Yuanhui et al. (46)

Influence of Seawall Line Choice on Tide Lock Drainage in Tidal Flat Inning —— Cangdongpian Inning Area on the west part of Tiaozini Sand as a case study ..... LI Jialin et al. (55)

Feasible Rate of Tidal Flat Reclamation —— Jiangsu Mud Coast as a Case Study ..... WANG Yanhong et al. (66)

Progress in Studies on the Equilibrium Shape of Headland-bay Shoreline ..... LI Zhilong et al. (74)

Identification Signs and Prospects of Hydrate Gas ..... XU Zhenzhong et al. (84)

LIBRARY
Pacific Islands Fisheries Science Center
NOAA Fisheries
Honolulu, Hawai'i

海 洋 通 报（英文版）

HAIYANG TONGBAO

2007 年 5 月 第 9 卷 第 1 期

目 次

台风 Haitang (0505) 登陆过程地形影响的数值模拟试验 …… 张建海 等 (12)

中华绒螯蟹精子形成过程酸性磷酸酶的分布特征 …… 刘桂荣 等 (19)

产自两株海洋真菌的三种鞘脂类的结构测定 …… 朱 峰 等 (25)

基于 BP 人工神经网络的水体遥感测深方法研究 …… 王艳姣 等 (35)

罗源湾口柱状沉积物中的甲藻孢囊 …… 孙爱梅 等 (45)

南海东北部末次冰期以来沉积环境演变的初步研究 …… 黄元辉 等 (54)

滩涂匡围海堤选线对邻近涵闸排水的影响分析

——以条子泥西侧岸滩仓东片匡围为例 …… 李加林 等 (65)

海岸滩涂围垦的适宜速度研究——以江苏淤泥质海岸为例 …… 王艳红 等 (73)

岬间海湾平面平衡形态研究进展 …… 李志龙 等 (83)

天然气水合物的识别标志及研究进展 …… 徐振中 等 (96)

A Numerical Study on the Effects of Orography During the Landfall Process of Typhoon Haitang

ZHANG Jianhai [1, 2], CHEN Hongmei [2], ZHU Xiaoming [2]

1. *Department of Atmospheric Sciences, Nanjing University of Information Science & Technology, Nanjing* 210044, *Jiangsu, China*

2. *Shaoxing Meteorological Bureau, Shaoxing* 312000, *Zhejiang, China*

Abstract: The landfall process of typhoon Haitang which affected East China seriously was simulated by using the MM5 model and the track, intensity, precipitation and structure of typhoon were successfully reproduced. Then through the sensitive test, the effects of terrain were analyzed. Results show that the irregular track during the period of typhoon passing through Taiwan and later landfalling at Fujian was in relation to the occurring and developing of orthographic impressed depression. The amount of rainfall was enhanced more than one time and the strength of typhoon was weakened 4 to 5 hPa. It is found that the effect of terrain on the structure of typhoon is limited at low level and is backward in space compared with the one at high level. In addition, the phenomenon that the equivalent temperature in the typhoon's moving direction inclines to the west on the eye of landfall may be concerned with the terrain.

Keywords: Typhoon Haitang; orographic effects; numerical experiments; structural change

Introduction

With the increasing model resolution and the perfecting physical processes development in recent years, numerical simulation appears to play an important role in the studies of landfall typhoon's interaction with topography. Progress in understanding the dynamics of typhoon circulation and its interaction with terrain has been made in the past decades through various observational studies and numerical simulations [1-4]. However, considerable detail of such an interaction is still not well understood, mainly due to major limitations both from lack of mesoscale observations that may provide a detailed description of the storms, and from lack of high resolution mesoscale model simulations that may offer insights into the mesoscale process responsible for the structural changes associated with the interaction of a typhoon with the mesoscale topography.

In this study, we used a well-developed mesoscale model MM5 to perform a real-case simulation of Typhoon Haitang (2005). Results are compared with observations to evaluate the capability of model in simulating the track, intensity, mesoscale wind, and precipitation distribution of Haitang during landfall. The effect of the Taiwan terrain on the evolution of Haitang is also investigated through different numerical experiments, with or without the Taiwan terrain. Section 2 describes the experimental design. Some

Received on April 10, 2006

observed features associated with Haitang and the model results are discussed in Section 3. The summary appears in Section 4.

1 Model description and experimental design

1.1 Model description

The model used in this case study is PSU/NCAR MM5 Model. The Fifth-Generation PSU/NCAR Mesoscale Model is the latest one in a series that has developed from a mesoscale model used by Anthes at Penn State in the early 1970s that was documented by Anthes and Warner (1978). Since that time it has undergone many changes designed to broaden its applications. These include (i) a multiple-nest capability, (ii) nonhydrostatic dynamics, and (iii) a four-dimensional data assimilation (Newtonian nudging) capability, (iv) increased number of physics options, and (v) portability to a wide range of computer platforms, including OpenMP and MPI systems.

1.2 Experimental design

To understand the evolution of Haitang and the effect of the Taiwan topography on Haitang, two 72-h model integrations were performed, starting at 0000 UTC, on July 18, 2005. As initial input data, this scheme uses the National Centers for Environmental Prediction (NCEP) global reanalysis data with a resolution of 1 degree as the first guess field of the model. The first experiment made a 72-h forecast using the PSU/NCAR MM5 model system. Experimental design uses a two-way nesting scheme, in which the coarse-grid distance is 60 km, and the fine-grid distance is 20 km, with the terrain data at the resolution of 10 minutes. Model central latitude and longitude are 29°N and 115°E respectively, the number of grid points in the parent domain is 77 × 94, and the number of grid points in the daughter domain is 106 × 97. The vertical structure of the model is of 23 sigma layers, and the pressure at the top of the model is 100 hPa. The Model physics includes two cumulus parameterization schemes described by Betts-Miller and Kain-Fritsch. The time step of integration is 90 seconds, and the model output frequency is 1 hourly. This experiment can be regarded as the control experiment, and also as a forecast since it was integrated based on the information available at the starting time. The second simulation excludes the Taiwan terrain to show the impact of the Taiwan topography on Haitang (Linear extrapolation was done at points under the terrain, while the hydrostatic relation is kept to obtain the new surface pressure). This experiment can be regarded as the sensitive experiment.

2 Results

2.1 Synopsis of Haitang

Typhoon Haitang was the 5th typhoon in the western North Pacific in 2005. According to the official report of National Meteorological Center, Haitang made the first landfall at Dongao, Taiwan at 0650 UTC on July 18, 2005, and crossed the northern half of Taiwan. After passing Taiwan, Haitang turned toward the northwest following a snaky track. Haitang made the second landfall at 0910 UTC on July 19, 2005 at

Lianjiang, Fujian. After landfall, Haitang moved west-northwest and crossed the northern and central half of Fujian, tracked inland over the mainland China, and gradually dissipated over land. The strong winds and heavy precipitation associated with the typhoon circulation occurred in Fujian and Zhejiang.

2.2 The control experiment and the sensitive experiment

2.2.1 Haitang's track

Fig. 1 shows the comparison of forecast track with the best track analysis from the National Meteorological Center. In general, the numerical experiments show fairly accurate track simulations for Haitang, though some position errors exist. These include: (i) the initialization fields are some degrees different from the observational analysis fields, which leads to the typhoon's position in the model atmosphere to the east of the observations. (ii) the typhoon's simulated landfall positions, with or without terrain, deviate to the south of the observed storm landfall position. (iii) as to the velocity forecast, the simulated storms move too fast compared with the observed storm's movement.

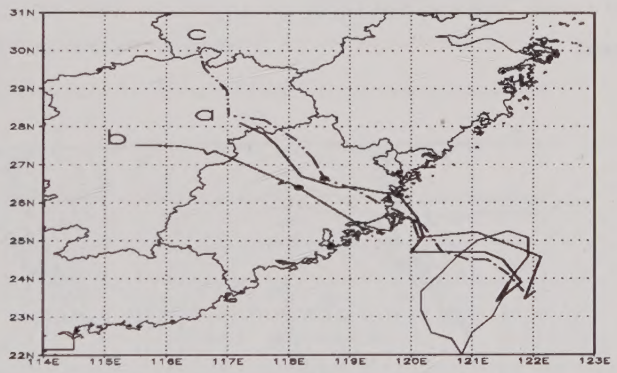

Fig. 1 Track of Typhoon Haitang (a. observated, b. terrain, c. no terrain, "•"location at 17:00, 19th)

In the comparison of the two experiments, the impact of topography on typhoon becomes more significant. In the observational analysis, Haitang's track is rather complicated and anomalous between its first landfall in Taiwan and its second landfall in Fujian. The control experiment shows a fairly accurate track simulation for Haitang. However, in the sensitive experiment, Haitang moved westwards regularly between 0000 UTC 18 July and its second landfall in Fujian, without the jumpings southwards, northwards, and westwards appearing in the observed storm track. After Haitang's second landfall in Fujian, in the control experiment the model track deviated to the south of the best track, while in the sensitive experiment the model track deviated to the north of the best track.

Fig. 2 shows the sea level pressure affected by terrain. In the comparison of the control experiment forecast track with the sensitive experiment model track, the significant difference is that the low level storm circulation separated into two vortex centers due to the Taiwan terrain. Since the subsidiary vortex center results from the Taiwan topography, it is named Topographic Influence Low [5]. Between 0000 UTC 18 July and 0300 UTC 18 July, Haitang moved southwards, however, the Topographic Influence Low

moved northwards, furthermore its intensity reinforced gradually. Nevertheless, the predominant vortex center moved southwards along the east coast of Taiwan. The analysis indicates that the two storm vortexes rotated around each other, but the intensity of the predominant vortex center was still greater than that of the subsidiary vortex center. Therefore, the moving direction of Haitang was still predominated by the predominant vortex center. Between 0300 UTC 18 July and 1200 UTC 18 July, Haitang moved northwards (Fig. 2b). The intensity of the subsidiary vortex center was almost equal to that of the predominant vortex center, still reinforcing, however, the predominant vortex center was weakened by the Central Mountain Range. Instead, the moving direction of Haitang was predominated by the Topographic Influence Low, and Haitang moved northwards. Between 1200 UTC 18 July and 2100 UTC 18 July, Haitang moved westwards (Fig. 2c). The predominant vortex center has been weakened too much and gradually dissipated. In place of the original predominant vortex center the Topographic Influence Low had become the new predominant vortex center, Haitang moved westwards. At 2100 UTC on 18 July, Haitang moved over the middle part of the Taiwan Straits, the influence of terrain attenuated and then the typhoon moved northwestward again. The comparison of the forecast track with the Taiwan terrain with the model track without the Taiwan terrain indicates that Haitang's anomalous track results from the Topographic Influence Low development.

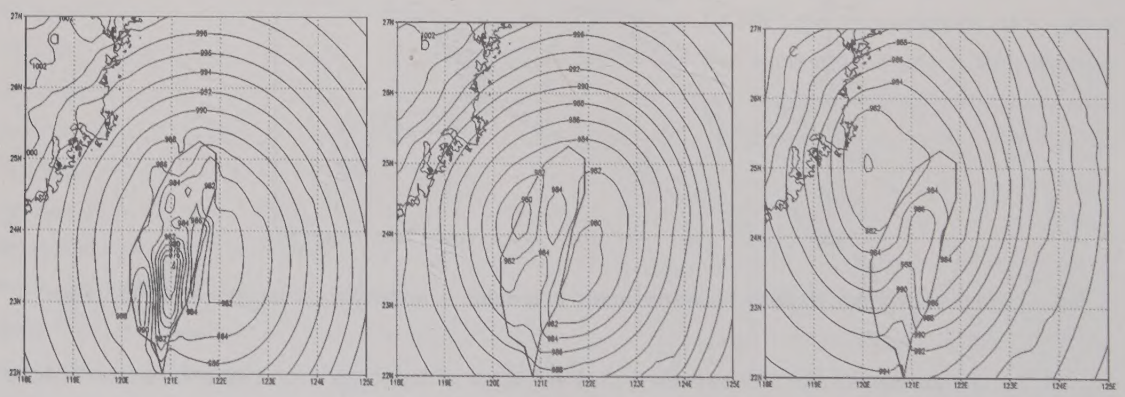

Fig. 2 Sea level pressure affected by terrain (a. at 08:00, b. at 11:00, c. at 20:00, 18 th, unit: hPa)

2.2.2 Haitang's intensity

Fig. 3 shows the variation of pressure of typhoon center. In general, findings from observational studies and numerical simulations are in agreement with each other, that is, the intensity of typhoon attenuated gradually. Nevertheless, in the first 36 h, the simulated storm center was much weaker than the observed center, which is consistent with the findings from the simulations by Fei (2003), Li (2004) [6, 7]. This error may be in part related to the NCEP reanalysis data resolution and the lack of ocean data. Using bogus can reduce the prediction error in the early stage of simulation, while the findings from observational studies and numerical simulations are in agreement with each other in the later stage of modeling.

Analysis of the variation of the typhoon intensity in simulations indicates that in the first 12 h, the intensity variations from the control experiment and the sensitive experiment were in agreement with each other, and the typhoon's intensity remained unchanged, however, its intensity attenuated a lot in the observational studies, that is, the vortex center pressure reinforced from 930 hPa to 955 hPa, which is induced by the intensity of typhoon in the model atmosphere weaker than in the observational studies. There was an adjustment to reduce the pressure to agree with the observed pressure in the initial integrating stage, which counterbalanced the intensity attenuation due to the terrain surface frictional dissipation. After 1200 UTC 18 July, the difference of intensity of typhoon between the control experiment and the sensitive experiment became significant, the intensity attenuation of the typhoon in the control experiment was 4-5 hPa, greater than that in the sensitive experiment, suggesting that terrain friction is an important factor in the gradual dissipation after typhoon's landfall.

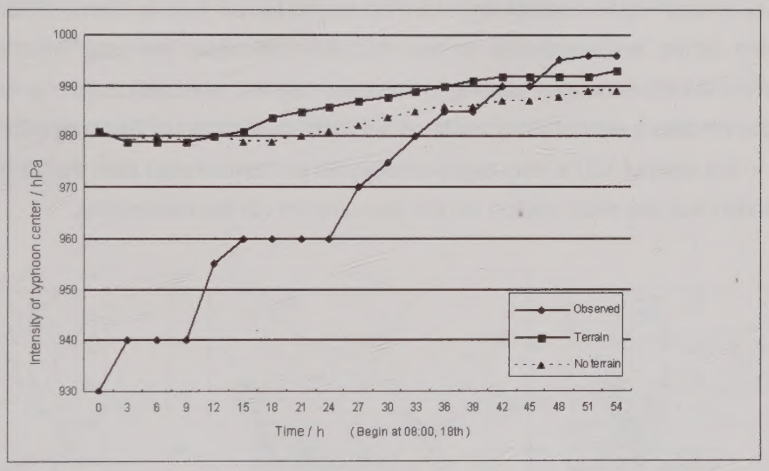

Fig. 3 Variation of pressure of typhoon center

2.2.3 Haitang's precipitation

From 0000 UTC 18 July to 0000 UTC 21 July, Typhoon Haitang affected Fujian and Zhejiang severely. Fig. 4 shows the comparison of the observed precipitation and the simulated precipitation in 72 h. In general, the findings about the extent of rainfall zone from the control experiment and the observational studies are in agreement with each other, that is, north-south direction. The two local rainfall maxima located to the north of the typhoon landfall position, but the intensity and location were some degrees different from the observed precipitation. The forecast rainfall center located to the north of the observed rainfall center by 0.5 degree, and the forecast amount of rainfall was smaller than the observed precipitation.

Comparing Fig. 4b with Fig. 4c, it was found that the rainfall distributions were still in agreement with each other, however, the rainfall intensities were quite different. In general, the rainfall balance distribution was in agreement with the correspondent terrain, that is, the heavy rainfall zone was correspondent to the

terrain of high altitude. The local rainfall maximum with terrain was much greater than that without terrain. The rainfall maximum was 450 mm with terrain, while 200 mm without terrain. However, there was nearly no difference between the two experiments to the west of 120°E, which showed that the terrain played a significant role in the enhancement of rainfall. On the other hand, compared with the sensitive experiment, the mesoscale structure of the rainfall was more significant in the control experiment. Fig. 4b shows that there were several rainfall centers of 100-200 mm in the precipitation zone. Fig. 5 shows the variation of simulated rainfall and topography along 28.4°N, suggesting that the rainfall distribution is in agreement with the terrain elevation distribution. On the windward side of the mountains, the amount of precipitation became large while the elevation increased. However, on the leeward side of the mountains, the amount of precipitation became small while the elevation increased. Comparison between the control experiment and the sensitive experiment shows that it was in the zone to the east of 120°E that there was great difference in the amount of precipitation, which was due to the Haitang's moving direction right across the mountains in Zhejing and Fujian coastal regions. The southeast air flow to the northeast of the typhoon center just located at the windward side of the southwest-northeast trending mountains. The terrain forcing lift intensified the condensation heating in the lower troposphere and updraft, and the warm-wet air flow uplifted on the windward side of the mountains led to the heavy rain in Zhejiang and Fujian. However, the precipitation to the west of 120°E was approximately 90 percent smaller than that to the east of 120°E. Therefore, the terrain was the main reason for the non-uniform rainfall distribution.

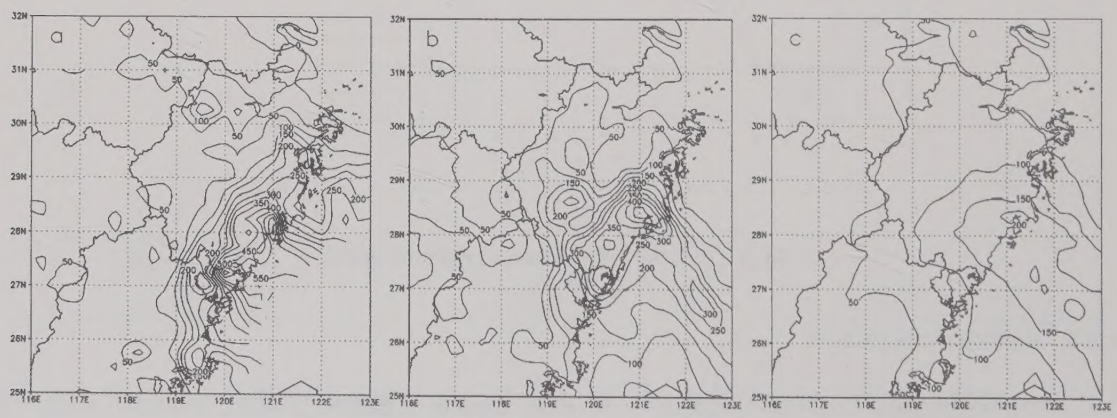

Fig. 4 Accumulative rainfall from 08:00, 18 th to 08:00, 21th (a. observed, b. terrain, c. no terrain, unit: mm)

2.2.4 The effect of Taiwan terrain on Haitang's mesoscale structure

2.2.4.1 Geopotential height field Fig. 6 shows the variation of geopotential height at 500 hPa and 925 hPa when Haitang passed Taiwan, with or without terrain, in the two experiments. At 0600 UTC 18 July, the geopotential height field had two features: (i) in the control experiment the low level storm circulation separated into two vortex centers induced by Taiwan terrain, which was consistent with the sea level pressure studies. However, the Topographic Influence Low only existed in the low level storm

circulation, not in the high level at 500 hPa. In the sensitive experiment there was no Topographic Influence Low, which could be explained by the terrain's interaction. Nevertheless, in the high level storm circulation, there was no significant difference between the two experiments, suggesting that the influence of Taiwan terrain on Typhoon's mesoscale structure only existed in the low level of the storm, which may be partly related to the elevation of the mountains. (ii) there were great differences between the control experiment and the sensitive experiment in the high-low level storm circulation centers. In the control experiment, the axis of high-low level centers inclined to the east while the elevation increased. The low level center of the storm was influenced by the Taiwan terrain, the predominant circulation of storm was prevented by the Taiwan Central Mountain Range, still located on the east coast of Taiwan, however, in the high level at 500 hPa, the circulation center had moved over Taiwan Island, which led to the low level vortex center falling behind the high level vortex center. In the sensitive experiment, the high-low level vortex centers moved nearly synchronously, furthermore the low level vortex center moved even faster. At 1200 UTC 18 July, the predominant vortex center to the east of the Central Mountain Range dissipated, and the Topographic Influence Low to the west of the Central Mountain Range became the new predominant vortex center. Typhoon Haitang jumped off Taiwan Island. The high-low level vortex centers gradually moved synchronously, which was consistent with the sensitive experiment.

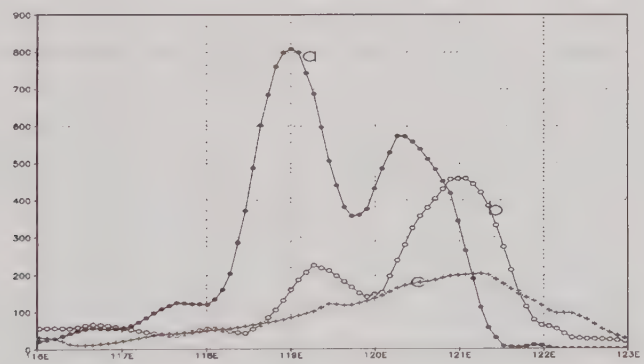

Fig. 5 Variation of simulated rainfall and topography along 28.4°N

(a. terrain, b. rainfall affected by terrain, c. rainfall not affected by terrain, height unit: m, rainfall unit: mm)

2.2.4.2 The variation of equivalent potential temperature According to the moist potential vorticity theory [8], under the moist potential vorticity conservation, due to the incline of plane of theta-e, the horizontal wind's vertical shear reinforces, which enhances the vertical vorticity. The more the plane of theta-e inclines, the faster the vertical vorticity reinforces, and the easier the storm rain will happen. Fig. 7 shows the vertical plane of theta-e from east to west at 0000 UTC 19 July. The feature is that there was a low index zone in the middle part of troposphere, and the low level storm center was correspondent to the high index zone, however, the high index zone located on both sides of the storm center asymmetrically, theta-e to the east of the storm center was higher than that to the west of the storm center. Comparison of the two experiments suggests that: (i) in the control experiment to the

east of the storm center (121-122°E), the high index of theta-e zone located at the level of 850 hPa, while in the sensitive experiment, the high index of theta-e zone located at below the level of 900 hPa, which indicated that convection in the control experiment was much severer than that in the sensitive experiment. It was the very place that was on the windward side of the mountain in which direction typhoon was moving. Terrain forced the warm-wet air into lifting up and the convective instability attenuated. (ii) in the sensitive experiment, before the typhoon landfall, the iso-theta-e near the west of the typhoon eye was thick, but did not incline to the west as it did in the control experiment, which indicated that the moist baroclinic reinforced much more slowly than that in the control experiment, which caused the intensity and structure of the typhoon to change slowly.

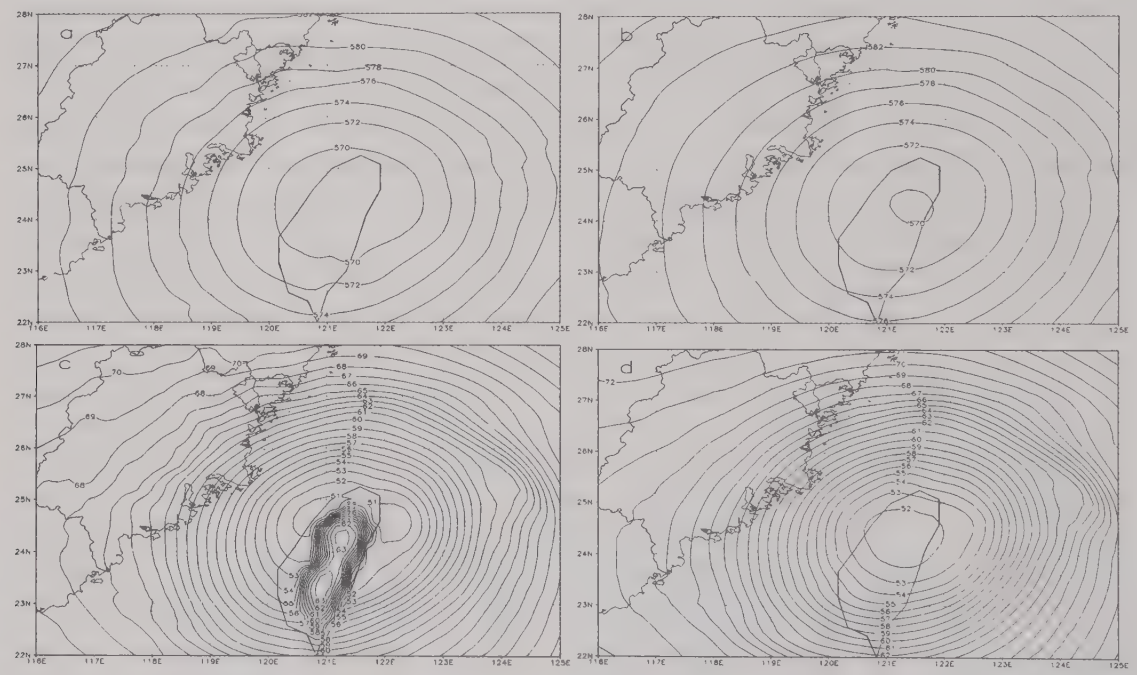

Fig. 6 Height fields at 14:00, 18 th

(a. 500 hPa, terrain, b. 500 hPa, no terrain, c. 925 hPa, terrain, d. 925 hPa, no terrain, unit: 10 gpm)

4 Summary

A real-case simulation of Typhoon Haitang (2005) using the PSU/NCAR MM5 Model is presented in this paper in simulating the track, intensity, precipitation and the mesoscale structure features of Haitang under the influence of topography. Studies on the impact of the Central Mountain Range on the evolution of Haitang experiments with or without the Taiwan terrain are also performed.

Typhoon Haitang's anomalous track during passing across Taiwan is related to the Topographic Influence Low's development to the west of Taiwan. When the Topographic Influence Low is weak, the

Typhoon's moving direction is predominated by the predominant vortex center to the east of Taiwan. When the Topographic Influence Low has become the new predominant vortex center, the typhoon's moving direction is predominated by the Topographic Influence Low, and then Typhoon Haitang jumped off Taiwan Island. For the typhoon landfalling in Fujian and Zhejiang, the mountains play an important role in intensifying the heavy storm rainfall. The influence of the terrain is not significant during the first 12 h, which becomes more significant in the later stage, and the intensity of attenuation of Typhoon is about 4-5 hPa induced by terrain.

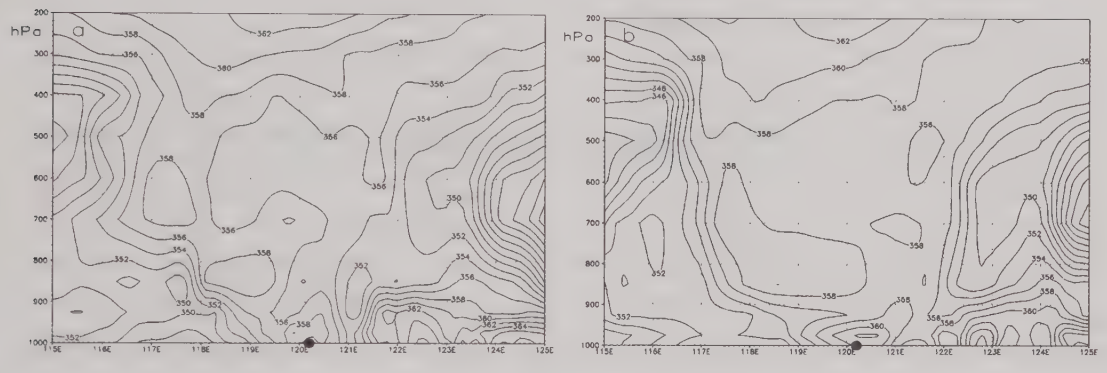

Fig. 7 Vertical plane of theta-e from east to west at 08:00, 19th
(a. terrain, b. no terrain, "●"center of typhoon, unit: K)

Under the influence of terrain, the low level vortex center separates into two vortex centers, but the high level vortex center remains unchanged, which is related to the elevation of the mountains. Typhoon's low level vortex center is prevented by the Central Mountain Range and falls behind the high level vortex center, which makes the axis of high-low level vortex centers incline to the east. After the typhoon departs Taiwan Island, the high-low level vortex centers move nearly synchronously again. When landfalling, under the impact of terrain the plane of iso-theta-e to the west of the typhoon eye becomes quite thick, and the plane of theta-e inclines to the west, which leads to the change of the moist baroclinic and vertical disability, which results in the variation of intensity and structure of Typhoon Haitang.

References

[1] Luo Zhenxian, Chen Lianshou. Effect of the Orography of Taiwan Island on Typhoon Tracks [J]. Scientia Atmospheric Sinica, 1995, 19(6): 701-706.

[2] Niu Xuexin, Du Huiliang, Liu Jianyong. The Numerical Simulation of Rainfall and Precipitation Mechanism Associated with Typhoon Sinlaku(0216) [J]. Acta Meteorologica Sinica, 2005, 63(1): 57-68.

[3] Yan Jinghua, Xu Jianping, Ding Weiyu, et al. A Modeling Study of the Impact of Terrain on the Intensity of Landfalling Tropical Cyclone Vongfong(0214) [J]. Scientia Atmospheric Sinica, 2005, 29(2): 205-212.

[4] Yan Jinghua, Dong Keqin. Numerical Simulation Study on the Effects of Taiwan Terrain on Typhoon Dot [J].

Journal of Tropical Meteorology, 1997, 13(3): 217-226.

[5] Yang Pingzhang, Wan Qiling, Du Huawu. Numerical Study on the Effects of Taiwan Terrain on Movement of Typhoon Dot [J]. Acta Oceanologica Sinca, 1996, 18(5): 22-29.

[6] Fong SoiKun, Wu Chisheng, Hao Ipan, et al. Numerical Prediction Experiment on Typhoon Maggie(9903) [J]. Acta Ocenologica Sinca, 2003, 25(4): 29-35.

[7] Li Jiangnan, Gong Zhepeng, Wang Anyu, et al. Numerical Experiments of the South China Sea Typhoon Vongfong(2002) [J]. Acta Scientiarum Naturalium Universitatis Sunyatseni, 2004, 43(3): 85-89.

[8] Wu Guoxiong, Cai Yaping. The Moist Potential Vorticity and the Development of Slantwise Vorticity [J]. Acta Meteorologica Sinica, 1995, 53(4): 387-404.

台风 Haitang(0505)登陆过程地形影响的数值模拟试验

张建海[1,2]，陈红梅[2]，诸晓明[2]

(1. 南京信息工程大学大气科学系，江苏 南京 210044；2. 绍兴市气象局，浙江 绍兴 312000)

摘 要：以 2005 年严重影响我国的登陆台风 Haitang 为研究对象，在用 MM5 模式成功模拟台风登陆前后路径、强度、降水以及结构特征的基础上，通过地形敏感性试验，分析了地形对台风的影响及其机理。结果表明：台风在经过台湾及其后在福建登陆期间的异常路径是地形诱生低压发生发展的结果；在降水强度上东部沿海特殊地形对台风北侧东南气流的辐合抬升使得暴雨增幅度 1 倍以上；地形对台风强度也有一定影响，约为 4 ～ 5 hPa。通过对有无地形影响时台风结构的比较发现地形影响主要在低层，使得高度场分裂两个中心，低层台风主体受山脉阻挡在位置上落后于高层。分析还发现台风登陆前夕移动方向西侧相当位温向西倾斜也可能与地形有关。

关键词：Haitang 台风；地形影响；数值模拟；结构变化

The Study on the Localization of Acid Phosphatase Activity During Spermiogenesis in Chinese Mitten-Handed Crab, *Eriocheir sinensis*

LIU Guirong, KANG Xianjiang, GUO Mingshen, SUN Wenjia, WANG Qi

College of Life Science, Hebei University, Baoding 071002, *Hebei, China*

Abstract: Ultrastructural cytochemical techniques and electron microscopy were used for localization of acid phosphatase activity during spermiogenesis in *Eriocheir sinernsis.* The results showed that: Acid phosphatase was synthesized in the endoplasmic reticulum in the early spermatids. The acid phosphatase was found gradually in nucleus, the membrane of acrosomal vesicle, the cytoplasmic region and the acrosomal tubule. And then the reaction product particles became thicker during the spermiogenesis. In the mature sperm, acid phosphatase was localized in the percutor organ slightly, but it was massive and compact in the acrosomal tubule.

Keywords: Spermiogenesis; Acid phosphatase; *Eriocheir sinensis*

Introduction

Eriocheir sinensis belongs to Subphylum Crustacea, Class Malacostraca, Order Decapoda, Suborder Pleocyemata, Infraorder Brachyura, Superfamily Grapsoidea. The detailed studies on the sperm ultrastructure, acrosomal reaction, and fertilization have been reported [1-3]. But the report on the distribution of acid phosphatase in the reproductive cells during *E. sinensis* spermiogenesis has not been reported. Acid phosphatase (ACPase (EC.3.1.3.2)) is one of the most imporment enzymes which catalyze hydrolyzing of phosphate mono-ester and producing phosphoric acid. Acid phosphatase has a close relation with phosphorus metabolism and substance metabolism. It is also a marker enzyme of lysosome in cell [4]. During spermiogenesis, some important events occur, such as the change of organelles, the modifing and degradation of biomacromolecule. The acid phosphatase plays an important role in these events.

E. sinensis is a transitional form of in vitro fertilization and in vivo fertilization, with eggs adhering sperm in vivo and fertilizing in vitro. Therefore, the research on the localization of acid phosphatase during spermiogenesis of *E. sinensis* is meaningful. A preliminary study on the distribution of acid phosphatase during spermiogenesis of *E. sinensis* was reported in this paper, in order to offer basic data for the function of acid phosphatase duing spermiogenesis, and the appraisal of the sperm quality.

Received on June 5, 2006

1 Material and methord

1.1 Material

The male *E. sinensis* was bought from the Fuhe market in Baoting, held in fresh water for two days. The testes, vas deferens and seminal visicle were dissected out immediately .

1.2 Methord

Gomori reaction [5].

Fix: Small pieces of above three tissues about 0.5 mm^3 in diameter were fixed at 4 ℃ for 1 h in 2 % paraform and 2.5 % glutaraldehyde buffer in 0.1mol·L^{-1} Sodium Cacodylate and 8 % sucrose buffer at pH 7.3, and washed three times in 0.1 mol·L^{-1} Sodium Cacodylate containing 8 % sucrose buffer at pH 7.3.

Incubate: The pieces were incubated at 37 ℃ for about 40 min. In the experimental group, the incubation buffer containing β-Sodium Glycerophosphate served as substrate. On the contrary, the incubation buffer in the control group had no subtrate.

Postfix and embed: After several times of washing in 0.1 mol·L^{-1} Sodium Cacodylate containing 8 % sucrose buffer at pH 7.3, the samples were postfixed in 1 % osmium tetroxide in 0.1 mol·L^{-1} Sodium Cacodylate for 30 min. rinsed in 0.1 mol·L^{-1} Sodium Cacodylate containing 8 % sucrose buffer, dehydrated in a series of increasing concentration of ethyl alcohol, and finally embedded in Epon812. Ultramicrocutted, observed with JEM-100SX, taken pictures.

2 Results

2.1 The distribution change of acid phosphate during spermiogenesis

In the early spermatid: Acid phosphatase distributed on the membrane of endoplasmic reticulum vesicle irregularly. The Gomori reaction was negative in nucleus, indicating there was no acid phosphatase (Plate Ⅰ: 1, 2). The Gomori reaction was negative in the control group.

In the late spermatid: There was acid phosphatase in the nucleus, acrosomal tubules, the membrane of acrosomal vesicle and the cytoplasmic region. There were uniform and compact metal granules distributing in acrosomal tubules, the membrane of acrosomal vesicle and in the cytoplasmic region, but there were less in the percutor organ of the acrosomal tubules, and the granules were most refined and compact. The metal granules located in nucleus were uniform and sparse, and their diameter was large, There were no acid phosphase in the fibrous layer, middle layer and lamellar structure of the acrosomal vesicles (Plate Ⅰ: 3, 4). Acid phosphase did not appear in the control group.

Along with the development of sperm, the metal granules congregated to uniform and large granules located in nucleus and acrosomal tubules. There was little granule in the percutor organ all the time. The

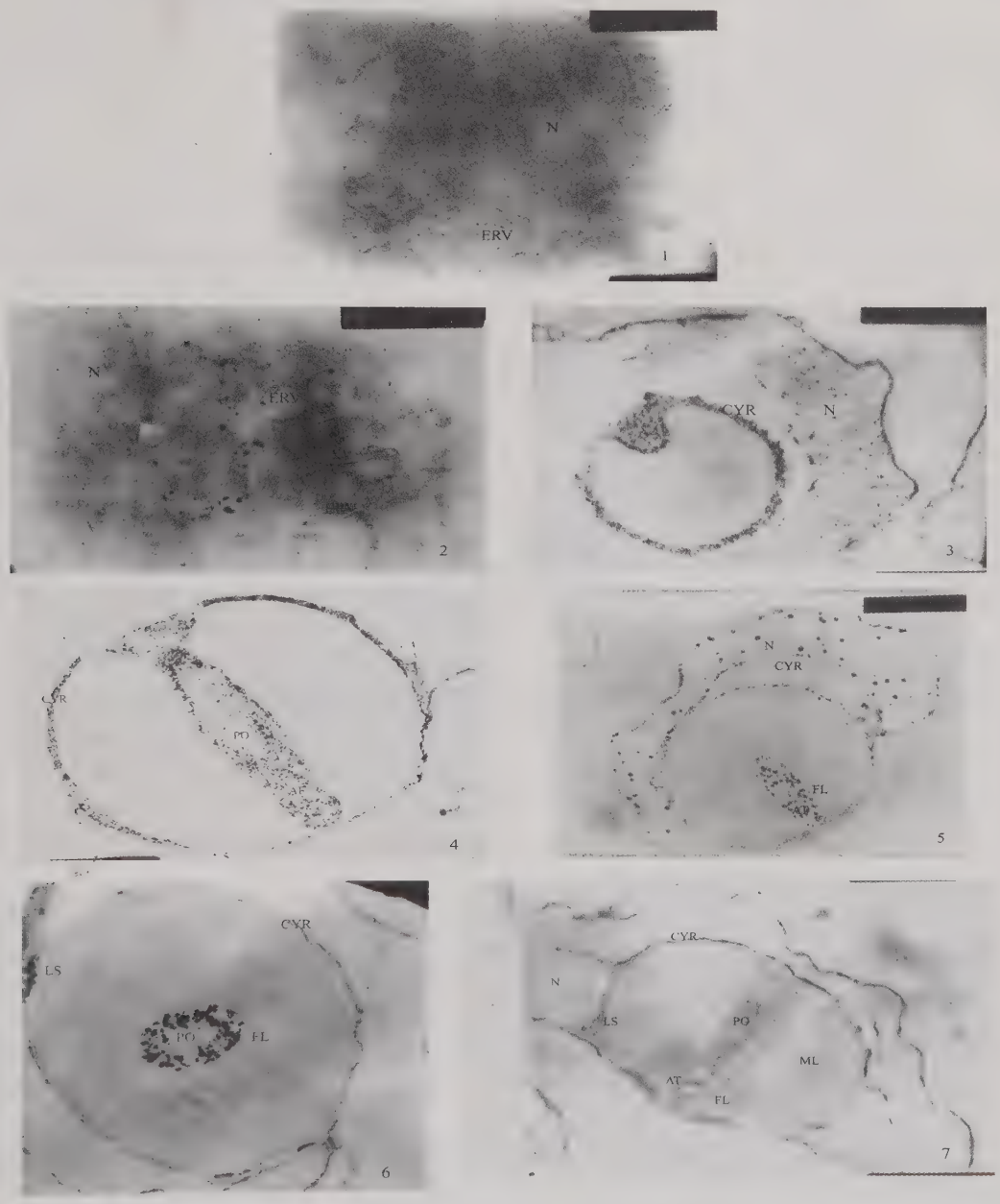

Plate Ⅰ Location of acid phophatase during spermiogenesis of *Eriocheir sinensis*

1, Acid phophatase located in the endoplastic reticulum vesicles of early spermatid×15 000;

2, A magnified part of early spermatid, showing endoplastic reticulum vesicles×25 000;

3, 4, 5, The location of acid phophatase of late spermatid×20 000 ×20 000 ×15 000;

6, The location of acid phophatase of mature sperm×15 000; 7, Mature sperm in the control group×15 000;

AT - acrosomal tubule; CYR - cytoplasmic region; ERV - endoplasmic reticulum vesic;

FL - fibrous layer; LS - lamellar structure; N - nucleus; PO - percutor organ

Gomori reaction was still negative in the fibrous layer, middle layer and lamellar structure of the acrosomal vesicle (Plate Ⅰ: 5). There was no metal granule in the control group either.

2.2 Distribution of acid phosphatase in mature sperm

Refer to Fig. 1 [6] which displays the mature sperm. There was little cytoplasm in the sperm. Organelles have also degenerated, and some even disappeared. Only a thin cytoplasmic region left between the nucleus and acrosome. There were no acid phosphatases in the cytoplase region.

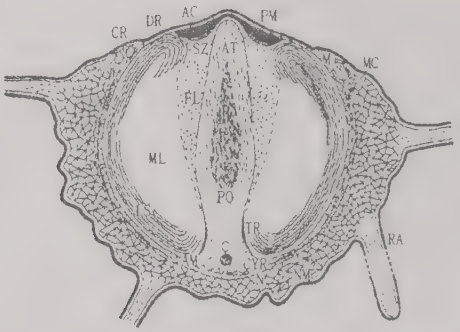

Fig. 1 Diagram of longitudinal section of the *E. sinensis* spermatozoa

AC. apical cap, AM. acrosomal membrane, AT. acrosomal tubules, C. centriole, CR. Convex ring, CYR. cytoplasmic region, DR. ditch ring, FL. Fibrous layer, LS. lamellar structure, M. mitochondria, MC. membrane complex, ML. middle layer, N. nucleus, NM. nuclear membrane, PM. plasma membrane, PO. percutor organ, RA. radial arm, SZ. subcap zone, TR. thickened ring.（Du.1999）

The main part of the sperm was occupied by the nucleus and acrosome. The shape of nucleus was unique and named nuclear cup, located in the behind part of sperm. Acid phosphatase was not observed in the nucleus.

Acrosomal vesicle was situated in the nuclear cup. It consisted of apical cap, acrosomal tubules and acrosomal vesicle.

a) Apical cap Apical cap is the head part with high election density. And there was no distribution of acid phosphatase.

b) Acrosomal tubule Acrosomal tubule was formed by the prolongation of the invaginated retral membrane of the acrosomal vesicle. It was filled with thread-like material. The percutor organ is in the middle part of the acrosomal tubule, formed by high election density canaliculus. The experiment result indicated that there were sporadic and thin metal granules in the percutor organ. All these showed that there was little acid phosphatase in the acrosomal tubule. There were many large and dense metal granules. That is to say, there was acid phosphatase in the other part of acrosomal tubule.

c) Acrosomal vesicle From inside to outside, the matter circling acrosomal tubules in the

acrosomal vesicle was divided into three parts: fibrous layer, middle layer and lamellar structure. Our experiment showed that there was no acid phosphatase in the three parts of acrosomal vesicle in mature sperm. (Plate Ⅰ: 6). There was not acid phosphatase in the control group (Plate Ⅰ: 7).

3 Discussion

3.1 Productive and operational mechanism of acid phosphatase

Pochon-Masson in 1983 pointed out: It is the main character of Decapoda Crustacea sperm that the rough endoplasmic retidulum replaces the Golgi apparatus to form the acrosome [7]. In the early period of *E. sinensis* spermiogenesis, Gomori reaction was positive in endoplasmic reticulum vesicles, which indicated acid phosphatase might be synthesized in the endoplasmic reticulum vesicle. Fernandes and Báo studied in 1999 the distribution of acid phosphatase in phytophagous bug sperm. They pointed out that acid phosphatase wasn't observed in the proacrosomal vesicle, they were absorbed in nucleus by the shrink of some vesicles and increased gradually. In the mature sperm, Gomori reaction products redistributed, and finally located in the acrosomal vesicle in a concentrated way. But the mechanism of acid phosphatase synthesis was different. It was synthesized in the Golgi apparatus [8]. The result revealed that acid phosphatase was synthesized in the endoplasmic reticulum. The endoplasmic reticulum was vesicle-shaped throughout the spermiogenesis of *E. sinensis.* And the pyknotic round granules, which were produced by rough endoplasmic reticulum vesicles in early spermatid, participated in forming the acrosome [9].

3.2 Acid phosphatase and nucleus

In the nucleus of middle and late spermatid during spermiogenesis of *E. sinensis*, Gomori reaction was positive. We conjectured that the acid phosphatase proenzyme was synthesized in the endoplasmic reticulum in the early spermatid stage, and transported from the cytoplasm to the nucleus, and then acid phosphatase zymogens were activated by a specific signal. The regulating action of enzyme to gene was usually fulfilled by phosphorylation and dephosphorylation. Acid phosphatase in the nucleus could regulate gene expression through activating or inhibiting some key enzymes related with the gene expression.

Furthermore, the mature sperm nucleus was nonconcentrated except *Nephrops* and *Homarus* in Decapoda. Researches proved that the genetic material in the nucleus was not integrated with basic proteins (histone or protamine) [10]. Our study discovered that there were basic proteins in prophase and metaphase, but not in the mature sperm nucleus during *E. sinensis* spermateteosis. It was reckoned that there was a nucleus-cytoplasm transfer of basic proteins. In 1967, Chevaillier studied the basic proteins during spermiogenesis of *Nephrops norvegicus*, *Eupagurus bernhardus* and *Carcinus maenas*. His results showed that histone, which filled in the nucleus during spermiogenesis, appeared in the mature sperm cytoplasm. These histones were free histones, rich in arginine in some part [11]. The acid phosphatase, appearing in middle and late spermatid nucleus during *E. sinensis* spermiogenesis, was maybe concerned with the transfer of basic proteins in the nucleus during spermiogenesis. This function was fulfilled by the

action of phosphorylation and dephosphorylation on basic proteins.

3.3 Acid phosphatase and acrosmal reaction

When the egg is still in the female *E. sinensis*, the acrosome of sperm clinging on the egg elongates, the apical cap heaves and the front of it dehisces also [2]. The acrosmal reaction of *E. sinensis* is approximately divided into two phases. The first phase, the acrosomal vesicle evaginates, and the inside material is released. After ovulation, the nuclear cup shrinks and oppresses the acrosomal vesicle, the middle part of fibrous layer, middle layer and lamellar structure evaginate in turn, and form the evagination vesicle. In succession, the membrane of acrosome and plasmic membrane disrupt, the inclusion of evagination vesicle, like egg membrane lysin, releases in order to dissolve the egg membrane. The second phase, the acrosmal tubule extends. After the two phases, the shape of *E. sinensis* sperm is the simplest. After the sperm gets into the egg, the acroamal tubule extends sequentially, contacts with the egg membrane, and the sperm and the egg membrane fuse at last. The acrosomal tubule brings the nucleus material into the egg, and the acrosomal reaction before fertilization is finished [3, 12, 13].

In the first phase, the fibrous layer goes through the slit pores of acrosomal membrane and plasmic membrane, forming a pore, and the material in the middle layer is released to lyze the egg membrane. In the second phase, the percutor organ elongates, contacts and fuses with the egg membrane, and spurs the cytoplasm band and nuclear material into the egg. It is reckoned that the acid phosphatase occupying the acrosomal tubule, is related with the lysis of egg membrane, the formation of masnulonucleus, and egg activation.

Acknowledgements

The project was supported by the National Natural Science Fund (30371115) and the Hebei Province Natural Science Fund (303118).

References

[1] Du N S, Lai W, Xue L Z. Studies on the sperm of chinese mitten-handed crab, *Eriocheir sinensis* (Crustacea, Decapoda) Ⅰ. The morphology and ultrastructure of mature sperm. Oceanologia et limnologia sinica, 1987, 18(2): 119-125.

[2] Du N S. The fertilization biology of chinese mitten-handed crab, *Eriocheir sinensis* (Crustacea, Decapoda) (1). Biology bulletin, 1998, 33(12): 5-8.

[3] Du N S. The fertilization biology of chinese mitten-handed crab, *Eriocheir sinensis* (Crustacea, Decapoda) (2). Biology bulletin,1998, 34(1): 10-12.

[4] Yukio Y, Eizo N, *et al*. Comparative studies on particulate acid phosphatases in sea urchin eggs. Comp. Biochem. Biophys., 1982, 71B: 563-567.

[5] Gomori G. In Microscopic histochemistry. Principles and practice. Chicago: University of Chicago Press. 1952, 189.

[6] Du N S, Lai W, Chen L Q, Xue L Z, Li T W, Wang L. Studies on the comparative ultrastructure of crab spermatozoa (Crustacea, Decapoda, Reptantia, Brachyura). Zoological Research, 1999, 20(5): 372-378.

[7] Pochon-Masson J. Arthropoda-Crustacea. In: Reporductive Biology of Invertebrates, Vol. Ⅱ: Spermatogenesis and Sperm Function[M]. Adiyodi, KG, Adiyodi, RG, ed. John Wiley & Sons Ltd.,1983, 407-449.

[8] Fernandes A P, Báo S N. Ultrastructural localization of enzymatic activity during spermiogenesis in two phytophagous bugs (Hemiptera: Pentatomidae). Tissue & Cell, 1999, 31(3): 349-356.

[9] Kang X J, Wang S A. Acrosomal formation and nuclear variation during spermatogenesis in Decapoda, Crustcen. Chinese Journal of Zoology, 2000, 35(4): 35-38.

[10] Chevaillier P. DNA-histone relations during spermatogenesis of Decapoda Crustaceans. C R Seances Soc Biol Fil, 1967, 161(2): 435-436.

[11] Chevaillier P. Development of nuclear and cytoplasmic constituants during spermatogenesis in Crustacea Decapoda. C R Acad Sci Hebd Seances Acad Sci D, 1969, 269(22): 2 251-2 253.

[12] Du N S, Lai W, Xue L Z. Acrosome reaction of the sperm in the Chinese mitten-handed crab,*Erioceir sinensis* (Crustacea, Decapoda). Acta zoological sinica, 1987, 33(1): 8-13.

[13] Wang Y L, Li S J. Zhang Z P. Overview of the research on the fertilization biology in Decapoda. Chinese Journal of Zoology, 1998, 33(5): 45-51.

中华绒螯蟹精子形成过程酸性磷酸酶的分布特征

刘桂荣，康现江，郭明申，孙文佳，王琦

(河北大学生命科学学院，河北 保定 071002)

摘 要：将金属盐法与光镜、电镜技术相结合，研究中华绒螯蟹精子形成过程中酸性磷酸酶分布的变化。研究表明，在精子形成的早期，酸性磷酸酶由细胞质中的内质网小泡上产生，随后出现在细胞核内、顶体囊膜上及顶体管内，并且反应产物逐渐由分布均匀的细密颗粒聚集成分布均匀的较大的颗粒；当精子成熟后酸性磷酸酶均匀分布在顶体管中，反应产物颗粒比较大，穿孔器部分发现有少量酸性磷酸酶分布。

关键词：生物化学；精子发生；酸性磷酸酶；中华绒螯蟹

Structural Determination of Three Sphingolipids from Two Marine-derived Mangrove Endophytic Fungal Strains

ZHU Feng[1], Chen Guangying[2], LIN Yongcheng[3]

1. *Department of Chemistry & Chemical Engineering, Foshan University, Foshan* 528000, *Guangdong,China;*
2. *Department of Chemistry, Hainan Normal University, Haikou* 571158, *Hainan, China;*
3. *School of Chemistry & Chemical Engineering, Zhongshan University, Guangzhou* 510275, *Guangdong, China*

Abstract: A set of three sphingolipids, *N*-2'-hydroxypalmitoyl-1-*O*-β-D-glucopyranosyl-9-methyl-4*E*, 8*E*-sphingadiene (A), *N*-2'-hydroxyl-3'*E*-octadecenoyl-1-*O*-β-D-glucopyranosyl-9-methyl-4*E*, 8*E*-sphingadiene (B) and *N*-palmitoyldihydrosphingosine (C), were isolated from two marine-derived mangrove endophytic fungal strains (strains No. 1924 and 3893) from the South China Sea. Their structures were elucidated by 2D NMR and FABMS methods. It is the first time that these sphingolipids were separated and obtained from marine-derived mangrove endophytic fungus from the South China Sea.

Keywords: marine fungus; metabolite; sphingolipid

Introduction

Marine microorganisms have been clearly demonstrated as a new source of novel natural products [1]. Marine fungus, as a group of marine microorganisms, has more and more attention. Recently, a lot of novel structures were found continuously from marine fungus [2-4]. Mangrove is a usually general term for a kind of arbor trees and shrubs living at the tide zones. It was reported that most described marine fungi could be found from mangroves. In the course of screening for novel structures from marine fungi, we examined firstly the metabolites of two marine-derived mangrove endophytic fungi (strains No. 1924 and 3893) from the South China Sea, and three sphingolipids were isolated from the mycelia extracts of these two strains. Their structures were elucidated as *N*-2'-hydroxypalmitoyl-1-*O*-β-D-glucopyranosyl-9-methyl-4*E*, 8*E*-sphingadiene (A), *N*-2'-hydroxy-3'*E*-octadecenoyl-1-*O*-β-D-glucopyranosyl -9-methyl-4*E*, 8*E*-sphingadiene (B) and *N*-palmitoyldihydrosphingosine (C) respectively, by 2D NMR and FABMS methods (seen in Fig. 1).

1 Experimental section

1.1 Instruments and reagents

Instruments: a Varian Inova 500NB NMR spectrometer, a VG-ZAB-HS mass spectrometer, a Bruker VECTOR 22 FT-IR spectrometer, a Shimadzu UV-2501PC spectrophotometer, and an Elementar Vario EL

Received on December 4, 2005

CHNS-O elemental analyzer.

Reagents: glucose (BR), peptone (BR), yeast extracts (BR), crude NaCl (used for microorganism culturing), the other reagents (AR).

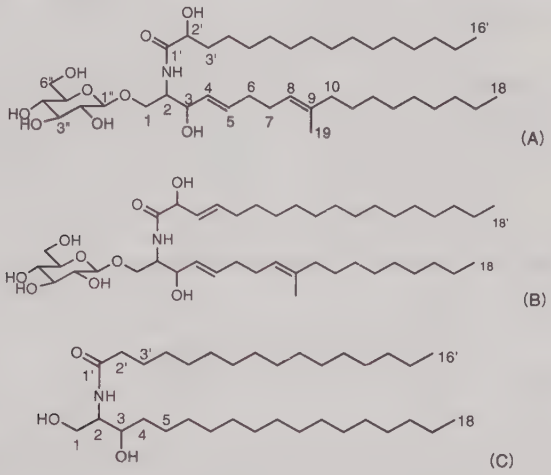

Fig. 1 Structures of compounds A~C

1.2 Fungal strain

Endophytic fungal strain No. 1924 / No. 3893 was isolated from a dropper / leaf of *Kandelia candel*, which is a mangrove plant from an estuarine mangrove in Hong Kong. All these fungal strain did not form spora and species were unidentified. The fungal strains were provided by Professor L L P Vrijmoed and Professor E B G Jones.

1.3 Culture conditions

Fungal strain No.1924 was cultured by industrial fermentation in 300 L of GYP media (glucose 1.2 %, yeast extracts 0.1 %, peptone 0.2 %, NaCl 0.3 %, pH 7.0) at 25 ℃ for 7 days.

Fungal strain No. 3893 was cultured at the static state in laboratory in 160 L of GYP media (glucose 1 %, yeast extracts 0.1 %, peptone 0.2 %, NaCl 0.35 %, pH 7.0) at 25 ℃ for 15-19 days.

1.4 Extraction and separation of metabolites

The cultures were filtered through cheesecloth. The mycelia were dehydrated by pressing and dried by air. The dried mycelia were extracted five times by soaking with an equal volume of methanol. The combined extracts were chromatographed on silical gel using a gradient elution from petroleum to ethyl acetate [5]. Compounds A (0.2 g) and C (30 mg) were obtained from the extracts of the mycelia of fungal strain No. 1924, and Compound B (0.15 g) was obtained from the extracts of the mycelia of fungal strain No. 3893.

1.5 Experimental data of compounds

Compound A: white threadlike solid, mp 184-186 ℃ (reference data [2]: 180-190 ℃); for NMR data, see Table 1; IR(KBr)*v*: 3401(br), 2921, 2852, 1641, 1542, 1466, 1382, 1081, 962, 900, 720, 612 cm^{-1}; FABMS *m/z*: 750 $[M+Na]^+$, 710$[M-H_2O+H]^+$, 548, 530, 496, 294, 257; Anal. calcd for $C_{41}H_{77}NO_9 \cdot 1.2H_2O$: C 65.68, H 10.28, N 1.869; found C 65.62, H 10.54, N 1.869.

Compound B: white threadlike solid, mp 170-172℃ (reference data[2]: 159-169 ℃), $[\alpha]_D$ +20.0°(*c* 0.055, CH_3OH), for NMR data, see Table 1; IR (KBr)*v*: 3432, 3334, 3192, 2924, 2853, 1640, 1615, 1454, 1401, 1165, 1079 cm^{-1}; UV (CH_3OH)λ_{max}: 215, 253 nm; FABMS (*m/z*): 776 $[M+Na]^+$, 736 $[M-H_2O+H]^+$, 574, 556, 538, 294, 280.

Compound C: white pellet solid, mp 96 ~ 100℃; for NMR data, see Table 1; FABMS *m/z*: 540 $[M+H]^+$, 341, 301, 257.

2 Results and discussion

Compound A has the molecular formula of $C_{41}H_{77}NO_9$ determined by FABMS (*m/z*) 750 $[M + Na]^+$ and elemental analysis. The numbers of hydrogen and carbon atoms in the ^1H and ^{13}C NMR spectra were in agreement with the molecular formula. The molecular formula suggested the presence of four unsaturated degrees.

The IR absorptions of Compound A at 1641 and 3401 cm^{-1} showed the presence of amide functionality and confirmed by the signals at ^1H and ^{13}C NMR spectra [δ_C173.6(s), δ_H7.34(d, 9.5Hz, NH)]. Thus one unsaturated degree was explained. In the ^1H and ^{13}C NMR spectra, there were some signals of two double bonds atδ_C134.8(s), 130.9 [d, 2×CH,δ_H 5.59 (tt, 15.5, 6.5, 1H) and 5.40 (dd,15,6.5Hz,1H)] and 123.4 [d,δ_H 5.10 (m,1H)]. Thus another two unsaturated degrees were explained. The remaining one unsaturated degree explained the presence of a ring.

The ^1H and ^{13}C NMR spectra for Compound A displayed resonances typical of glycosphingolipid. The signals in the ^1H and ^{13}C NMR spectra exhibited the presence of a number of carbinol atoms. Especially the occurring of signal of an anomeric carbon at δ_C103.4 (d) and δ_H 4.12 (d, 7.5Hz, 1H), suggested Compound A had a glucopyranosyl. The existence of glucopyranosyl was further confirmed by the peak at *m/z* 548 $[M-H_2O-163+2H]^+$ in the FABMS. In addition, the ^1H and ^{13}C NMR signals also suggested the presence of three methyls. One methyl [δ_C15.6(q),δ_H 1.54(s, 3H)] was linked to a carbon in a double bond, the other two overlapped [δ_C13.8(q),δ_H 0.85(t, 6.5Hz, 6H)], indicating the presence of two long aliphatic chains.

The structure of Compound A was established as Fig. 1 (A) through extensive analysis of FABMS and 2D NMR spectra data, including COSY, HMQC and HMBC experimental methods, and further confirmed by comparison with the NMR data derived for cerebroside B [6], which possessed the antifungal activity of aculeacin.

Tab. 1 NMR data of compounds A~C

C#	A		B		C	
	δ_C[a]	δ_H[m, J(Hz)][b]	δ_C[a]	δ_H[m, J(Hz)][b]	δc[a]	δ_H[m, J(Hz)][b]
1	68.6(t)	3.91(dd, 10.5, 5.5) 3.53(dd, 10.5, 4.0)	68.5(t)	3.92(dd, 10.5, 6.0) 3.53(dd, 10.5, 4.5)	60.9(t)	3.48(m)
2	52.8(d)	3.81(m)	52.9(d)	3.79(m)	54.9(d)	3.57(m)
3	70.5(d)	4.00(dd, 12.5, 6.5)	70.5(d)	3.99(dd, 12.0, 6.0)	70.1(d)	3.39(m)
4	130.9(d)	5.40(dd, 15.5, 6.5)	130.8(d)	5.38(dd, 15.5, 6.5)	↑	↑
5	130.9(d)	5.59(tt, 15.5, 6.5)	130.8(d)	5.44(dd, 15.5, 6.0)	I	I
6	27.3(t)	1.99(m)	27.3(t)	1.95(m)	I	I
7	31.2(t)	1.99(m)	31.2(t)	1.95(m)	33.2-21.7(t)	1.26(br s)
8	123.4(d)	5.10(m)	123.4(d)	5.09(m)	I	I
9	134.8(s)	-	134.8(s)	-	I	I
10	38.9(t)	1.92(t, 7.5)	38.9(t)	1.95(m)	I	I
11-17	34.4-22.0(t)	1.26(br s)	32.0-22.0(t)	1.26(br s)	↓	↓
18	13.8(q)	0.85(t, 6.5)	13.8(q)	0.85(t, 6.0)	13.5(q)	0.85(t, 6.5)
19	15.6(q)	1.54(s)	15.6(q)	1.54(s)	-	-
1'	173.6(s)	-	171.9(s)	-	171.8(s)	-
2'	71.0(d)	3.81(m)	71.9(d)	4.30(m)	35.3(t)	2.04(m)
3'	↑	↑	129.0(d)	5.58(dddd, 15.5, 6.5, 5.5, 5.5)	↑	↑
4'	34.4-22.0(t)	1.26(br s)	123.4(d)	5.67(dddd, 15.5, 7.5, 7.5, 1.5)	33.2-21.7(t)	1.26(br s)
5'-15'	↓	↓	↑	↑	↓	↓
16'	13.8(q)	0.85(t, 6.5)	32.0-22.0(t)	1.26(br s)	13.5(q)	0.85(t, 6.5)
17'	-	-	↓	↓	-	-
18'	-	-	13.8(q)	0.85(t, 6.0)	-	-
1"	103.4(d)	4.11(d, 7.5)	103.4(d)	4.12(d, 8.0)	-	-
2"	73.3(d)	2.96(m)	73.3(d)	2.96(m)	-	-
3"	76.5(d)	3.13(m)	76.5(d)	3.14(m)	-	-
4"	70.0(d)	3.23(m)	70.0(d)	3.23(m)	-	-
5"	76.8(d)	3.09(m)	76.8(d)	3.06(m)	-	-
6"	61.0(t)	3.66(m); 3.43(m)	61.0(t)	3.66(m)	-	-

a) Spectra recorded in DMSO-d_6 at 325 MHz. b) Spectra recorded in DMSO-d_6 at 500 MHz. Assignments on the basis of DEPT and HMQC experiments.

In Compound A, the geometry of the C-4/C-5 double bond was determined to be *trans* by the large vicinal coupling constant (J = 15.5 Hz) displayed between H-4 and H-5. The C-8/C-9 double bond was assigned as *E* based on the typical upfield shift of the C-19 methyl group [3]. The sugar was assigned as an β-glucopyranoside based on the chemical shift of the anomeric proton (δ4.11), its large coupling constant

(J = 7.5 Hz).

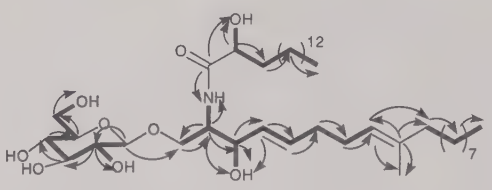

Fig. 2 Key HMBC (→) and COSY (——) correlations of compound A

Compound B analyzed for $C_{43}H_{79}NO_9$ by FABMS (m/z) 776 $[M + Na]^+$ and NMR data, a formula that indicated one more degree of unsaturation than Compound A. The ^1H and ^{13}C NMR spectra clearly indicated that there were one more double bond signals atδ_C129.0 [d, δ_H 5.58 (dddd, 15.5, 6.5, 5.5, 5.5)] and 123.4 [d,δ_H 5.67(dddd, 15.5, 7.5, 7.5, 1.5)]. Extensive analysis of the FABMS and NMR data for Compound B, and comparison with the data derived for compound A, led to the establishment of the structure of Compound B as Fig. 1 (B), and further confirmed by comparison with the NMR data derived for cerebroside C [6], which possessed the antifungal activity of aculeacin. In 1996, Keusgen et al. [7] also reported the isolation of this glycosphingolipid from the marine fungus *Microdphaerpsis olivaces*.

Compound C analyzed for $C_{34}H_{69}NO_3$ by FABMS (m/z) 540 $[M + H]^+$ and NMR data, a formula that indicated one degree of unsaturation. The ^1H and ^{13}C NMR spectra for Compound C displayed resonances typical of saturated dihydroxyceramide, such as signals of amide functionality atδ_C171.8(s) andδ_H7.40 (d, 9.0Hz, NH), and signals of long aliphatic chain atδ_C 13.5(q),δ_H 0.85(t, 7.0Hz, 6H). In the ^1H NMR spectra, the signals atδ_H 2.04 (m, 2H) indicated that the C-2' in the fatty acid acyl chain was not linked to hydroxy. Finally, the structure of Compound C was established as Fig. 1 (C) through extensive analysis of FABMS and 2D NMR, and was in agreement with *N*-palmitoyldihydrosphingosine [8]. Different from compounds A and B, Compound C is a ceramide.

Sphingolipids are the major lipid components of biological membranes. They serve as structural support and shape determinants of the cell membrane and, via protein binding, act as mediators of biological events such as activation, cell agglutination, intracellular communication, cell death, and cell growth [9]. Such cellular recognition events are common to cancer, allergy, viral infection, inflammation, and autoimmune disease [9]. Each of these events is executed by a specific sphingolipid such as ganglioside, tumor antigen, or viral receptor [9]. This exquisite degree of specificity suggests that sphingolipids could be suitable candidates for new drugs. Thus, It is of momentous significance to find that marine fungal strains No.1924 and 3893 could produce abundant sphingolipids [10].

Acknowledgements

Authors would like to give thanks to Professor L L P Vrijmoed and Professor E B G Jones in the City University of Hong Kong for providing marine fungal strains. The project was supported by the National

"863" Program of China (No. 2001AA624010), the Guangdong Provincial Natural Science Foundation of China (No. 04300674), the Guangdong Provincial Science and Technology Program Foundation of China (No.2004B30101017) and the Foshan City Foundation for the Development of Science and Technology (No. 2005081871).

References

[1] Pietra F. Secondary metabolites from marine microorganism: bacteria, protozoa, algae and fungi. Achievments and prospects [J]. Nat. Prod. Rep., 1997, 14(5): 453-464.

[2] Zhu F, Lin Y C. Marinemide, a novel alkaloid and its methyl ester produced by the application of mixed fermentation technique to two mangrove endophytic fungi from the South China Sea [J]. Chin. Sci. Bull., 2006, 51(12): 1 426-1 430.

[3] Zhu F, Lin Y C, Wang J, et al. Metabolites of mangrove endophytic fungus #2492 from the South China Sea [J]. Mar. Sci. Bull., 2006, 25(3): 34-37

[4] Blunt J W, Copp B R, Munro M H G, et al. Marine natural products [J]. Nat. Prod. Rep., 2006, 23(1): 26-78.

[5] Sitrin R D, Chan G, Dingerdissen J, et al. Isolation and structure determination of *Pachybasium* cerebrosides which potentiate the antifungal activity of aculeacin [J]. J. Antibiot., 1988, 41(4): 469-480.

[6] Jenkins K M, Jensen P R, Fenical W. Thraustochytrosides A-C: new glycosphingolipids from a unique marine protist, *Thraustochytium globosum*[J]. Tetrahedron, 1999, 40(43): 7 637-7 640.

[7] Keusgen M, Yu C M, Curtis J M, et al. A cerebroside from the marine fungus *Microsphaerpsis olivacea* (Bonord) Höhn [J]. Biochem. System. Ecolog., 1996, 24(5): 465-468.

[8] Bertello L E, Andrews N W, de Lederkrews R M. Developmentally regulated expression of ceramide in *Trypanosoma cruzi* [J]. Mol. Biochem. Parasitol., 1996, *79*(2): 143-151.

[9] Barrett A G M, Beall G C, Braddock D C, et al. Asymmetric allylboration and ring closing alkene metathesis: A novel strategy for the synthesis og glycosphingolipids [J]. J. Org. Chem., 2000, *65*: 6 508-6 514.

[10] Zhu F, Wu X Y, Lin Y C. Advances in the synthesis of glycosphingolipids [J]. Chin. J. Org. Chem., 2002, *22*(11): 807-816.

产自两株海洋真菌的三种鞘脂类的结构测定

朱峰[1]，陈光英[2]，林永成[3]

(1. 佛山科学技术学院化学与化工系，广东 佛山 528000；2. 海南师范大学化学系，海南 海口 571158；
3. 中山大学化学科学与工程学院，广东 广州 510275)

摘 要：3 种鞘脂类代谢产物 *N*-2'-羟基十六碳酰基-1-*O*-β-D-吡喃葡萄糖基-9-甲基-4*E*,8*E*-十八碳二烯-1-醇（**A**）、*N*-2'-羟基-3'*E*-十八碳烯酰基-1-*O*-β-D-吡喃葡萄糖基-9-甲基-4*E*, 8*E*-十八碳二烯-1-醇（**B**）和 *N*-十六碳酰基二氢鞘氨醇（**C**）分别产生于来源于中国南海的 2 株海洋真菌（菌株编号为 1924 和 3893），通过 2D NMR、MS 等方法测定了它们的结构。这是首次从南海红树内生真菌分离得到的 3 种鞘脂类代谢产物。

关键词：海洋真菌；代谢产物；鞘脂类化合物

Study on Remote Sensing of Water Depths Based on BP Artificial Neural Network

WANG Yanjiao [1,2], ZHANG Peiqun [1], DONG Wenjie [1,2], ZHANG Ying [3]

1. *Laboratory for Climate Studies of China Meteorological Administration, National Climate Center, Beijing* 100081, *China;*

2. *Institute of Atmospheric Physics, Chinese Academy of Sciences, Beijing* 100029, *China;*

3. *College of Geographical Science of Nanjing Normal University, Nanjing* 210097, *Jiangsu, China*

Abstract: A momentum BP neural network model (MBPNNM) was constructed to retrieve the water depth information for the South Channel of the Yangtze River Estuary using the relationship between the reflectance derived from Landsat 7 satellite data and the water depth information. Results showed that MBPNNM, which exhibited a strong capability of nonlinear mapping, allowed the water depth information in the study area to be retrieved at a relatively high level of accuracy. Affected by the sediment concentration of water in the estuary, MBPNNM enabled the retrieval of water depth of less than 5 meters accurately. However, the accuracy was not ideal for the water depths of more than 10 meters.

Keywords: Yangtze River Estuary; BP neural network; water-depth remote sensing; retrieval model

Introduction

Quantification of water-depth remote sensing is a very important period in the water-depth detecting by the remote sensing technology. Optical remote sensing techniques can extract large area and new shallow water depth information in a short time, because colour satellite imagery provides complete maps of areas and dynamic detecting. Many works have been studying the bathymetric maps by optical remote sensing techniques with excellent results from the seventies of the 20th century since the 1920s. V Mgenge [1] applied multi-temporal TM remote sensing imageries to map the shallow water depths nearby Netherlands and achieved better results. Bierwirth et al. [2] constructed a multi-band model to extract the water depths and bottom reflectance information from the Landsat TM imagery, which assumed that water properties were homogeneous and some area in the scene where depth varied over a uniform bottom, the model was applied to the Shark Bay in Western Australia and resulted in a bias of several meters with the Landsat retrieval being too deep. Janita and Ronald [3] established the empirical relationships between the depth and remote-sensed spectral radiance and constructed the back propagation-artificial neural network (BP-ANN) water depth retrieval model. Results showed that the neural network approach operated on a higher level than some traditional statistical methods for retrieval of remote sensed information. Dang Fuxing et al. [4] built the water-depth retrieval model of the Yongshu Reef in the South China Sea using the Landsat TM remote sensing imagery, based on the bottom type identification. They found that the bottom

Received on September 13, 2006

type identification could improve the model accuracy. Based on the analysis of the mechanism of remote sensing, Huang Jiazhu et al. [5] constructed a water-depth retrieval model for the Nantong section of Yangze River using quasi-synchronous landsat TM data and channel sounding data, indicating that the landsat TM data have some efficiencies in measuring shallow water depths in the high sediment discharge riverbed. Chen Ming et al. [6] established a subdivision model for remote sensing of water depths in the Yangtze River estuary considering the characteristics of water and sediment, and the remote sensing bathymetric chart acquired by the subdivision model agreed well with the measured one.

1 The study area and data used

1.1 The study area

The study site is located in the South Channel of Yangtze River Estuary and lies between latitudes 31°7′58″ and 31°21′47″N and between longitudes 121°40′40″ and 121°59′21″E. It was assumed that the water properties were homogeneous and the bottom was uniform in the study area. The maximal water depth is 16.6m; the average water depth is 5.48m. In this paper it is defined that the value below the theoretical datum plane is positive (Fig.1).

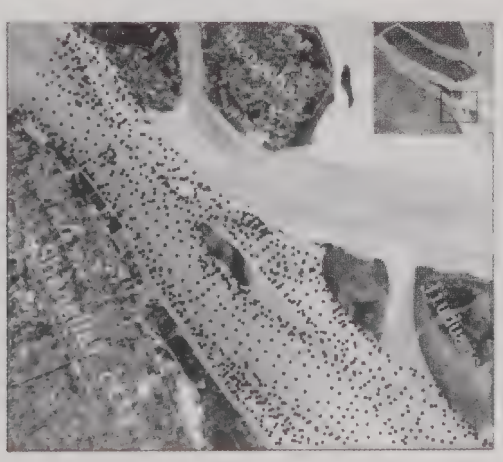

Fig. 1 Sketch of the study area

1.2 Data sets

Remote sensing imagery data used in this study were collected from the Yangtze River Estuary of China on November 7, 2002. Water depth data in the study area were measured from July to November in 2003 with a plotting scale of 1:60000. Because there were no deluges and other abnormal weather during the period, it was considered that the underwater topography had changed indistinctly and the bathymetry mapping and the remote sensing imaging are quasi-synchronous.

2 Data processing and analysis

2.1 Remote sensing image processing

2.1.1 Atmospheric correction

The atmospheric absorption and scattering can weaken the solar radiation energy during the satellite imaging, which greatly influences the information extraction from the remote sensing imagery and parameter retrieval, so the remote sensing imagery must be atmospherically corrected. In this paper, the improved Dark Object Subtraction (DOS) algorithm was used (Mausel, 2002)[7], and it assumed that the ground surface was Lambert's plane reflection and the sky irradiance was isotropy and there were absolute dark objects such as clear water and shadow etc. in the images. In addition the algorithm not only considered the atmospheric scattering and absorption effects in the process of radiation transmission, but also corrected the effects caused by aerosol. The model is expressed as:

$$\rho_{bandN} = \frac{\pi((L_{bandN}Gain_{bandN} + Bias_{bandN}) - (H_{bandN}Gain_{bandN} + Bias_{bandN}))D^2}{E_{bandN}\cos\theta TAU_v TAU_z}$$

Where N is the serial number of band, ρ_{bandN} is the surface reflectance, L_{bandN} is the digital numbers (DN), H_{bandN} was the dark objects in the band N, L_{bandN} and H_{bandN} can be got from remote sensing images. D is the standardized solar-terrestrial distance, E_{bandN} is the exo-atmospheric solar irradiance, D and E_{bandN} can be gained from the references [8, 9]. $Gain_{bandN}$ and $Bias_{bandN}$ are the slope and intercept of response function respective, θ is the solar zenith angle in degrees. TAU_v is the atmospheric transmittance along the path from the ground surface to the sensor, which is usually equal to 1, because the view angle is 0 in the landsat sensor imaging process. TAU_z is the atmospheric transmittance along the path from the sun to the ground surface, Chavez [10] presented an algorithm to calculate the TAU_z approximatively, i.e., TAU_z could be substituted by the cosine value of Zenith angle. Finally the remotely sensed digital numbers (DN) of six bands are converted to the ground surface reflectance respectively using the above atmospheric correction algorithm.

2.1.2 Geometric correction

The remote sensing imagery was geometrically corrected using ground control points collected from field measurement topographic maps of Yangtze River Estuary with a plotting scale of 1 : 10 000 and the Xian 80 coordinate system. Thirty ground control points such as lock entrances and bridges etc. were selected from the topographic maps and the geometric errors were in 0.5 pixel. Finally the image system was transformed to the map system using a linear algebraic formula using the ENVI software.

2.1.3 Land and water separation

The water and land in the image were separated in order to study the water better. Because the near infrared bands are intensively absorbed by water and the pixels with the TM5 reflectance higher than 6% represent emerged land (Fig.2), the masked image was built using Landsat TM5 (Fig.3) and was

superimposed on the Landsat TM1 to TM4 to mask the land information.

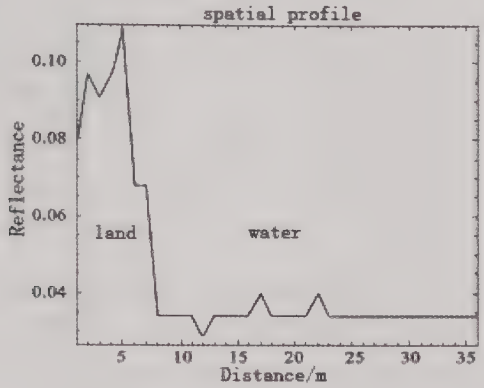

Fig. 2 Reflectance variation of TM5 from land to water

Fig. 3 The mask figure built by TM5

2.2 Water depth data processing

The underwater topographic map was field measured in 2003 with the plotting scale of 1:60,000 and the Beijing 54 coordinate system. First, the topographic map was geometrically corrected using the projection and the latitudes and longitudes labeled in the map, and then the water depths in the map were digitized. Because the coordinate system of topographic map was Beijing 54 and that of the geometrically corrected remote sensing image was Xian 80, we must transform them into the same coordinate system in order to make the water depths and the pixel reflectance matched. By selecting seven control points that had the latitudes and longitudes of Xian 80 coordinate in the underwater topographic map, using the seven parameter method the map system was transformed into the image system, so the water depths in the map and the pixel reflectance in the image were one-to-one correspondence (Fig.1).

2.3 The water depth and remote sensing data extraction and analysis

First, 987 water depth measurements with latitudes and longitudes in the South Channel of Yangtze River Estuary were extracted from the underwater topographic map, and second, pixel reflectances of all bands with latitudes and longitudes were gained by outputting the file format as .xyz using the ENVI software. The pixel reflectances that had the same latitudes and longitudes as the bathymetry measurements were selected by the program. Owing to the changes of the coast, the bathymetry measurements corresponding to the zero pixel reflectance were eliminated. Finally 972 bathymetry measurements and pixel reflectance with the same latitude and longitude were used.

Correlations between pixel reflectance of all bands and water depths were analyzed in order to select the better water depth retrieval factors. Because band ratios can eliminate the influence of environmental factors and improve the correlations between spectral reflectance and water depth information (Zhang Ying et al., 2000) [11], band ratios were calculated and correlations between each band ratio and water depths were analyzed. Results showed that the correlations between the TM4/TM2, TM4/TM3, TM4/TM1, TM3/TM2 and the water depths were better than those of other bands and band ratios (Tab.1). Finally, TM1, TM2, TM3, TM4, TM4/TM1, TM4/TM2, TM4/TM3, TM3/TM2 were selected to retrieve water depths and adopted for further modeling.

Tab. 1 The correlation between reflectance of bands and band combination and water depths

Factors	TM1	TM2	TM3	TM4	TM4/TM1	TM4/TM2	TM4/TM3	TM2/TM3
Corrlation	0.269	0.219	0.351	0.555	0.467	0.554	0.544	0.415

3 MBPANN water depth retrieval model established

Artificial neural networks (ANNs), based on the biological neural networks, are information processing methods of simulating behaviors of man brain. Owing to the strong abilities of self-learning, self- organizing, self-adaptability and nonlinear mapping, the ANNs exhibit stronger capabilities of simulating the nonlinear systems than the traditional statistical methods [12]. In this paper a back-propagation artificial neural network (BP-ANN) was applied, BP-ANN has a solid theoretical basis and it is widely used in various fields. Because the BP-ANN method has the defects of slow convergence velocity and easily running into local minimum and over fitting, the BP-ANN method was improved by introducing the momentum factor and the weight control algorithm [13-16].

3.1 Model building

In this paper, a typical three-layered MBP-ANN model was established including an input layer, a hidden layer and an output layer. A tangent sigmoid transfer function was used for the hidden layer and the linear transfer function was used for the output layer. The single band and band ratios selected above used as predictors and the corresponding water depth measurements were predictands. Six hundred pixel reflectance and water depth measurements were random selected as the training samples and 372 pixel

reflectance left as test samples. The number of hidden layer neurons and other parameters in the MBPANN model were determined by continuously leaning and training between the predictors and predictands, and the relationship between the spectral reflectance and the water depths was established by selecting the optimal weights and biases. Finally the structure of MBPANN model was as follows: the number of input, hidden and output layer neurons was 8, 18 and 1 respective; the leaning rate was 0.05, the increasing and decreasing ratio was 1.2, the momentum parameter was 0.9, the training precision was 0.5 and the error radio was 0.4.

3.2 Model testing

The performance of the MBPANN was evaluated as follows: first, the 327 samples which never joined the training of MBPANN model and were looked as the independent test samples, were inputted to the model to calculate the water depths. The retrieval water depths compared with the field water depth measurements were shown in Fig. 4, and the mean absolute errors between them were 0.9 m。

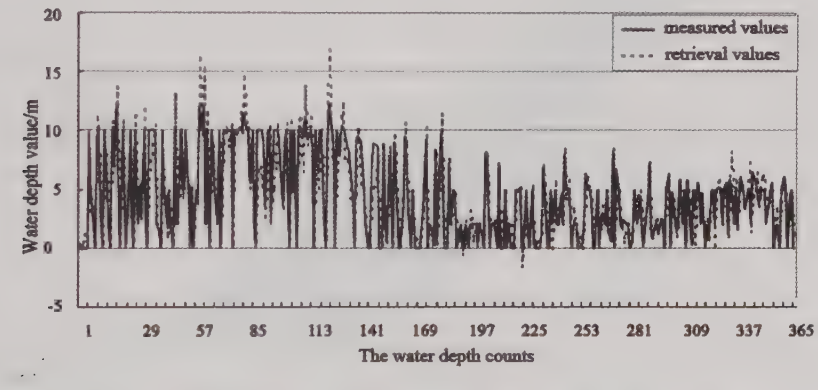

Fig. 4 Comparison of retrieval and field measured water depths

Second, the field measured water depths were compared with the model retrievals by dividing three ranges (Tab. 2) in order to evaluate the performance of MBPANN model further. Results showed that the MBPANN model enabled the water depth retrievals of less than 5 meters to be made accurately, the mean absolute errors were 0.6 meters, however the accuracy was not ideal for the depth of more than 10 meters, the mean absolute errors were 1.7 meters. The relatively great errors for the depth of more than 10 meters could be attributed to the high suspended sediment concentration in the Yangtze River Estuary which made the light radiation hardly accessible to the deeper water. Finally, the MBPANN model was applied to each pixel in the study area scene and the depth image was produced (Fig. 6), and then the depth error image for the study area was got by subtracting the model retrievals from the field measured water depths (Fig. 7).

Fig. 5 was the truth water depth image produced by resampling field measured data, Fig. 6 was the MBPANN model depth image, and Figure 7 was the depth error image for the study area. Comparing Fig. 5 with Fig. 6 it could be seen that: the MBPANN model could retrieve the water depths of less than 10

meters accurately, especially for the water depths of less than 5 meters, the model exhibited the best performance, the distribution of less than 5 meter water depths could be seen clearly in the study area (Fig.6), however the accuracy was not ideal for the depth of more than 10 meters, we only got the general distributions of more than 10 meter water depths. In addition, the same results could be seen in Fig. 7.

Tab. 2 Comparison of retrieval and measured water depths of different ranges

Water depth ranges /m	Water depth counts	Mean absolute errors /m
10-17	61	1.7
5-10	61	1.1
0-5	250	0.6

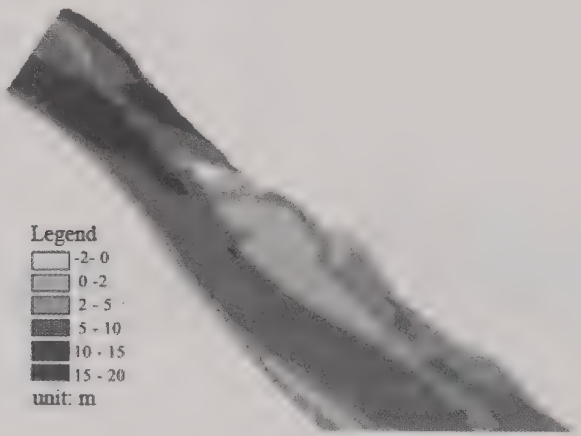

Fig. 5 The fathom map interpolated by measured water depths

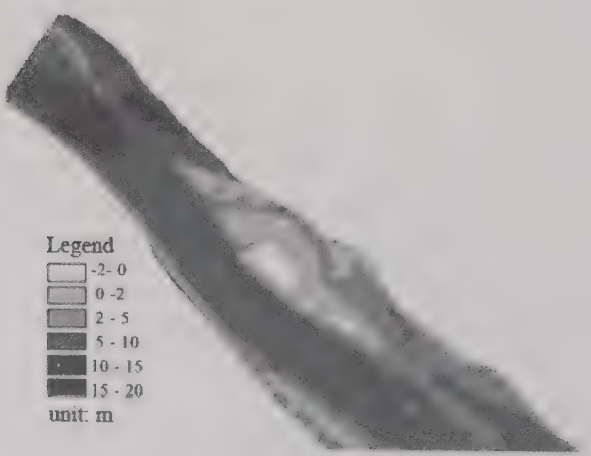

Fig. 6 The water depth retrieved by BP network model

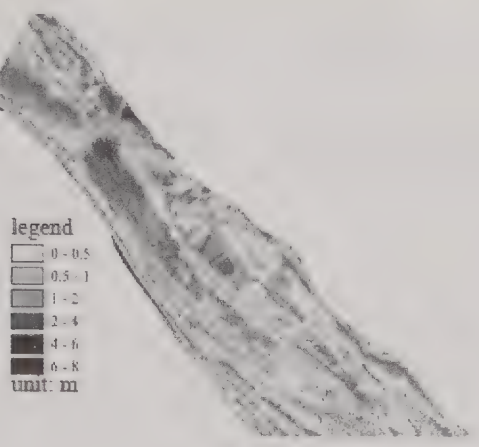

Fig. 7 The absolute error between the retrieval and situ measured water depths

4 Conclusions

At present, water depth retrievals by multispectral remote sensing always use the traditional statistical models. In this paper, the MBPANN model was constructed to retrieve the water depth information for the South Channel of the Yangtze River Estuary combined with the RS and GIS technology. Results showed :

a) The water depths detecting by the remote sensing technology is a non-linear process affected by many factors, and the BPANN is a massively parallel non-linear dynamic system with strong capabilities of self-adapted learning and non-linear mapping, so it exhibits a better performance than the traditional statistical methods in bathymetry mapping by the remote sensing technology.

b) A momentum BPANN model established using the relationship between reflectance derived from satellite data and actual water depths allowed the water depth information in the South Channel section of Yangtze River Estuary to be retrieved at a relatively high level of accuracy, the mean absolute errors between the measured water depths and the model retrievals were 0.9 meters.

c) The field measured water depths and the model retrievals were compared by dividing three ranges. Results showed that the MBPANNS model enabled the retrievals of water depth of less than 5 meters to be made accurately, the mean absolute errors was 0.6 meters , however the accuracy was not ideal for the depth of more than 10 meters, the mean absolute error were 1.7 meters. The relatively great errors for the depth of more than 10 meters could be attributed to the high suspended sediment concentration in the Yangtze River Estuary which made the light radiation hardly accessible to the deeper water. The conclusions indicated that the water depth inversion model established using the momentum BPANN method has a practical application value.

Acknowledgements

The project was supported by the Key Program of National Natural Science Foundation (Project No.50339010) and the Huaihe Valley Open Fund Project (No.Hx2007).

References

[1] Mgengel V, Spitzer R J. Application of remote sensing data to mapping of shallow sea-floor near by Netherlands [J]. International Journal of Remote Sensing, 1991, 57(5):473 - 479.

[2] Bierwirth P N, Lee T J, and Burne R V. Shallow sea-floor reflectance and water depth derived by unmixing multispectral imagery [J]. Photogramm. Eng. Remote Sens., 1993, 59:331-338.

[3] Juanita C. S., Ronald J. H. Coastal bathymetry from hyperspectral observations of water radiance [J]. Remote Sensing of Environment, 1998, 65:341- 352.

[4] Dang Fuxing, Ding Qian. A technique for Extracting water depth information from multispectral scanner data in the South China Sea [J]. Marine science bulleting, 2003, 22(3):55-60.

[5] Huang Jiazhu, You Yuming. Experiment of water depth surveying in the Nantong section of the Yangtze River [J]. Adnances in water science, 2002, 13(2): 235-238.

[6] Chen Ming, Li Shihong and Kong Qingfen. Fathoming method by satellite remote sensing for the Yangze River estuary water body [J]. Hydro-science and engineering, 2003, 2:61-64

[7] Mausel P D, Brondizio E, Moran E. Assessment of atmospheric correction methods for Landsat TM data applicable to amazon basin LBA research [J]. International Journal of Remote Sensing, 2002, 23(13):2651 - 2671.

[8] Gyanesh C, Brian M. Revised Landsat-5 TM radiometric calibration procedures and postcalibration dynamic ranges[J] . Transactions on Geoscience and Remote Sensing, 2003, 41(11):2647 - 2677.

[9] NASA Landsat 7 Science Data Users Handbook [OB/OL]. Http: / / ltpwww. gsfc. nasa. gov/ IAS/ handbook/ handbook-toc. html.

[10] Chavez PS Jr and DK MacKinnon. Image－based atmospheric corrections－revisited and improved[J] . Photogrammetric Engineering and Remote Sensing, 1996, 62(9):1025 - 1036.

[11] Zhang Ying, Wang Yigang. Remote sensing technology of subwater topography [J].Ocean engneering, 2000, 18(3):88-91

[12] Jin Long, Chen Ning, Lin Zhenshan. Study and comparison of ensemble forecasting based on artificial neural network [J]. Acta meteorological sinica, 1999, 57(2):198-207

[13] Yuan zengren. Artificial neural network and application (M). 2000, Beijing: Tsinghua university publication

[14] Zhang Xiang, Ding Jing. Controlled-weight method for improving the generalization ability of layered forward neural networks [J]. Advances in water science, 1998, 9(4):373-377

[15] Wen xin, Zhou Lu, Wang Danli. Neural networks application and design [M]. 2000, Beijing: science publication

[16] Lou Shuntian，Shi Yang. Neural networks－based on the MATLAB analysis and design [M]. 2000, Xian: Xian electron scientific and technical university publication.

基于 BP 人工神经网络的水体遥感测深方法研究

王艳姣[1,2]，张培群[1]，董文杰[1]，张鹰[3]

（1. 国家气候中心，北京 100081；2. 中科院大气物理研究所，北京 100029；
3. 南京师范大学地理科学学院，江苏 南京 210097）

摘　要：利用 Landsat7 ETM+ 遥感图像反射率和实测水深值之间的相关性，建立了动量 BP 人工神经网络水深反演模型，并对长江口南港河段水深进行了反演。结果表明：具有较强非线性映射能力的动量 BP 神经网络模型能较好地反演出长江口南港河段的水深分布情况；由于受长江口水体高含沙量的影响，模型对小于 5 m 的水深值反演精度较高，而对大于 10 m 的水深值反演精度较低。

关键词：长江口；BP 神经网络；水深遥感；反演模型

Dinoflagellate Cysts Records from Core Samples of Modern Marine Sediment at the Luoyuan Bay Mouth

SUN Aimei [1], LI Chao [1], LAN Dongzhao [2], ZHU Yue [1]

1. *Department of Oceanography/Institute of Subtropical Oceanography, Xiamen Univ., Xiamen* 361005, *Fujian, China*

2. *Third Institute of Oceanography, SOA, Xiamen* 361005, *Fujian, China*

Abstract: Thirty species of dinoflagellate cysts in 15 genus are identified from KMZK5 Core samples of recent marine sediment at the Luoyuan Bay mouth, Fujian. All of these dinoflagellate cysts are first recorded in the Luyuan Bay, 12 species of them are not distributing in the near sea area such as Sansha Bay and Minjiang estuary, including 6 kinds of toxic species, such as *Alexandrium affine*、*A. minutum*, *A. tamarense*, *Gonyaulax spinifera*, *Gymnodinium catenatum* and *Scrippsiella trochoidea*. The abundance and vertical distribution characterestics of the main and the toxic dinoflgellate cysts are also studied in the paper.

Keywords: dinoflagellate cysts; vertical distribution; toxic dinoflagellate species

Introduction

The dinoflagellate resting cysts are the non-motion zygotes formed by vegetation cells sexual reproduction. They may float in waters and eventually sink on the sea floor to resist the unfavorable environmental condition for plankton cells, after recovery of the environmental condition they can germinate and re-establish motile population in the sea waters and reproduce in an agamogenesis way, so the dinoflagellate cysts may be treated as one seed source of red tide [1, 2].

Two different phragma, organic sporo-pollenin or calcareous material build up the wall of modern dinoflagellate cysts, and the organic sporo-pollenin wall is highly resistant to the chemically and biologically adverse ambient condition, which provides specific resistant features of the resting cysts and gives them a chance to be preserved perennially in marine sediments. The dinoflagellate cysts in marine sediment can reflect the taxa of vegetation cells in waters so that the dinoflagellate communities and the marine environmental changes can be reconstructed on the basis of the cyst assemblages [3].

The Luoyuan bay locates in the intersection of Luoyuan County and Lianjiang County, Fujian Province, which is surrounded by hills with a large internal sea area and a narrow mouth. With the large-scale increasing of cage aquaculture and the decreasing of laminaria culture, the frequency and the duration of red tide occurrence increase distinctly in the Luoyuan bay [4]. Although the investigation on algae assemblages including dinoflagellate communities in the water column had been carried out before [5], researches on dinoflagellate cysts in sediment have not been done in the Luoyuan bay. The depth of core sediment samples reserving the dinoflagellate cysts mainly limits to the surface of 0-20 cm,

Received on May 8, 2006

there is lack of the corresponding research on dinoflagellate cysts in the core sediment exceeding 20cm in depth [2, 5]. The component and the abundance of dinoflagellate cysts in the KMZK5 core, which locates in the Luoyuan bay entrance sea area, is about 100 cm-long, are studied in this paper. The results can not only provide reference for studying the change of dinoflagellate communities in waters, but also reconstruct the process of eutrophication in the Luoyuan bay.

1 Materials and methods

1.1 Sampling

The KMZK5 core sediment, which was collected in the Luoyuan Bay, 100 cm in length (26°26′51″N, 119°49′54″E; 17.3 m water depth; Fig. 1), was taken continuously every 4 cm, so a total of 25 samples were analysed.

The core sediments consist of clayish fine grain and shell fragments from 0 cm to 4 cm, gray clay from 4 cm to 100 cm. There is no evident bioturbation in the core section.

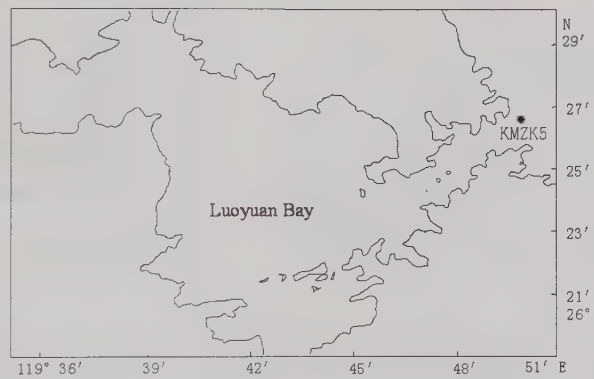

Fig.1 Location of the sampling core

1.2 Methods of analysis

The samples for analysis are placed into a drying oven under 70 ℃ for about 24 hours and weighed 5 gram in beaker. Add 20 mL distilled water and mix it with the sediment. Then disperse the samples by ultrasonic disintegrator at a frequency of 150 Hz for 2 min. Wash the dispersed samples with distilled water under a set of two sieves of mesh-size with 125 μm being the upper and 15 μm being the lower to remove the tiny particles of sediment. Put the residue in a 10 mL tube for centrifugation (approx. 4000 rpm, 2 min). Suck out the supernatant by a pipette till to 2 mL and shake it up, then add 1 mL solution of the tungstenic acid natrium (1.6 special gravity), suck out all of the upper layer samples carefully by a pipette and move them into a 5 mL tube to wash on the 15 μm sieves for two times, collect all residues on the 15 μm sieves into the 5 mL vial and make up the solution 2 mL with distilled water. This is the refined sample ready for the next study. The cysts identification was carried out under an bio-microscope Nikon E400 with a

photomicrographic system. The total number of identification cysts is counted until more than 100 grains.

2 Results and discussion

2.1 The components of dinoflagellate cyst species in Core KMZK5

More than 30 dinoflagellate cyst species belonging to 15 genera (Plate Ⅰ) were identified from the sediment of KMZK5 core on the basis of the criterion created by Kazumi and Yasuwo[6]. The species of dinoflagellate cyst are: *Alexandrium affine*, *A. minutum*, *A. tamarense**, *Cochlodinium polykrikoides*, *Diplopsalis lenticula*, *Gonyaulax scrippsea*, *G. spinifera**, *Gymnodinium catenatum**, *Gyrodinium impudicum*, *Lingulodinium polyedrum*, *Pheopolykrikos hartmannii*, *Polykrikos kofoiddii*, *Prorocerátium reticulatum*, *Protoperidinium americanum*, *P. avellana*, *P. claudicans*, *P. compressum*, *P. conicum*, *P. conicoides*, *P. denticulatum*, *P. latissimum*, *P. leonis*, *P. minutum*, *P. oblongum*, *P. pentagonum*, *P. subinerme*, *P. thorianum*, *Pyrophacus steinnii*, *Scrippsiella trochoidea**, *Zygabikodinium lenticulatum* (*means toxic species).

A total of 17 species belonging to 6 genera of dinoflagellate vegetation cells have been identified in the water column[5], they were *Ceratium furca*, *Cer. fusus*, *Cer. inflatum*, *Cer. deflexum*, *Cer. macroceros*, *Cer. massiliense*, *Cer. trichoceros*, *Cer. breve*, *Cer. gibberum*, *Cer. tripos*, *Cer. pulchellum*, *Dinophysis caudate*, *Noctiluca scintillans*, *Prorocentrum micans*, *Protoperidinium depressum*, *P. oceanicum*, *Pyrophacus* var. *horologium*. Among them only *Pyrophacus* var. *horologium* can form the resting cyst, but the cyst of this species was not found in the sediment. 29 species of dinoflagellate were recorded in the Xinghua Bay, Fuqing Bay, Sansha Bay and Shacheng Bay according to the literature [5], among which only *Protoperidinium conicum*, *P. pentagonum* and *Pyrophacus* var. *horologium* can form the resting cyst.

The dinoflagellate cysts found in the core sediments from the Luoyuan bay have the similar characteristics to that were found in surface sediments from the adjacent Mingjiang estuary and Sansha bay[7], for example, among the 20 species in 9 genera of dinoflagellate cysts recorded in the surface sediments from the Sansha bay, there are 12 species found in the Luoyuan bay: *Alexandrium affine*, *A. minutum*, *A. tamarense*, *Gonyaulax scrippsea*, *G. spinifera*, *Lingulodinium polyedrum*, *Polykrikos kofoiddii*, *Prorocerátium reticulatum*, *Protoperidinium americanum*, *P. conicum*, *P. minutum* and *Scrippsiella trochoidea*. Among the 17 species in 7 genera of dinoflagellate cyst recorded in the surface sediments from the Mingjiang estuary [1], there are more than 14 species found in the Luoyuan bay, such as *Alexandrium affine*, *A. tamarense*, *Gonyaulax scrippsea*, *G. spinifera*, *Polykrikos kofoiddii*, *Prorocerátium reticulatum*, *Protoperidinium avellana*, *P. conicum*, *P. conicoides*, *P. denticulatum*, *P. leonis*, *P. oblongum*, *P. pentagonum* and *Scrippsiella trochoidea*. But the other 12 species of dinoflagellate cysts recorded in the Luoyuan bay are not found in the Mingjiang estuary and Sansha bay, including *Cochlodinium polykrikoides*, *Diplopsalis lenticula*, *Gymnodinium catenatum*, *Gyrodinium impudicum*, *Pheopolykrikos hartmannii*, *Protoperidinium claudicans*, *P. compressum*, *P. latissimum*, *P. subinerme*, *P. thorianum*, *Pyrophacus steinnii*, *Zygabikodinium lenticulatum*, especially *Gymnodinium catenatum*, the toxic dinoflagellate cyst has never been recorded in the Luoyuan bay before.

The dinoflagellate cysts preserved in the sediments suggest that the same vegetation cells should

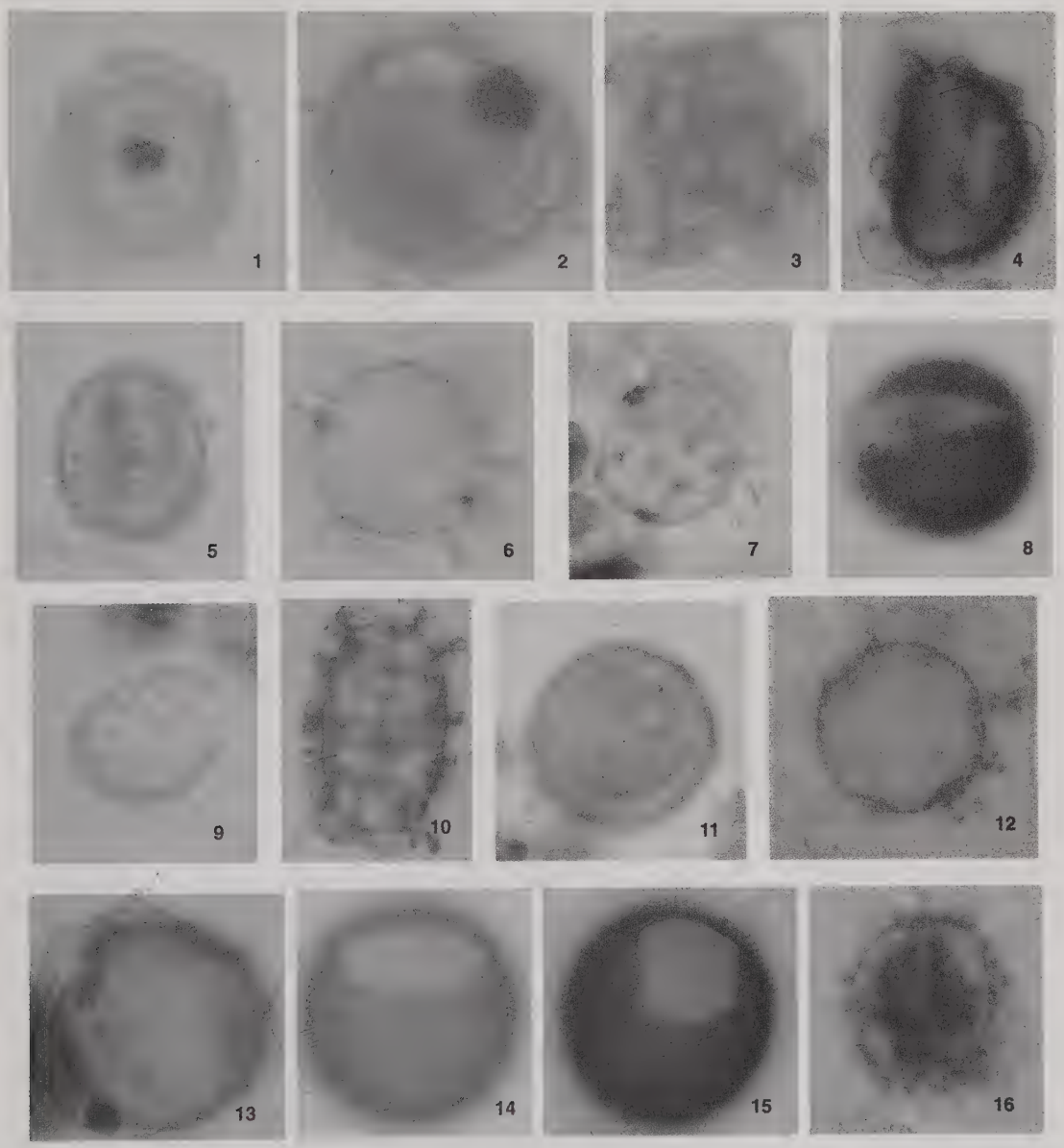

Plate Ⅰ Dinoflagellate cysts from core samples of submarine sediment at the Luoyuan Bay mouth

1. *Alexandrium affine* (×500), 2. *Alexandrium minutum* (×700), 3. *Alexandrium tamarense* (×400),
4.*Cochlodinium polykrikoides* (×600), 5.*Diplopsalis lenticula* (×600), 6.*Gonyaulax scrippsae* (×600),
7.*Gonyaulax spinifera* (×500), 8.*Gymnodinium catenatum* (×500), 9. *Lingulodinium polyedrum* (×500),
10.*Polykrikos kofoiddii* (×500), 11.*Pheopolykrikos hartmannii* (×550), 12. *Prorocentrum reticulatum* (×700),
13. *Protoperidinium americanum* (×800), 14, 15. *Protoperidinium avellana* (×650),
16.*Protoperidinium conicum* (×570),

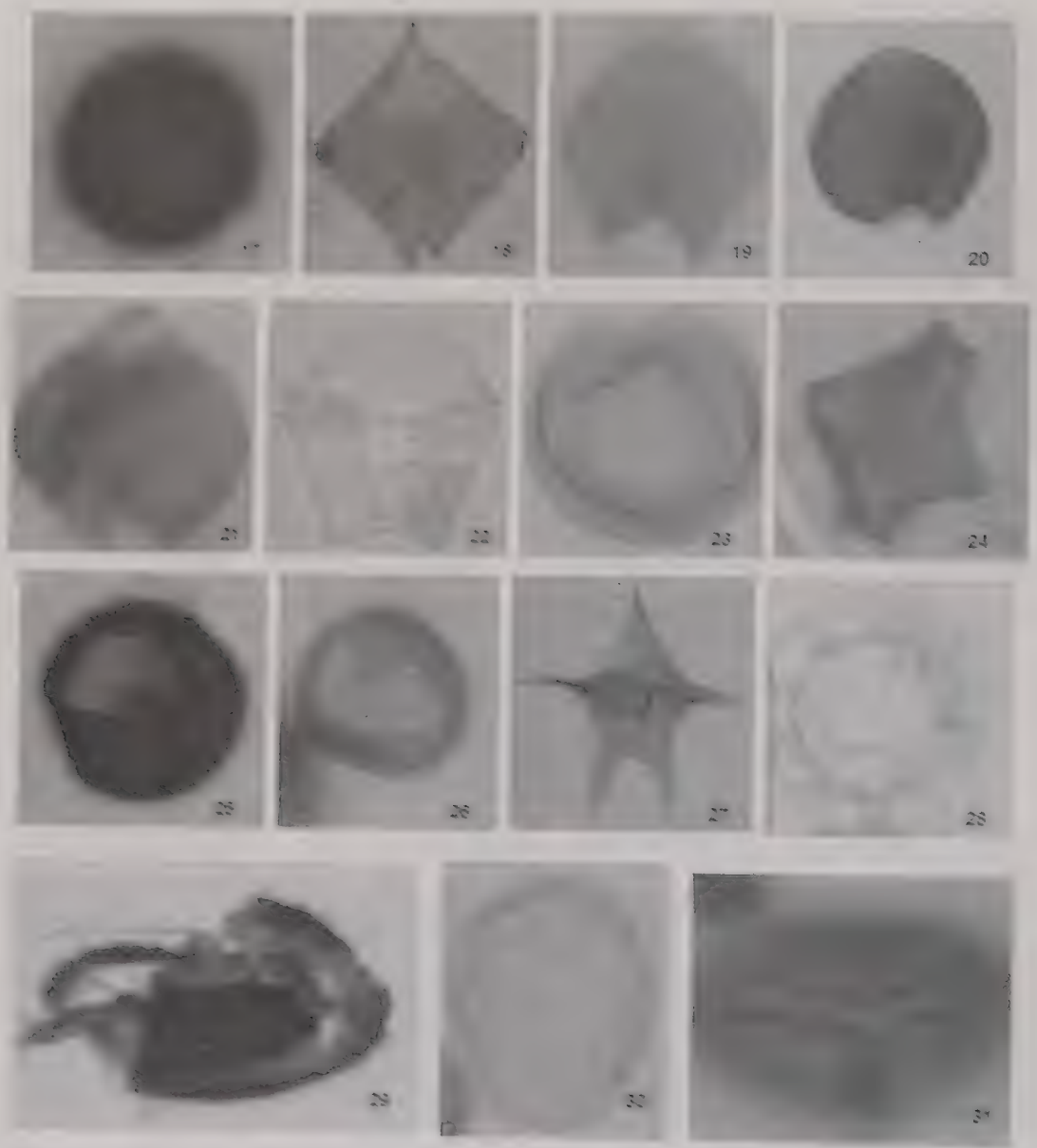

Plate 1 (continue) Dinoflagellate cysts from core samples of submarine sediment at the Laoyuan Bay mouth

17. Protoperidinium leonis (×1000). 18. Protoperidinium pentagonum (×350).
19. Protoperidinium leonis (×380). 20, 21. Protoperidinium oblongum (×450).
22. Protoperidinium pentagonum (×400). 23, 24. Protoperidinium subinerme (×600).
25. Protoperidinium thorianum (×600). 26. Protoperidinium denticulatum (×400).
27. Protoperidinium compressum (×500). 28. Pyrophacus steinii (×400).
29–31. Spiniferites mirabilis (×400). 32. Lingulodinium machaerophorum (×600).

exist in water. But there has obvious distinction between dinoflagellate cysts found in the sediment samples and the dinoflagellate vegetation reported by the literature [5], this fact also exists in the Minjiang estuary [1], Sansha bay [7] and Xiamen bay [8]. Besides the fact that most dinoflagellate cells recorded in the past investigation could not produce resting cysts, it may be caused by the reasons as follows. Firstly, the criterion mesh-size tow net is 77 μm according to the Ocean Investigation Criterion- Halobios Investigation (GB/T 12763. 6-1991), but the sizes of many kinds of dinoflagellate cells range from 40 μm to 60 μm, those cells with sizes smaller than 77μm can leak from the standard mesh-size tow net. Secondly, some dinoflagellates can decompose at once as dying, it is very difficult to be preserved by fixed liquor, such as *Polykrikos kofoiddii* can be observed alive in the spot test of sea water, but it can never be observed in the fixed samples. Thirdly, some newly discovered dinoflagellates species, which can produce resting cysts, may probably be introduced into the study sea area by some approaches, such as by ballast water discharging, by introduction of new species for aquatic-breeding. A detailed study need be carried out to solve this problem.

All the identified dinoflagellate cysts are preserved in the core sediment, some kinds of dinoflagellate cysts may be alive according to the fresh protoplasm in surface sediments, the other dinoflagellate cysts in core sediments cannot reproduce or have just reproduced to leave empty cysts. More precise dinoflagellate cysts identification by cyst breeding can be carried out after collecting modern surface sediment samples in the Luoyuan bay in the future.

2.2 Vertical distribution of dinoflagellate cysts

The vertical distribution of important dinoflagellate cyst species and their abundance, the total cysts abundance is plotted in Fig.2. *Gonyaulax scrippsea*, *Lingulodinium polyedrum*, *Polykrikos kofoiddii*, *Prorocentrum reticulatum*, *Protoperidinium leonis* and *P. oblongum* have relatively high abundance, with the values about 20 cysts•g^{-1} (dry weight), but the other dinoflagellate cysts abundances are less than 10 cysts•g^{-1} and distributing discontinuously in the whole core section.

As shown in Fig.2, *Gonyaulax scrippsea*, *Lingulodinium polyedrum*, *Protoperidinium leonis* and *P. oblongum* generally have maximum abundance values in the upper part of the core and increase evidently at 4 - 6 cm, *L. polyedrum* and *P. leonis* reaches the maximum value of about 15 cysts•g^{-1} at 5 cm, whose relatively abundance reaches 14 % of the total cysts. *Lingulodinium polyedrum* is a typical coastal species, and its high abundance (5 % - 40 % of the total cysts) is an index of eutrophic waters [9], so a eutrophication process can be deduced on the basis of the cyst abundance of *Lingulodinium polyedrum* at 5cm. High abundance of dinoflagellate cysts in surface sediments is likely to associate with the red tide occurring in the Luoyuan bay in the past two years [4]. Main kinds of dinoflagellate cysts' abundances are no more than 10 cysts•g^{-1}, such as *Lingulodinium polyedrum* is less than 5 cysts•g^{-1}. *Gonyaulax scrippsea*, *Polykrikos kofoiddii* and *P. oblongum* can not be found in some layers of the core between 20cm and 55cm. In the lower part of core (under 55cm), main dinoflagellate cysts present continuously. *Gonyaulax scrippsea* has a high abundance of 9 - 15 cysts•g^{-1} and reaches the maximum value of 15 cysts•g^{-1} at 90cm. *P. leonis* has two high value points (up to 13 cysts•g^{-1} and 14 cysts•g^{-1}) at 56cm and 86cm respectively. The cyst abundance of *Prorocentrum reticulatum* limits to 10 cysts•g^{-1}, and has an increasing trend with depth

under the section of 50 cm in the core.

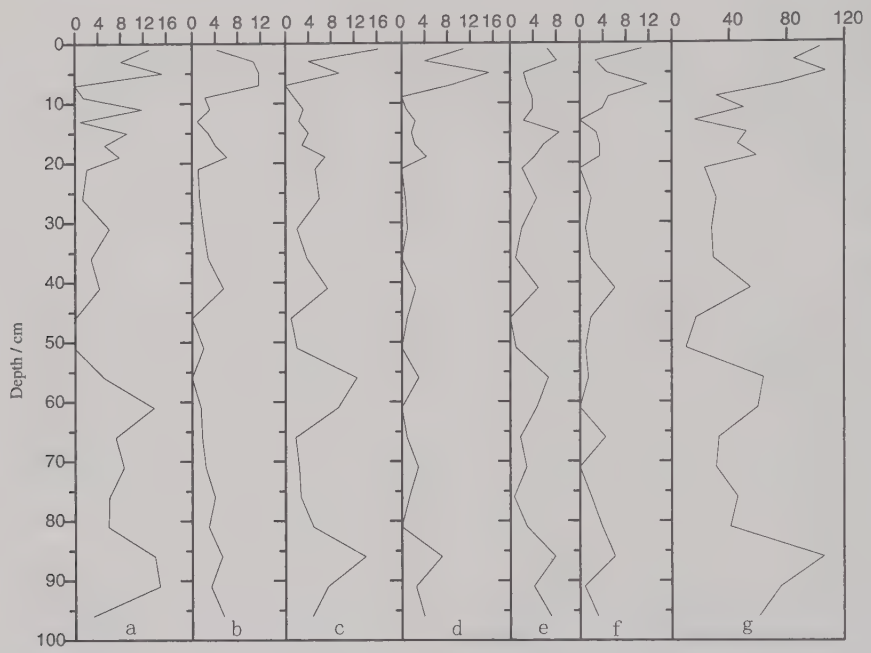

Fig. 2 Vertical distribution of main dinoflagellate and total cysts concentration

a. *Gonyaulax scrippsea*, b. *Lingulodinium polyedrum*, c. *Polykrikos kofoiddii*, d. *Prorocerátium reticulatum*, e. *Protoperidinium leonis* f. *P. oblongum*, g. total abundance of all dinofalgellate cysts.

The total dinoflagellate cysts abundance is from 10 cysts•g^{-1} to 107 cysts•g^{-1}, in the upper part of the core (0 - 30 cm), the total cysts abundance shows an increasing trend toward the top of the core and shows relatively high values at 5 cm, the total cysts abundance has 3 peak values (56 cysts•g^{-1} at 41 cm, 64 cysts•g^{-1} at 56 cm, 106 cysts•g^{-1} at 86 cm) between 30 cm and 100 cm, there are lower values of cysts abundance between the peak values, and the minimum value of cysts decreases to 10 cysts•g^{-1} at 86 cm.

The depositional behavior of dinoflagellate cysts is like that of clay, and their abundance increases along with the percentage of clay increasing in sediments (Dale 1983) [10]. Anderson suggests that dinoflagellate cysts mainly deposit in the low sea floor in the process of clay grain accumulation [11]. The core (0 - 4 cm) consists of clayish fine sand at the top sample (0 - 4 cm) and clay in the part of 4 - 100 cm, which may explain for the maximum dinoflagellate cysts abundance at 4 - 6 cm. Besides, the core is located at the mouth of Luoyuan bay, the high abundance of the dinoflagallete distributing in the inner bay can be transported to the outside of the bay by ebb-tide, and deposit along with the hydrodynamic condition decreasing in the process of transportation. Recently, the rapid development of aquiculture at the Luoyuan bay has led to eutrophication in the sea waters, red tides in the southwest and east of the bay happen almost every year, moreover the frequency of the red tide shows an increasing trend [4]. Thus, the

high abundance of dinoflagellate cysts in the surface sediment from the Luoyuan bay mouth is likely to indicate the red tide events occurring in the bay; high abundances of dinoflagellate cysts in the different lower sections of the core may also indicate the red tide events occurring inside of the bay in the past years. For lacking surface and core sediment samples from the inner part of the bay, the red tide records and the data of the core sediment age-dating, the reason for the high abundance of dinoflagellate cysts in the lower part of the core awaits further analysis in the future.

2.3 Distribution of toxic dinoflagellate cysts

Six toxic species have been identified from the core sediment samples shown in Fig. 3, they are *Alexandrium affine*, *A. minutum*, *A. tamarense*, *G. spinifera*, *Gymnodinium catenatum* and *Scrippsiella trochoidea*. Among them, *Alexandrium affine* only distributes in the top of core with an abundance of 1 cysts•g^{-1} and the other toxic dinoflagellate cysts distribute discontinuously. The characteristics of *A. minutum* and *A. tamarense* distribution are obviously discontinuous in the whole core section, their abundances have the similar trends at 50 - 100 cm, no more than 10 cysts•g^{-1}. *G. spinifera* distributes throughout the whole core with a maximum abundance of about 9 cysts•g^{-1} at the top of core and different peak values of abundance at 6 cm, 40 cm, 60 cm, 86 cm and the bottom of the core. *Gymnodinium catenatum* only distributes in the top of samples or in the lower part of the core (74 - 100 cm) and the abundance ranges from 0 cysts•g^{-1} to a maximum value of 5 cysts•g^{-1} at 90cm. *Scrippsiella trochoidea* first appears from the 60 cm section and distributes in the upper part of the core, its abundance is less than 5 cysts•g^{-1}.

The identified species of toxic dinoflagellate cysts in the Luoyuan bay this time are more than in other sea areas in Fujian province[1, 7, 12, 13], additionally, the frequency of the red tide had an increasing trend in last 4 years, so the probability of toxic red tide breaking out is higher in the Luoyuan bay. In fact, from April 2002 to the middle ten days of May, there experienced the worst recorded marine toxicity event which caused 3 people to death, more than 50 people were poisoned by eating *Nassarius* in Luoyuan, Ningde, Xiamen and Putian [14], and the paralytic shellfish poisoning (PSP) toxin was detected from the samples collected in these poisoned person. Among the 6 toxic species in sediment samples from the Luoyuan bay, *Alexandrium minutum*, *A. tamarense* and *Gymnodinium catenatum* can produce PSP toxins, although these three species cysts' abundance is very low, the PSP toxin produced by the species of *Alexandrium* can be concentrated to high level by mussels [8], which may cause human death very easily when those mussels were eaten by accident. The residents nearby the area should pay more attention and avoid toxicity event breaking out again in the future.

3 Conclusion

a) Thirty species (belonging to 15 genera) dinoflagellate cysts were identified in the sediment samples of 100cm long KMZK5 core at the Luoyuan bay mouth, including 6 toxic species *Alexandrium affine*, *A. minutum*, *A. tamarense*, *Gonyaula spinifera*, *Gymnodinium catenatum* and *Scrippsiella trochoidea*.

b) The maximum abundance values of main dinoflagellate cysts are less than 20 cysts•g^{-1} and the

total cysts abundance ranges from 10 to 107 cysts•g^{-1}, in the upper part of the core (0 - 30 cm), the total dinoflagellate cysts abundance shows an increasing trend toward the top of the core and reaches relatively high values at 5 cm, whereas under 30 cm its abundance shows 3 peak values.

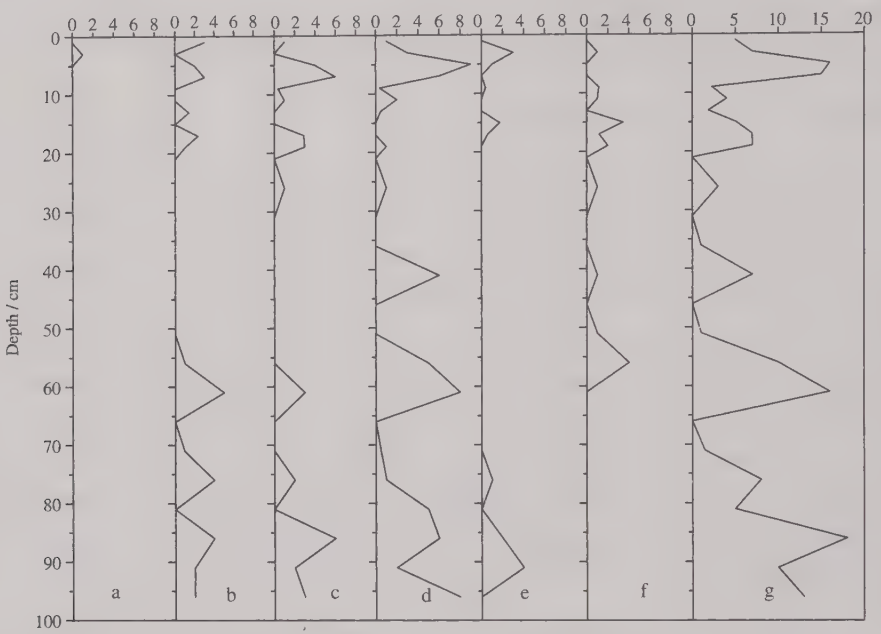

Fig. 3 Distribution of toxic dinoflagellate cysts

a: *Alexandrium affine*, b: *A. minutum*, c: *A. tamarense*, d: *G. spinifera*, e: *Gymnodinium catenatum*, f: *Scrippsiella trochoidea*, g: total abundance of toxic dinoflagellate cysts

c) The 6 toxic species are present discontinuously in low abundance values which limit to 10 cysts•g^{-1}, their percentage of the total cysts abundance changes in a fluctuating way. These toxic dinoflagellate cysts indicate that the Louyuan Bay sea area is well provided with the conditions for the toxic red tide to break out, the residents around the Luoyuan bay should pay more attention and avoid toxicity events happening in the future.

Acknowledgements

This project was supported by the National Natural Science Foundation of China under the contract No.40306018 and the Natural Science Foundation of Fujian Province under the contract No.2001F001.

References

[1] Fang Q, Lan D Z, Gu H F. Preliminary Study on Dinoflagellate Resting Cysts in Surface Sediments from Minjiang Estuary [J]. Marine Science Bulletin, 2004, 23(6): 21-25.

[2] Wang Z H,Qi Y Z,Jiang T J, Xu Z N. Vertical Distribution Of Dinoflagellate Resting Cysts In Recent Sediments From Daya Bay, The South China Sea [J]. Acta Hydrobiologia Sinica, 2004, 28(5): 504-510.

[3] Matsuoka K. Eutrophication process recorded in dinoflagellate cyst assemblage—a case of Yokohama Port, Tokyo Bay, Japan [J]. Science Total Environment, 1999, 231:17-35.

[4] Li S Q. Ways and methods for preventing red tide in Luoyuan bay [J]. Journal Of Fujian Fisheries, 2003, (4):71-74.

[5] Editorial committee of China's bays. Survey of China's bays (Seventh fascicule), the bays in north part of Fujian province [M]. Beijing: Marine Publishing Company, 1994. 256-257.

[6] Matsuoka K, Fukuyo Y. Technical Guide for Modern Dinoflagellate Cyst Study. Japan Society for the Promotion of Science[M]. Japan: Japan Society for the Promotion of Science, 2000: 1-90.

[7] Li C, Lan D Z, Fang Q, et al. Dinoflagellate cysts from sediments of Sansha Bay, Fujian [J]. Journal of Oceanography In Tai Wan Strait, 2003, 22(1): 38-46.

[8] Hallegraeff G M, Bolch C J, Blackburn S I, et al. Species of the toxigeni: dinoflagellate genus *Alexandruium* in southeastern Australian Waters [J]. Botanica Marina, 1991, 34: 575-587.

[9] Francesca Sangiorgi, Timme H. Donders. Reconstructing 150 years of eutrophication in the north~western Adriatic Sea (Italy) using dinoflagellate cysts, pollen and spores [J]. Estuarine Coastal and Shelf Science, 2004, 60: 69-79.

[10] Dale B. Dinoflagellate resting cysts: "benthic plankton" [A]. Fryxell G A. Survival Strategies of the Algae [M]. Cambridge: Cambridge University Press, 1983. 69-136.

[11] Anderson D M, Aubrey D G, Tyler M A, *et al.* Vertical and horizontal distributions of dinoflagellate cysts in sediments[J]. Limnology and Oceanography, 1985, 27(4): 757-765.

[12] Fang Q, Lan D Z, Gu H F. Preliminary study on dinoflagellate cysts in sediment of Xiamen Harbor [J]. Journal Of Fisheries Of China, 2003, 27(2): 137-142.

[13] Lan D Z, Li C, Fang Q. A preliminary taxonomic study on dinoflagellate cysts from sediments of main estuary and bays in Fujian Province, China [J]. Acta Oceanologica Sinca, 2005, 27(2): 70-78.

[14] Chen J R. Do not eat Nassarius any longer [N]. Amoy evening paper, 2002-05-28 (4).

罗源湾口柱状沉积物中的甲藻孢囊

孙爱梅[1]，李超[1]，蓝东兆[2]，祝跃[1]

(1. 厦门大学海洋学系、亚热带海洋研究所，福建 厦门 361005；2. 国家海洋局第二海洋研究所，福建 厦门 361005)

摘 要：通过对福建罗源湾口海域 KMZK5 柱状沉积物中甲藻孢囊的分析，共鉴定出 15 属 30 种甲藻孢囊。对比发现这 30 种甲藻孢囊是该湾以前未被记录的种类。其中 12 种是附近海域也未曾发现的种类，6 种为有毒种类：缘亚历山大藻、小型亚历山大藻、塔玛亚历山大藻、具刺膝沟藻、链状裸甲藻、锥状斯氏藻.同时对甲藻孢囊的主要属种和有毒种类的丰度、分布在垂直方向上的变化特征进行了初步研究.

关键词：甲藻孢囊；丰度；垂直分布；有毒种；罗源湾

Development of Sedimentary Environment in the Northeastern South China Sea Since the Last Glacial Stage

HUANG Yuanhui [1] , LAN Dongzhao [2]

1. *Department of Geography, East China Normal University, Shanghai* 200062, *China*

2. *Third Institute of Oceanography, State Oceanic Administration, Xiamen* 361005, *Fujian, China*

Abstract: Core D（21°23′02″N，116°47′13″E, water depth 405 m）was sampled from the upper slope from the northeastern South China Sea (SCS) and applied to analyze the sedimentary environmental change in this sea area since the last glacial stage. The results of grain size analysis, diatom analysis and detrital mineral analysis were well matched. We divided the core D into two layers. The surface sand layer (0 - 2 cm) consisted of residual sediments, which might be originally the sediment in the late Pleistocene and later suffered from being transformed in the post glacial transgression. The lower layer (2 - 130 cm) was quite different from the surface one, which might mainly result from a neritic sedimentary environment in the last glacial stage. Two sedimentary cycles could be detected in the core D: regression during Marine isotope stage (MIS) 4 to transgression during MIS 3 and regression during MIS 2 to transgression during the post glacial.

Keywords: diatom, grain size, sedimentary environment, the last glacial stage, the northeastern South China Sea

Introduction

Several previous investigations in the northeastern South China Sea (SCS) and its adjacent sea areas[1-2] primarily focused on the surface sedimentary environment [3-8], while few researchers have studied the sedimentary environmental change of the northeastern SCS since the last glacial stage [9-11]. In 1979, according to the geomorphologic and surface sedimentary characters, the South China Sea Institute of Oceanology, Chinese Academy of Sciences proposed a sedimentary model in the northeastern SCS [2], which could be compared with that of the Hanjiang Delta and Zhujiang Delta in Guangdong province. So, this model can serve as a fundamental basis for our study. In this paper, we aim to obtain more insights on the sedimentary environmental development in the northeastern SCS since the last glacial stage according to the multiple analytical results of core D.

1 Materials and methods

Core D (21°23′02″N，116°47′13″E；405 m water depth, 130 cm core length) was sampled using a piston corer from the upper slope of the northeastern SCS. A total of 33 sub-samples for diatom analysis

Received on April 17, 2006

were sampled at an interval of 4 cm, and 14 sub-samples for grain size as well as detrital mineral analysis were sampled at an interval of 10 cm. The thickness of each sample was 2 cm.

The 33 sub-samples for diatom analysis were prepared based on the method described by Lan [12]. After socked in distilled water for several hours, all samples were scattered with an ultrasonic scatter apparatus for 5 minutes and then filtered with a bolting cloth with holes of 15 μm. The remaining was transferred into centrifugal tubes and centrifuged for 3 minutes with a revolution of 1500 rpm. A cadmium heavy liquid with a specific gravity of 2.4 was used to enable the diatoms to suspend to the upper layer. The supernatant was placed on a cover slip and mixed with the help of a pipette in order to distribute the diatoms evenly on the cover slip. After the material had completely dried, the cover slips were transferred onto permanently labeled slides, mounted with Canada balsam. If possible, more than 300 diatom valves were counted for each sample, otherwise all diatoms on the entire three slides would be counted. Grain size and detrital mineral analyses were conducted for the 14 sub-samples according to the Specification for Oceanographic Survey (GB/T13909-92). Sub-samples for grain size analysis were treated as follows: sampling, drying, weighing, adding Sodium hexametaphosphate and water, and then soaking, filtering through the water sieve with a diameter of 0.063 mm. The grains left on the sieve (> 0.063 mm) were analyzed by a sieve analysis after drying, and the grains under the sieve (< 0.063 mm) were analyzed with a Mastersizer-2000 laser diffraction particle size analyzer (measurement range: 0.02-2000 μm). The results of grain size analysis were plotted on the Wentworth scale (Wentworth, 1922), and the sediments were classified using the Shepard triangular diagram (Shepard, 1954).

2 Results

2.1 Grain size analysis

According to the results of grain size analysis (Tab. 1), the core D could be divided into two layers: A thin surface layer of sand extended from 0 to 2 cm with its grain sizes ranging from 100 to 1000 μm and a mean grain size of 1.94 φ, whereas the sedimentary types of the thick lower layer (2 - 130 cm) were mainly dark gray clayey silts, the grain size ranging from 1 to 100 μm and the mean grain sizes ranging from 6.64 to 7.31 φ with an average of 7.04 φ.

Grain-size cumulative probability curve of the upper layer was quite different from the others (Fig. 1). It was constituted by three log-normal components, the rolling population (amounting to 15.36 %) , the suspension population (amounting to 8.76 %) and the saltation population (amounting to 75.88 %), together with a steep slope, moderate sorting, coarse truncation of 1.0 φ and fine truncation of 3.0 φ, reflecting a high-energy sedimentary environment.

Grain-size cumulative probability curves of the lower layer were primarily two log-normal or linear styles. According to the change tendency of the grain size, the lower layer could be divided into three segments as follows.

10 - 62 cm : A rolling population was absent. The content of the saltation population amounts to

18.7 % at most and all of the rest were suspension populations. From bottom upward, the grain sizes became coarser gradually and the contents of sand increased from 1.19 % to 13.66 %, reflecting a sedimentary environment with a low but growing energy.

Tab. 1 Results of grain size analysis of core D in the northeastern South China Sea

Sample No.	Depth / cm	Grain size distribution / %				Statistical parameters / φ			
		gravel	sand	silt	clay	Mz	σi	Ski	Kg
1	0 - 2	3.06	92.42	4.21	0.31	1.94	1.16	-0.13	1.45
2	10 - 12	0.00	13.66	61.53	24.81	6.64	2.34	-0.12	1.45
3	20 - 22	0.00	6.40	66.18	27.43	7.00	2.14	-0.05	1.52
4	30 - 32	0.00	3.17	74.33	22.50	6.87	1.57	0.14	1.13
5	40 - 42	0.00	8.72	66.76	24.52	6.72	2.08	-0.03	1.28
6	50 - 52	0.00	1.82	72.69	25.50	6.99	1.59	0.14	1.06
7	60 - 62	0.00	1.19	68.81	30.00	7.23	1.58	0.12	1.07
8	70 - 72	0.00	0.42	68.35	31.23	7.29	1.59	0.15	1.03
9	80 - 82	0.00	4.16	67.51	28.33	7.14	1.65	0.05	1.17
10	90 - 92	0.00	1.05	67.48	31.47	7.31	1.57	0.12	1.07
11	100 - 102	0.00	3.62	67.17	29.20	7.20	1.61	0.07	1.15
12	110 - 112	0.00	0.90	70.83	28.27	7.18	1.51	0.12	1.07
13	120 - 122	0.00	1.23	69.83	28.94	7.16	1.60	0.12	1.06
14	128 - 130	0.00	1.74	74.94	23.32	6.80	1.66	0.19	1.03

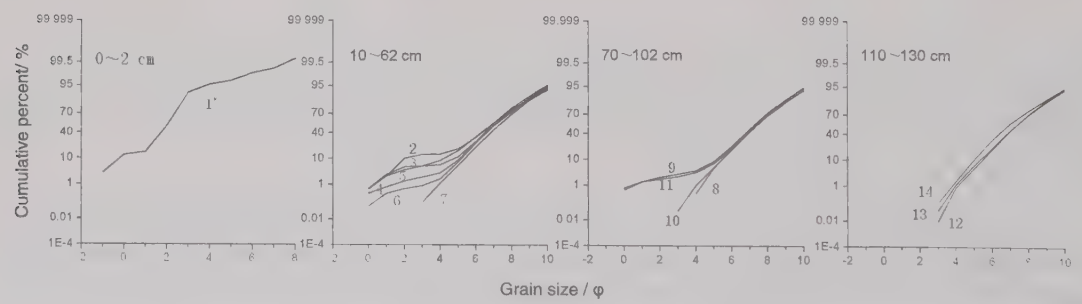

Fig. 1 Grain-size cumulative probability curves of core D in the northeastern South China Sea. The numbers from 1 to 14 refer to the sediment numbers in Tab. 1.

70 - 102 cm : No suspension population has been found in this segment. From bottom upward, the grain size became finer gradually (except for the sample 9) and the total content of silt and clay increased from 96.37 % to 99.58 %, reflecting an extremely low-energy sedimentary environment and the worsening hydrodynamic condition.

110 - 130 cm : All cumulative probability curves were slightly linear and almost overlapped. This segment was mainly composed of suspension population with a mean grain size ranging from 6.80 to 7.18 φ, indicating a low-energy sedimentary environment.

2.2 Diatom analysis

A total of 48 diatom taxa belonging to 17 genera (including varieties and forms) were identified. The diatoms with relatively high occurring frequencies were freshwater to brackish water species *Hantzschia amphioxys* (Ehr.) Grunow; brackish water species *Biddulphia gründleri* A. Schmidt; marine shallow water species *Melosira sulcata* (Ehr.) kützing, *Coscinodiscus excentricus* Ehrenberg, *Pyxidicula weyprechtii* Grunow, *Coscinodiscus radiatus* Ehrenberg, *Coscinodiscus argus* Ehrenberg, *Triceratium favus* Ehrenberg, *Coscinodiscus subtilis* Ehrenberg and *Coscinodiscus fimbriatus* Ehrenberg, oceanic species *Coscinodiscus nodulifer* A. Schmidt and *Hemidiscus cuneiformis* Wallich. Moreover, some other marine shallow water species such as *Actinoptychus undulatus* (Bail.) Ralfs, *Podosira stelliger* (Bail.) Mann, *Cyclotella stylorum* Brightwell, *Campylodiscus brightwellii* Grunow, *Diploneis incurvata* (Greg.) Cleve and *Triceratium reticulum* Ehrenberg have also been detected occasionally.

Based on the diatom assemblage, the quantitative distribution of some dominant diatom species and the diatom abundance of each sample, we grouped diatoms in the core D into 4 diatom zones(Fig. 2).

Diatom zone Ⅰ (112 - 130 cm): Diatom abundance in this zone was relatively high, with an average abundance of 1 389 valves/g. Eight species have been identified, with *Hantzschia amphioxys* as the dorminant species, and majority of the rest diatoms were marine shallow water species such as *Melosira sulcata, Triceratium favus* and *Coscinodiscus spp.*

Diatom zone Ⅱ (72 - 110 cm): A few diatoms have been found in most samples of this zone, but in the 72-74 cm interval the diatom abundance reached as high as 16 462 valves/g and 47 taxa of diatoms belonging to 16 genera (including varieties and forms) were identified, and the main diatom assemblage was *Melosira sulcata-Pyxidicula weyprechtii-Triceratium favus.* Most of them were common species which always showed up in the marine shallow habitat such as *Biddulphia gründleri, Campylodiscus brightwellii, Podosira stelliger* and *Cyclotella stylorum. Hantzschia amphioxys* has never been found in this zone.

Diatom zone Ⅲ (4 - 70 cm): Like the diatom zone Ⅰ, the diatom zone III had an average abundance of 1202 valves/g and eight species have been identified, most of which were *Hantzschia amphioxys* as well as some marine shallow water species.

Diatom zone Ⅳ (0 - 2 cm): Diatom abundance in this zone was 297 valves/g and eighteen species have been identified. A distinct characteristic of the diatom composition in this zone was that all of the three groups of diatoms with distinguishably different habitats could be identified in this zone, including coastal benthic species, marine shallow water species and oceanic species. The dorminnat species were the marine shallow water species *Melosira sulcata* and *Pyxidicula weyprechtii* (amount to 18.5 % and 12.3 % respectively), and the oceanic species *Coscinodiscus nodulifer* and *Hemidiscus cuneiformis* (amount to 18.5 % and 12.3 % respectively).

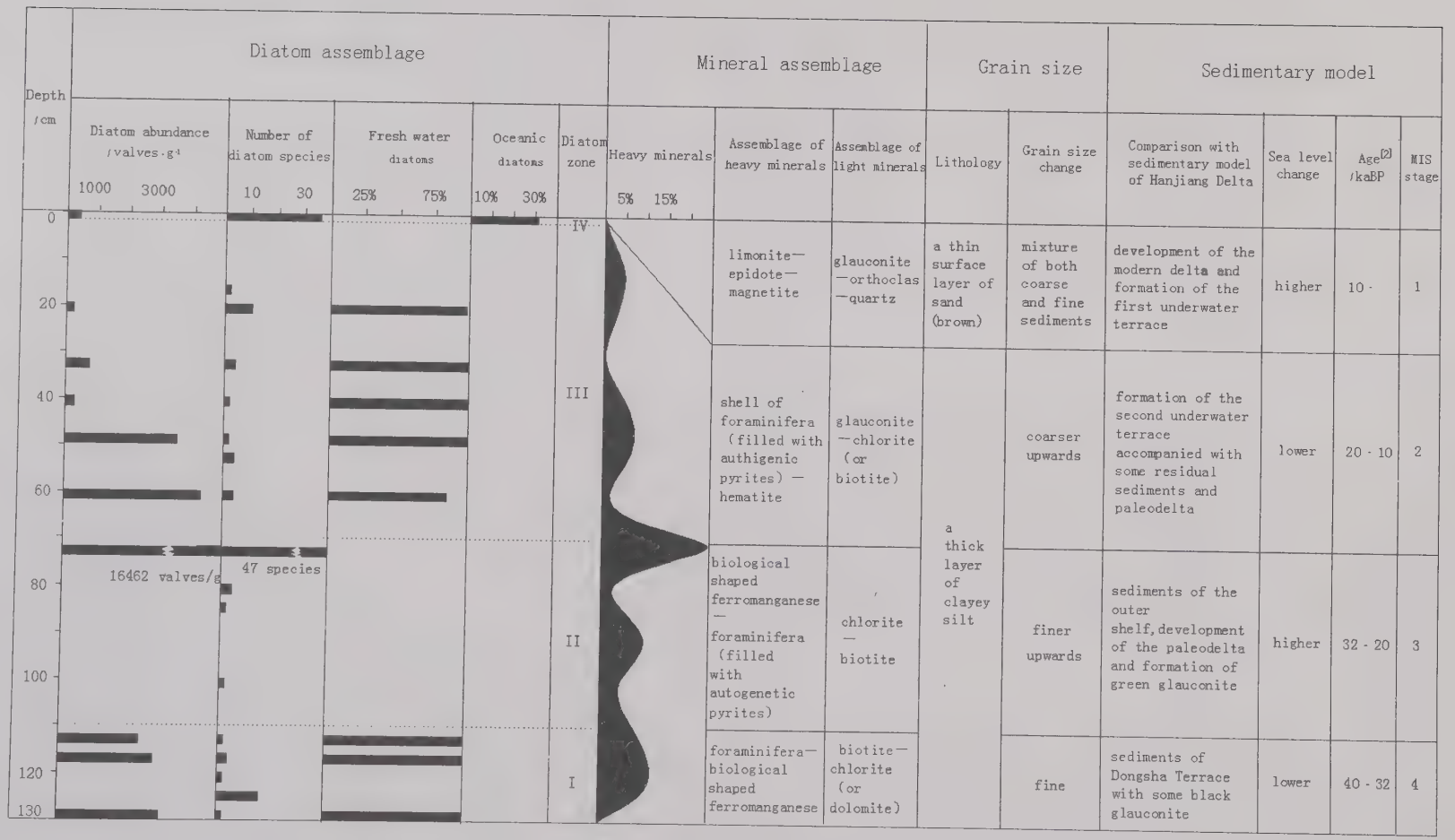

Fig. 2 Model of sedimentary environmental development in the vicinity of Core D in the northeastern South China Sea since the last glacial stage

2.3 Detrital mineral analysis

Twenty-one heavy minerals have been identified. Except for authigenic pyrite (appearing occasionally and always filling in the shell of foraminifera) and chlorite, terrestrial detrital minerals were commonly found, dominated by oxide and other silicate and hydroxide. Thirteen light minerals have been identified, including glauconite, chlorite, biotite, orthoclase and so on. The content percentages of the light and heavy minerals were shown in Table 2. Note that the percentage of heavy minerals reached as high as 24.52 % at the interval of 70 - 72 cm.

Tab. 2 Percentage of light and heavy minerals in Core D from the northeastern South China Sea / %

Depth/cm	0 - 2	10 - 12	20 - 22	30 - 32	40 - 42	50 - 52	60 - 62	70 - 72	80 - 82	90 - 92	100 - 102	110 - 112	120 - 122	128 - 130
Heavy mineral	0.25	4.21	3.14	0.57	5.64	6.75	1.91	24.52	2.62	12.01	4.48	8.81	11.78	1.31
Light mineral	99.75	95.79	96.86	99.43	94.36	93.25	98.09	75.48	97.38	87.99	95.52	91.19	88.22	98.69

3 Discussion

3.1 Sedimentary environment analysis

3.1.1 Surface layer sedimentary environment

Based on uranium-series dating result proposed by the South China Sea Institute of Oceanology, Chinese Academy of Sciences, the sedimentation rate of the surface layer in the northeastern SCS is 1.6×10^{-3} mm/a [2]. Presumably, the surface layer of core D might be the sediments as a result of the sea level rise since ca. 12.5 kaBP. This assumption is quite consistent with the results of grain size analysis and diatom analysis that the coarse sand dominated the sediments with a wide range of grain size distribution and the marine shallow water diatom taxa dominated the diverse-habitationed diatoms. The absence of *Hantzschia amphioxys* provides another testimony to prove that the surface layer might sediment in a shallow to bathyal sedimentary environment.

After the last glacial maximum (LGM), a global warming occurred. The shoreline moved landwards and part of the residual sediments from the outer shelf were taken to the core D and a thin surface layer came into being in the surface layer of core D. This kind of residual sediments distribute widely in many surface layer sediments of the continental shelf of China seas [13-15].

3.1.2 Lower layer sedimentary environment

This layer was quite different from that of the upper layer. We presume that sedimentary breaks might exist based on the results of diatom analysis. Two sedimentary cycles were recognized according to the results of grain size and diatom analysis. Therefore, the core D was divided into three segments: the lower segment (110 - 130 cm) , the middle segment (70 - 110 cm) and the upper segment (2 - 70 cm) .

The lower segment (110 - 130 cm): This segment was characterized by a large number of freshwater

to brackish diatom species *Hantzschia amphioxys* and the fine-grained sediment, reflecting a relatively low sea level and a short distance to the shore. We presume this segment to be a coastal to neritic sedimentary environment during the Marine Isotope Stage (MIS) 4.

The middle segment (70 - 110 cm): Most of the diatoms were marine shallow water species and no freshwater to brackish diatom species *Hantzschia amphioxys* had been identified. At the interval of 72 - 74 cm, both the diatom abundance and the species diversity simultaneously reached the peak of 16 462 valves/g and 47 taxa respectively. Cumulative probability curves changed from a linear style to a two log-normal style. Compared with the lower segment, grain sizes of this segment were smaller and turned gradually finer upward. As a result. We presume this segment to be a neritic sedimentary environment during MIS 3 with a relatively deep water depth and a higher sea level.

The upper segment (2 - 70 cm): The result of diatom analysis was quite similar to that of the lower segment with a majority of *Hantzschia amphioxys*, and its abundance reached the peak of 3427 valves/g at the interval of 60 - 62 cm. Cumulative probability curves were primarily a two log-normal style, and grain sizes grew bigger upward. We presume the sea level had dropped and the 60-62 cm interval might be the sediment during MIS 2 when the sea level had fell to its lowest position.

Additionally, amount of authigenic pyrite has been identified in the lower layer, implying a reducing environment at that time[11, 16-17].

In conclusion, we believe the lower layer resulted from a neritic sedimentary environment in the last glacial stage.

3.2 Sedimentary cycles

Combined with the sedimentary model proposed in 1979 by the South China Sea Institute of Oceanology, Chinese Academy of Sciences, we compiled the results of grain size analysis, diatom analysis and mineral analysis to draw a preliminary conclusion that two sedimentary cycles and four sedimentary stages could be detected in the core D.

Cycle 1 : regression during Marine isotope stage (MIS) 4 to transgression during MIS 3

During the period of MIS 4 (ca. 40 - 32 kaBP) lots of freshwater to brackish diatom species *Hantzschia amphioxys* showed up in the core D as the sea level fell. Afterwards, with the advent of MIS 3 (about 32 - 20 kaBP), as a result of global warming, a transgression occurred, so the grain sizes became finer gradually and marine shallow water diatom taxa replaced *Hantzschia amphioxys*.

Cycle 2 : regression during MIS 2 to transgression during the post glacial

As the global sea level falling happened during MIS 2 (about 20 - 10 kaBP), a large number of freshwater to brackish diatom species *Hantzschia amphioxys* appeared in the core D and reached the peak at the 60 - 62 cm interval. The climate turned warmer quickly after the post glacial stage. Accordingly, the sea level rose to the present water depth in a short time. During this period the sedimentation rate was quite low and only a 2 cm thin layer of sediment has been formed in the core D.

4 Conclusion

a) The characteristics of the surface upper layer of core D in the northeastern SCS were quite different from those of the lower layer. The grain size analysis showed that coarse sands and fine sands coexisted while coarse sands dominates the sediments. The diatom analysis showed that marine shallow water species and oceanic species coexisted while the marine shallow water species dominated the diversely habitating diatoms. We presume the surface layer is a residual sediment. As a result of the neritic sedimentary environment since the last glacial stage, regular change of the grain sizes and the presence of freshwater to brackish water diatom species *Hantzschia amphioxys* characterized the lower layer.

b) The results of diatom, grain size and mineral analyses were well matched with each other, revealing that two sedimentary rhythms and four stages could be detected in the core D.

Acknowledgements

We thank Prof. Chen Chenghui for his helpful suggestions and Lan Binbin for his assistances in the pretreatment of the diatom analysis samples. This study was supported by the open fund of Key Laboratory of Marine Sedimentology and Environmental Geology, State Oceanic Administration (Grant No. MASEG200401).

References

[1] Liu Z S, ZHAO H T, FAN S Q, et al. Geology of the South China Sea [M]. Beijing: science press. 2002, 14.

[2] South China Sea Institute of Oceanology, Academia sinica. Report of a multidisciplinary investigation in the South China Sea (No. 2) [M]. Beijing: science press. 1985, 2-128.

[3] Luo Y L. A preliminary study on the surface sediment types and their grain size characteristics of the northeastern part of the South China Sea. Tropic Oceanology. 1985. 4 (1): 33-41.

[4] Huang B Q, Jian Z M. Late Quaternary changes of paleoproductivity in the northeastern South China Sea [J]. Marine geology & Quaternary geology, 2000, 20 (2): 65-68.

[5] Xu J, Huang B Q, Chen R H, et al. Distribution of foraminifera in surface sediments of northeastern South China Sea and its environmental implications [J]. Journal of Tropical Oceanography, 2001, 20 (4): 6-13.

[6] Meng Y, Yan S Z, Chen R H, et al. Composition analysis of the biogenic and mineral clastics In the surface sediment of the northeastern South China Sea and its paleoenvironmental significance [J]. Marine geology & Quaternary geology, 2001, 22(3): 17-22.

[7] Chen R H, Wang D J, Xu J, et al. Calcium and siliceous microfossil in the surface sediments of the northeastern South China Sea and their relationships with the sedimentary environment [J]. Marine geology & Quaternary geology, 2003, 23 (4): 15-21.

[8] Chen R H, Xu J, Meng Y, et al. Microorganisms and carbonate lysocline depth and CCD in the surface sediment

of the northeastern South China Sea [J]. Acta Oceanologica sinica, 2003, 25(2): 48-56.

[9] Duan W W, Chen F, Wei K Y, et al. Calcareous nannofossil in the northeastern South China Sea since the last 15ka and its significance of paleo-oceanography [J]. Marine geology & Quaternary geology, 1998, 18(1): 13-22.

[10] Wei K Y, Lee M Y, Duan W W, et al. Late glaciation-Holocene paleo-oceanography of the northeastern South China Sea: core RC26-16 [J]. Marine geology & Quaternary geology. 1999, 19(3): 19-27.

[11] Yang Q H, Zhang F Y, Lin Z H, et al. On mineralogical and geochemical records of paleosedimentary environmental variation in the northeastern South China Sea since the late Pleistocene [J]. Acta Oceanologica sinica, 2004, 26(2): 72-80.

[12] Lan D Z, Cheng Z D, Liu S C. Diatoms in late quaternary sediments from the South China Sea [M]. Beijing: China Ocean Press. 1995.

[13] Wang P X, Min Q B, Bian Y H, et al. Preliminary study on Quaternary transgressional stratigraphy in East China [J]. Acta Geologica Sinica, 1981, (1): 1-13.

[14] Wang P X, Zhang J J, Zhao H Q, et al. Foraminifera and Ostracoda in bottom sediments of the East China Sea [M]. Beijing: China Ocean Press. 1988, 298-301.

[15] Wang Z H, Guo Z Y, Chen Z Y, et al. Relict sediment and its environmental implication in Pingbei area, East China Sea continental shelf [J]. Journal of East China Normal University (Natural Science). 2002, 1: 81-86.

[16] Chu F Y, Chen L R, Shen S X, et al. Origin and environmental significance of authigenic pyrite from the south Yellow (Huanghai) Sea sediments [J]. Oceanologia et Limnologia Sinica, 1995, 26(3): 227-233.

[17] Wang L, Wang P. Late Quaternary paleoceanography of the South China Sea: glacial-interglacial contrasts in an enclosed basin [J]. Paleoceanography, 1990, 5 (1): 77-90.

南海东北部末次冰期以来沉积环境演变

黄元辉[1]，蓝东兆[2]

(1. 华东师范大学地理系，上海 200062

2. 国家海洋局第三海洋研究所海洋与海岸地质环境开放实验室，福建 厦门 361005)

摘 要：利用南海东北部上陆坡处所取的 D 孔（21°23′02″N，116°47′13″E,水深 405 m）进行硅藻分析，结合粒度分析与碎屑矿物分析结果，探讨该海域末次冰期以来沉积环境演变过程。结果表明：粒度与硅藻分析结果较为吻合，共同显示 D 孔可分为上下两层，上层（ 0 - 2 cm）的砂质沉积层为经冰后期海进过程改造的晚更新世残留沉积层；下层（2 - 130 cm）主要是末次冰期形成的浅海沉积。整个柱样可反映出海洋同位素 MIS 4 期海退至 MIS 3 期海进与 MIS 2 期海退至冰后期海进的沉积韵律。

关键词：硅藻；粒度分析；沉积环境；末次冰期；南海东北部

Influence of Seawall Line Choice on Tide Lock Drainage in Tidal Flat Inning

—— Cangdongpian Inning Area on the west part of Tiaozini Sand as a case study

LI Jialin [1], WANG Yanhong [2], ZHANG Renshun [3]

1. *Institute of Human Inhabiting Environment, Ningbo University, Ningbo* 315211, *Zhejiang, China*
2. *River and Harbor Department, Nanjing Hydraulic Research Institute, Nanjing* 210024, *Jiangsu, China*
3. *Institute of Ocean and Coastal Wetland. Nanjing Normal University, Nanjing* 210097, *Jiangsu, China*

Abstract: Most of the flood from the wide inner lowland plain discharges through tide locks on coast, and the influence of tidal flat inning projects on the tide lock drainage must be solved by seawall line choice. Taking the Cangdongpian inning area on the west side of Tiaozini Sand as a case study, the paper analyzed the compages and validity of ebb tide water to maintain the flood discharge creek below the tide lock for different projects of seawall line. Result indicates that a rational seawall line program has little influence on the flood discharge of lock during the mean tide or general spring tides, but has certain influences during a storm surge or an extreme spring tide in autumn. However it could be resolved by several times of artificial scour on the creek.

Keywords: tidal flat; inning; tide lock; discharge; influence

Introduction

The Jiangsu coast with a total length of 954km is located on the middle west of Huanghai Sea (Yellow sea) between the Shandong Peninsula and Changjiang River (Yangtze River) mouth. Its tidal flat is very wide and most of that is gradually growing. Reclamation of tidal flat has a buffer function on the cultivated land decrease, and it is very important to the balance of total amount of cultivated land. Flood discharge from the wide lowland plain behind the mud coast mostly depend on tide locks on seacoast, and the influence of tidal flat inning project on tide lock drainage should be solved through seawall line choice. Unsuitable seawall projects could enhance sedimentation in creeks below the tide lock, weaken the flood drain function of tide lock and accelerate abandon of tidal lock. Take Cangdongpian inning area on the west part of Tiaozini Sand as a case study, the paper analyzed the influence of seawall line choice of inning project on compages and validity of ebb tide water to maintain the flood discharge creek below the tide lock for different projects of seawall line.

1 Regional background and choice of seawall line for different designed inning projects

After the northward shift of Yellow River in 1855, Jiangsu coast no longer had abundant sediment

Received on August 10, 2006

supply and the erosion-deposition condition of the Radiate Sand Ridges changed rapidly. Tiaozini Sand is just located in the inner part of the well-known offshore Radiate Sand Ridge area. Due to the special dynamic sedimentary condition, the East China Sea advancing tidal waves from south to north converge with the South Yellow Sea rotary tidal waves from north to south (Fig.1), and the development of tidal creek systems and tidal basins is very sensitive to the hydrodynamic changes [1].

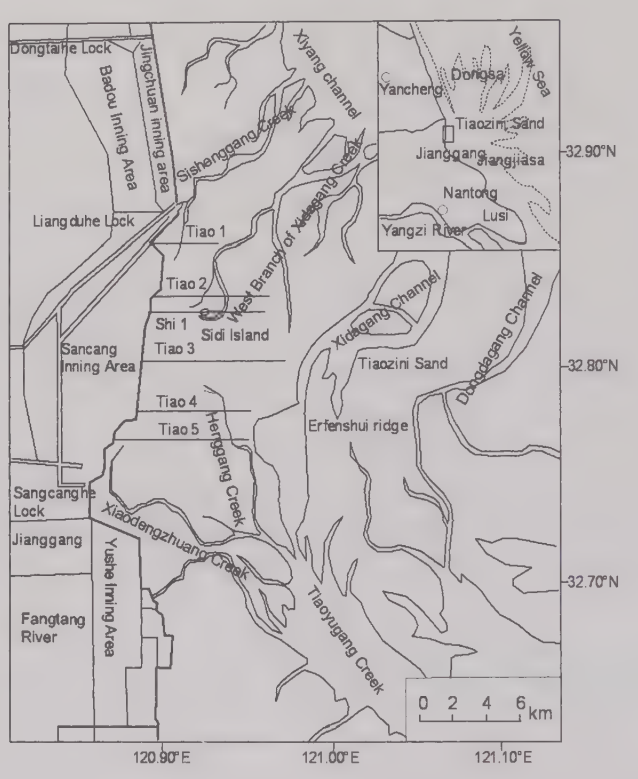

Fig. 1 The location of study area (According to Jan.2003 TM image)

The study area, western part of Tiaozini Sand, is connected with the Sancang inning area reclaimed in 1997 (Fig.1). Tidal current is complicated and strong in the area, and the tidal range increases gradually from north to south. And tidal basin systems are well developed on the tidal flat. The Liangduhe tide lock, built in the 1970s, is one of the most important locks in Dongtai County. It protrudes from the old embankment that was built in 1958. Flood from the lock could reach the outside tidal channel by a short creek of Sishenggang, added up with the frequent artificial scouring to the downstream creek, the lock ran favorably in the past decades. Besides, there developed a tidal creek named Erfenshui between the nearshore flat and the Tiaozini Sand before the 1980s. The creek ran approximately parallel to the coastline before the 1980s. The creek was connected southwardly with the Xiaodengzhuanggang creek outside of Jianggang and northwardly with the Sishenggang creek. Width depth of the cross section of waterway of the creek could reach more than 2.5 km and 0.9 m during spring tide at that time, however 2.0 km and 0.7 m during normal tides, respectively. During a spring rise and ebb circle, 0.1012×10^8 m^3

water volume flowed over the ridge of Erfenshui from south to north, and 0.030 2×10^8 m^3 during a neap tide[2,3]. The water entered the Sishenggang creek and played important roles in maintaining the flood discharge capacity of the Liangduohe tide lock.

From 1999 to 2003, elevation and topography of 5 sections in the study area were investigated, 15 times altogether. Based on the analysis of the investigated data and 11 remote sensing images (MSS, TM and ETM) since 1980, developing tendency of mean high water line on the tidal flat, formation process of the sand island (Sidi island) and development of tidal creeks near Tiaozini Sand are discussed. Meanwhile, relationship between flat elevation of seawall line and water level of tidal characteristic numbers, west-moving boundary of Xidagang and Henggang creeks, ecological influence of inning on the original salt marsh, integrated benefits of inning project and so on are studied as well. Based on these studies, three candidate inning projects of seawall line were designed, for analyzing the influence of tidal flat inning on the drainage of Sishenggang creek below tide lock (Fig.2).

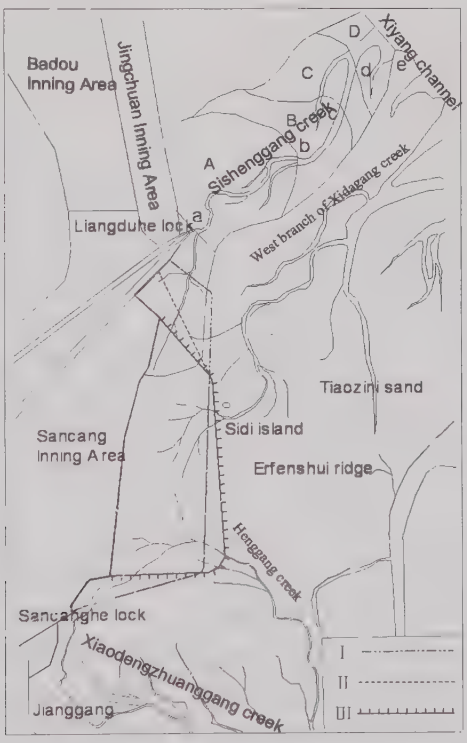

Fig. 2 The sea wall line of inning programs

2 Tidal creek system on the study area and subsection of the creek below Liangduhe tide lock

Cangdongpian inning area is between Liangduohe tide lock and Sancanghe tide lock. Creek systems on the tidal flat are mostly branches or tips of the tidal creek systems that belong to the tidal basins of Sishenggang, west branch of Xidagang, west branch of Henggang and Xiaodengzhuanggang.

Sishenggang tidal basin, located in the north part of the flat, discharge flood from Liangduhe River and a thin layer of tide water on tidal flat into offshore channel on the north Cangdongpian flat during the later ebb phase. West branch of Xidagang creek extends westward into the planned inning area from the south of Sidi Island and forms a tidal basin. It discharges tide water in the middle part of the planned inning flat to the Xiyang channel. The west branch of Henggang creek and Xiaodengzhuang creek extend into the planned inning flat from south-east and south, respectively. Tide water in the east and south parts of the flat flows by into the Tiaoyugang creek in this tidal basin.

Expect some tidal creeks and their vicinities, the surface elevation of the planned Cangdongpian inning area flat is mostly higher than the mean high water level. The planned seawall line will cut the branch creeks of Sishenggang, Xidagang, West Henggang and Xiaodengzhuanggang main creek. Consequently, the ebb tide water volume of these creeks will decrease.

Original tidal creek systems are usually selected as waterways for flood discharge from the plains behind tide locks. The creek could be divided into three stretches from tide lock to tidal channel or open sea. [4] Usually, the upper stretch means the artificial creek section or the section located on the supra-tidal flat. This stretch is similar to a river. Because the boundaries are restricted by artificial banks or high supra-tidal flats, the waterway is generally stable and straight. The lower stretch has developed on the lower inter-tidal flat, and has no stable banks. Because of the complexity of tidal current and wave on lower flats, the creek is generally wide and shallow. It can move widely on the flat. The middle stretch, on high inter-tidal flat, generally has an obvious trough. Because of the binary structure of sediment layers on the tidal flat, the creek is usually bended there. The flood discharging rivers in Jiangsu province, such as Xingyanggang River, Doulonggang River and Dongtai River usually develop more than one bend below tide locks, the waterway could even choose a short cut when the creek is deeply bended. The creek below tide lock is obviously affected by bidirectional hydrodynamics, landward and seaward. The upper stretch is mainly controlled by the runoff from the tide lock while the lower stretch by tidal current and wave dynamics. The middle stretch is a transitional part that is affected by land-ocean interaction greatly.

Based on results of flat elevation survey and interpretation of remote sensing images, subsection of the creek below the Liangduohe tide lock was divided as in Fig. 2. The upper stretch, from north and south tide locks of Liangduhe to the juncture (point a) of artificial waterways, has concreted banks, with lengths of 0.65 and 0.68 km, respectively. From the point a to the point b is the middle stretch, located on the middle part of the upper inter-tidal flat with a length of 5.1 km. From the point b to the point e is the lower stretch, on the lower part of inter-tidal flat with a length of 5.3 km.

3 Influence of various seawall line programs on the water mass supplied to the creek below the Liangduhe tide lock

As tidal waves spread from the lower section to the upper one along the gutter, stationary waves will come into being. Furthermore, the sedimentation process of silt carried by tidal waves has an obvious sediment delay effect on the tidal flat. Sediment will enrich near the tide lock gate and only the ebb tide

current can transport it to sea. Otherwise, the drain flow below tide lock will not smooth. Water mass supplied to the creek below the Liangduhe tide lock is composed of the tidal current from the South Tiaozini ridge which traverses over the ridge of Erfenshui and flows into the Sishenggang creek, the river discharge from north and south tide locks of Liangduhe river, the intertidal storage volume of anthropical river below tidal lock, the thin layer of tide water on the tidal flat in the later ebb phase and storage volume in the creek system of Sishenggang tidal basin, et al. Tidal flat reclamation will change the volume of ebb water to the creek.

3.1 Composition and change of water volume to the creek below the Liangduohe tide lock

3.1.1 Tide water flow over the ridge of Erfenshui from south to north

As mentioned above, tide water traversing over the ridge of Erfenshu from the south has played an important role in maintaining the flood drain capability of the creek below the Liangduohe lock. Recently, due to large-scale deposition and accretion of the tidal flat, the Erfenshui creek was filled gradually. In the early 1980s, the frequency of traverse of tide water over the ridge of Erfenshui from south to north is about 20 days per month. However, in the early 1990s, it was only about 6 to 7 days per month, and the water valume decreased little by little with silting of the creek. In October 1999, the width of Erfenshui creek was only about 350 meters. And the elevation of Erfenshui creek bottom was 3.45 meters, higher than the mean spring high water level. This indicated that there was almost no tide water to the Sishenggang creek from south of Erfenshui Ridge, even during the spring tide. The flat 4 000 meters outside the seawall is lower than the mean spring water level. But the tidal water that traversed over the ridge flows into the Xidagang main channel directly or by west branches of Xidagang creek, rather than by the Sishenggang creek. Consequently, it made no contribution to the capability of flood drain of Sishenggang creek. Profile survey of Tiao4 in the past years showed that the Erfenshui creek was shrinking slowly. In Jan., 1999, the Erfenshui creek was about 1 500 meters wide on the profile, and seemed wider in the summer of 1999. But it was connected with the Xiyang channel directly, rather than by the Sishenggang creek. The elevation of the creek bottom was mostly higher than the mean spring water level and there was no tidal current at average tides in 2001. It means there was almost no tidal water traversing over the ridge of Erfenshui to the Sishenggang creek after 2001. So the seawall line choice project does not need to consider the influence of tidal water which traversed over the ridge of Erfenshui to the Sishenggang creek.

3.1.2 River discharge

The north and south tide locks of Liangduhe River were built in 1972 and 1983, respectively. Based on the statistics of hydrologic data in the past years, the yearly average water discharge of the two locks, the water discharge in the flood and dry seasons, the each tidal circle water discharge on the average during flood and dry seasons were calculated respectively (Tab. 1).

3.1.3 Tide water storage volume of the creek below the Liangduhe River tidal lock

Based on the analysis of tide data below the Liangduhe river tide locks, levels of mean high tide, mean high spring tide, autumnal extra high spring tide and high water of storm surge are 2.62 m, 3.00 m,

3.50 m and 4.00 m, respectively. Tide water storage volume of the creek downstream of south and north Liangduhe tidal locks can be calculated as follows:

$$V = (A_1 + A_2) \cdot L \cdot h / 2 \quad (1)$$

Where V is the volume of tide water storage in the tidal creek; A_1 and A_2 are the breadths of the creek at mean low water and high water respectively; L is the length of the creek; and h is the corresponding tide range.

Tab. 1 Water discharge of Liangduohe River

Items	Yearly water discharge on the average / 10^8 m^3	Water discharge in flood seasons on the average / 10^8 m^3	Water discharge in dry seasons on the average / 10^8 m^3	Water discharge per tide circle / 10^5 m^3	Water discharge in flood seasons per tide circle / 10^5 m^3)	Water discharge in dry seasons per tide circle / 10^5m^3
North lock	1.95	1.38	0.57	2.79	5.98	1.21
South lock	1.59	1.12	0.46	2.26	4.85	0.98
Total	3.53	2.5	1.03	5.05	10.83	2.19

Then the volume of tide water storage in the tidal creek below Liangduhe River tide locks at different water levels could be calculated. The results are shown in Tab. 2.

Tab. 2 Storage volume of anthropical river below Liangduhe River tide locks at different tidal water levels / 10^5 m^3

Tide level	Mean high water	Mean high water line of general spring tide	Mean high water line of spring tide in autumn	High water line of storm surge
Storage volume of tide water	1.14	1.42	1.68	1.97

3.1.4 Water mass supplied to the creek at middle and nether parts of creek below Liangduhe river tide locks

Water mass supplied to the creek at middle and nether parts of creek comes from the water mass on the tidal flat between the Chuanlonggang creek system and the south branch of Xidagang creek system. According to the analysis of TM image (January 2003) and survey on the topography of tidal flat, the tidal flat of the nether part of Sishenggang creek system is disported into 4 sections. There are parts A, B, C and, the part D where water mass flows into the inlet of Xiyang Channel (Fig.2). The area of tidal flats and water volume per tide were calculated as in Tab. 3.

Tab. 3 Flats area and water volume per tide at middle and nether parts of Sishenggang creek

section	A	B	C	D
area / km^2	10.56 *	3.10	12.82	3.48
water volume / 10^5 m^3	10.56	3.10	12.82	3.48

* Depth of water mass supplied creek is regarded as 10 centimeters because the tidal flat is almost all bare.

3.1.5 Loss of tide water storage volume caused by reclamation

The tail of Sishengang creek to the south of Liangduohe tide lock has shrunk gradually in recent decades. About 2.0 km^2 of high flat on both sides of the creek is out of the reach normal tide water inundation, and the *Imperata cylindrical var.major* community has become the main vegetation. The other 5.5 km^2 high flat has been densely covered by *Spartina alterniflora* and *Suaeda salsa*. Tide water from the flat could only supply the Sishengang creek during spring tide.

The project of reclamation will cut the upper and middle reaches of the Sishenggang creek. It may cause decrease of water storage volume of it. 2.05 km, 1.15 km and 0.55 km of the Sishengang creek with average widths of 30 m, 20 m and 15 m will be cut in the programs Ⅰ, Ⅱ and Ⅲ, respectively. Therefore, loss of water volume of Sishenggang creek caused by reclamation could be calculated. The results are shown in Tab. 4.

Tab. 4 Loss of water volume of Sishenggang creek caused by inning

Program	Ⅰ	Ⅱ	Ⅲ
High water level of storm surge	1.15×10^5 m^3	0.36×10^5 m^3	0.17×10^5 m^3
Mean high water line of autumnal spring tide	0.84×10^5 m^3	0.25×10^5 m^3	0.11×10^5 m^3
Mean high water line of general spring tide	0.54×10^5 m^3	0.13×10^5 m^3	0.06×10^5 m^3
Mean high water line	0.30×10^5 m^3	0.05×10^5 m^3	0.01×10^5 m^3

Because the elevation of most of the tidal flat in the planed reclamation is higher than the mean high water of spring tide, the water volume loss could only occur during spring tides, autumnal spring tides and storm surges. The inundated area by storm surge is regarded as the whole reclaimed area, that by the autumnal spring tide as the area of the dense *Suaeda salsa* community distributed, and that by normal spring tide as area of the sparse *Suaeda salsa* community. There is no water mass supplied to the creek at the mean high water line in all the three programs. Tide water loss caused by different programs is shown in Tab. 5.

Tab.5 Tide water loss caused by the reclamation for different programs

Program	Ⅰ	Ⅱ	Ⅲ
Storm surge	2.32×10^5 m^3	1.92×10^5 m^3	1.01×10^5 m^3
Autumnal spring tide	1.67×10^5 m^3	1.43×10^5 m^3	0.75×10^5 m^3
Spring tide	0.30×10^5 m^3	0.13×10^5 m^3	0.06×10^5 m^3
Mean high water line	0	0	0

* Depth of water mass supplied to the creek of *Spartina alterniflora* and dense *Suaeda salsa* flats is regarded as 15 cm, depth of water mass supplied to the creek of sparse *Suaeda salsa* and bare flats is regarded as 10 cm.

3.1.6 Newly added rainfall supplied to the Sishenggang creek

Currently (before reclamation), the tidal flat of the planed reclaimation area belongs to tidal basins of Sishenggang, west branch of Xidagang, Henggang and Xiaodengzhuanggang. Precipitation on the tidal flat is shared by all the tidal basins. After reclamation, all precipitation in the area will be supplied to the Sishenggang creek through an artificial water lock. About 70 % of annual precipitation in Dongtai County occurs during rainstorms that could form water flow on tidal flat. The runoff rate of rainstorm on the supra tidal flat is regarded as 0.7. Other rains hardly have runoff yield due to quick infiltration. So the newly added rainfall supplied to the Sishenggang creek could be calculated as in the equation (2).

$$Q = (M_1 - M_2) \cdot U \cdot 0.7 \cdot b \quad (2)$$

Where Q is the added rainfall water mass supplied to the Sishenggang creek. M_1 is the reclamation area. M_2 is the area of Sishenggang basin that will be enclosed. U is the annual precipitation of the study area. b is the runoff rate of rainstorm on supra tidal flats (the value is 0.70).

Based on the equation (2), the newly added rainfall for the programs Ⅰ, Ⅱ and Ⅲ could be calculated. It is 0.28×10^5, 0.275×10^5 and 0.27×10^5 m^3, respectively.

3.2 Validity of water mass supplied to the creek to maintain the drain capability of creek below tide locks

Because of the difference of position, time, water volume and sediment concentration, various water masses supplied to the creek play different roles in maintaining the drain capability of creek below the tide lock. Generally, nearer to the tide lock, stronger the water scouring capability is. So the rain discharge from tide locks and the water storage volume in the artificial river are the most valid water masses to maintain the drain capability of creek. Water mass supplied to the creek in the outlet of the creek is of no avail for maintaining the drain capability of the creek. Because many variables are involved, it's hard to quantitatively estimate the validity currently. In this study, only the position and validity of water mass supplied to the creek are considered, and the linear equations of (3), (4) and (5) are employed.

$$\alpha_i = L_i / L \quad (3)$$

Where α_i is the coefficient of validity to maintain the drain capability of the creek water depth. L_i is the length of creek from the entrance to the outlet of the creek. L is the length of Sishenggang creek.

$$B_i = \alpha_i \cdot V_i \quad (4)$$

Where B_i is the validity of water mass supplied to the creek. V_i is the amount of water mass. And i is the number of water mass supplied to the creek.

$$P_i = B_i / \sum_{i=1}^{n} B_i \quad (5)$$

Where P_i is the contribution rate of water mass supplied to the creek.

Based on the equations (3), (4) and (5), we can calculate the contribution rate of water mass supplied

to the creek to maintain drain capability of Liangduhe creek. The results are shown in Tab. 6.

Tab. 6 Water volume and contribution rate to maintain the drain capability

Item	Rainfall discharge	Storage volume of artificial river	Storage volume of Sishenggang creek and tidal flats	Newly added rainfall	A	B	C	D
α_i	1	1	1	1	0.608	0.526	0.12	0
V_i Program I	5.05	1.97	3.47(storm surge)	0.28	10.56	3.10	12.82	3.48
		1.68	2.51(autumnal spring tide)					
		1.42	0.84(spring tide)					
		1.14	0.30(mean high water)					
V_i Program II	5.05	1.97	2.28(storm surge)	0.275	10.56	3.10	12.82	3.48
		1.68	1.68(autumnal spring tide)					
		1.42	0.26(spring tide)					
		1.14	0.05(mean high water)					
V_i Program III	5.05	1.97	1.18(storm surge)	0.27	10.56	3.10	12.82	3.48
		1.68	0.86(autumnal spring tide)					
		1.42	0.12(spring tide)					
		1.14	0.01(mean high water)					
P_i Program I	24.80	9.70	17.00(storm surge)	1.40	31.50	8.00	7.60	0
	26.40	8.80	13.10(autumnal spring tide)	1.50	33.60	8.50	8.10	0
	29.40	8.30	4.90(spring tide)	1.60	37.30	9.50	9.00	0
	30.90	7.00	1.80(mean high water)	1.70	39.20	10.00	9.40	0
P_i Program II	26.40	10.30	11.90(storm surge)	1.40	33.50	8.50	8.00	0
	27.60	9.20	9.20(autumnal spring tide)	1.50	35.10	8.90	8.50	0
	30.40	8.60	1.60(spring tide)	1.70	38.70	9.80	9.20	0
	31.40	7.10	0.30(mean high water)	1.70	39.90	10.10	9.50	0
P_i Program III	28.00	10.90	6.50(storm surge)	1.50	35.60	9.00	8.50	0
	28.50	11.10	4.80(autumnal spring tide)	1.50	36.20	9.20	8.70	0
	29.70	11.60	0.70(spring tide)	1.60	37.80	9.60	9.00	0
	29.90	11.70	0.06(mean high water)	1.60	38.00	9.70	9.04	0

* A, B, C and D are four sub-basins which supplied middle and lower reaches of Sishenggang creek.

Analysis of Table 6 shows, the amount of water mass that is supplied to the creek is the largest part of all water items. Its contribution rate to maintain the drain capability of Sishenggang creek is more than 45%, though its validity is lower. The contribution rate of rain discharge and storage volume of anthropical river is more than 30% too. The contribution rate of water volume of storage volume of Sishenggang creek and water mass of tidal flats is ranging from in 0.06 % - 17.00 % at different programs. The contribution rate of newly added rainfall will change in 1.40 % - 1.70 %.

Different programs could only cause the change of water volume of storage water mass of Sishenggang creek, the tide water on tidal flat in the later ebb phase and the newly added rainfall. Other items will not change. So the influence of different inning projects on the drain capability of Sishenggang creek can be regarded as the difference between water volume of storage volume of Sishenggang creek,

water mass of tidal flats and newly added rainfall. The results are showed in Tab. 7.

Tab. 7 Influence on the drainage of Liangduo tide lock caused by reclamation

Tide level	Storm surge	Autumnal spring tide	Spring tide	Mean high water
Program I	15.6%	11.6%	3.3%	0.1%
Program II	10.5%	7.7%	-0.1%	-1.4%
Program III	5.0%	3.3%	-0.8%	-1.54%

Because the elevation of tidal flats in the inning area is higher than the high water line of spring tide, the seawall line choice of project I almost has no influence on the drain capability of Sishenggang creek. The influence is only 0.1 % and 3.3 % at the mean high water line and high water line of spring tide. In the programs II and III, seawall line choice is beneficial to maintaining the drain capability of Sishenggang creek because loss of water volume of upper and middle parts in the Sishenggang basin will be very little and the rainfall in middle and south parts of inning area will flow into the Sishenggang creek.

During storm surge and autumnal spring tide, the influence of inning project on the drain capability of Sishenggang creek is notable. The decreases are 15.6 % and 11.6 % in Program I , 10.5 % and 7.7 % in Program II , and 5.0 % and 3.3 % in Program III respectively. The frequency of the water level higher than 3.0 m is 7 % (47 times one year), higher than 3.5 m in the autumnal spring tide is 1 % (6 or 7 times one year). And 4.0 meters in the storm surge is 0.1 % - 0.3 % (1 or 2 times one year). Therefore, the influence on the drain capability by the inning project could be resolved by some times of artificial scour.

3 Conclusion and discussion

Based on the analysis of the influence of different inning programs on the drain capability of Sishenggang creek, it is concluded that inning of supra tidal flats will only cut part of storage volume of the upside Sishenggang creek at the mean high water line. The decrease of water volume is quite notable during spring tide, autumnal spring tide and storm surge. It may cause silting at the Sishenggang creek below Liangduhe tide locks. Because the possibility of very high water is low, the settled sludge can be scoured artificially. Therefore, the program III is considered to be the most reasonable one. That is to say that reasonable seawall line choice may decrease the influence and maintain the drain capability of creek below the tide lock with current technology.

Due to the difference in the position and time of water mass flow to the creek, and water volume and sediment concentration of different water masses, various water masses supplied to the creek play different roles in maintaining the drain capability of creek below tide locks. In this study, we only consider the position and validity of water mass supplied to the creek and uses the linear equation to calculate it. In addition, inning of supra tidal flats would not cause adjustment of the equilibrium state in tidal flats, but the twig of tidal creek may be cut off and the area of tidal basin will decrease. It may change the hydrodynamics and sediment condition of tidal flats and cause shift of creek below the tide lock. These

studies should be strengthened in the future.

Acknowledgements

This study was supported by the natural Science Foundation of Zhejiang Province (Y505032) and the Ningbo Natural Science Foundation (2006A610077).

References

[1] ZHANG Renshun, CHEN Caijun. Evolution of Jiangsu offshore banks and probability of Tiaozini sands merged into mainland, Beijing: China Ocean Press, 1992, 1-12.

[2] ZHANG Renshun. Relation between changes of submarine sand ridge field and development of coast near Jianggang, Jiangsu, *Journal of Nanjing University (nature science)*, 1984, 20(2): 369-380.

[3] ZHANG Renshun. Evolution of tidal channel and its neighboring mud flat under the action of tidal current. *The Ocean Eengineering*. 1986, 4(4): 84-94.

[4] ZHANG Renshun. The influence of tidal inning on tide lock drainage. *Journal of Nanjing normal University (nature science)*, 1995, 18(2): 89-94.

滩涂匡围海堤选线对邻近涵闸排水的影响分析

——以条子泥西侧岸滩仓东片匡围为例

李加林[1]，王艳红[2]，张忍顺[3]

(1. 宁波大学人民环境研究所，浙江 宁波 315211；2. 南京水利科学研究院河流海岸研究所，江苏 南京 210024；
3. 南京师范大学海洋与滩涂研究所 江苏 南京 210097)

摘 要：淤泥质海岸后方大面积的低地平原主要通过海岸上建设的涵闸排水，潮滩匡围对沿海涵闸排水的影响是围垦工程必须解决的问题。文章以条子泥西侧岸滩仓东片匡围为例，探讨了不同堤线方案下邻近闸下流槽各种落潮水量组成及其维护闸下排水能力的有效性。结果表明，合理的滩涂匡围堤线方案，在平均潮汛及一般大潮汛时对邻近闸下排水能力影响较小，而在风暴潮或秋季大潮汛时有一定影响，但可以通过若干次冲淤保港来解决。

关键词：滩涂；匡围；涵闸；排水；影响

Feasible Rate of Tidal Flat Reclamation
—— Jiangsu Mud Coast as a Case Study

WANG Yanhong [1], Li Jialin [2], WANG Jian [3], ZHANG Renshun [3]

1. *River and Harbor Department, Nanjing Hydraulic Research Institute, Nanjing* 210024, *Jiangsu, China;*
2. *Institute of Human Inhabiting Environment, Ningbo University, Ningbo* 315211, *Zhejiang, China;*
3. *School of geography science, Nanjing Normal University, Nanjing,* 210097, *Jiangsu, China*

Abstract: Reclamation of tidal flat is one of the main ways to get a dynamic balance of the total amount of plowland. With the development of social economy and the increasing demand for plowland, the contradiction between tidal flat reclamation and environment protection becomes more and more outstanding. However, tidal flat reclamation should also follow the dynamic balance of total amount of tidal flat amount. The paper analyzed the history of reclamation and development of Jiangsu mud coast, and calculated the feasible rates of tidal flat reclamation on different stretches respectively, and pointed out that both the economic social benefits of reclamation and the natural erosion-accretion conditions of the coasts should be taken into consideration in deciding the intensity of tidal flat reclamation, so as to satisfy demands on both reclamation and protection of tidal flat resource.

Keywords: mud coast; mud flat; reclamation

Introduction

As a member of wetland class, the coastal tidal flat is one of the most important natural resources of Jiangsu Coast. Reclamation of tidal flat is a main approach of keeping a dynamic balance of gross farmland all the while in Jiangsu Province. However, with the developing of economy and increasing of farmland demand, reclamation of tidal flat is tending to be enhanced gradually. In the past two decades, newly reclaimed area of tidal flat is between 2 000 and 2 667 hm^2 annually on the average, but the amount from 2000 to 2005 is more than 6 667 hm^2 annually [1]. Meanwhile, more and more attention begins to be paid to the negative impacts of reclamation on the coastal environment. And the contradiction between farmland demand and coastal wetland reservation is increasingly extruded.

However, it's difficult to build an exact relationship of comparison between the socioeconomic benefit after reclamation and the ecological value before reclamation. Gain and loss of reclamation are hard to estimate. But, to stop reclamation completely is hardly possible. From the angle of protecting the present tidal flat, the paper reviewed the history of reclamation, analyzed the erosion and progradation condition of tidal flat of Jiangsu Coast, so as to seek feasible reclamation rates for different coastal stretches based on the premise of keeping a stable tidal flat condition.

Received on September 15, 2006

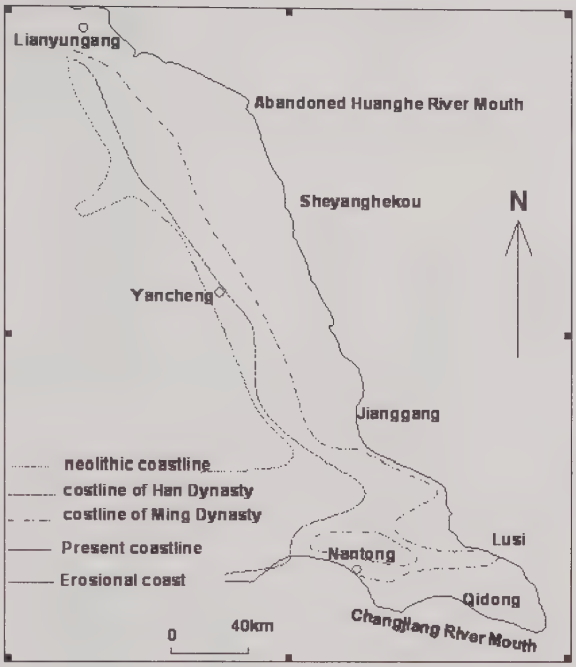

Fig.1 Historical change and present condition of Jiangsu coast

1 History of evolution and erosion and progradation dynamics of Jiangsu Coast

Jiangsu Coast, with more than 900 km of coastline, extends from the Xiuzhenhe River Mouth (boundary of Jiangsu Province and Shandong Province) in the north to the north branch of Changjiang River Mouth. Both of the two biggest rivers of China, the Changjiang River and the Huanghe River, nourished the Jiangsu Coast historically. Abundant sediment supply changed the property of the coast from sandy to muddy, built a broad coastal plain and provided substance for tidal flat progradation [2]. Because of this, about a quarter of the tidal flat area in China is distributed in Jiangsu province.

1.1 Coast progradation historically

During the past 7 thousand years, Jiangsu coast was generally prograding, and the accretion rate was 0.1 to 10cm per year. The advance rate of the coastline increased gradually. According the coastline movement (Fig. 2), progradation rates could be estimated as 9-13 m/a, 20-33 m/a and 49- 85 m/a since 6 000 years, 2 000 years and 500 years respectively.

With the lower reaches of Huanghe River shifting back to nourish the Bohai Sea and the Changjiang River Mouth moving southward gradually, the north Jiangsu coast lost foreign sediment supply greatly, and the coast entered a period of adjustment [3, 4]. However, the dynamic condition of different coastal sections varies greatly, the abandoned Huanghe River Delta coast was eroded heavily, and the tidal flat area was minimized after erosion. But some stretches, especially in the middle part of Jiangsu coast

sheltered by the offshore radiant sand ridges are still keep prograding, and the totality of coastal mud flat is increasing (Fig. 2) [5]. However, since 1949, much of the coastal mudflat has been occupied by reclamation, and reclamation has become an important factor that impacted the area change of tidal flat. And the costal mudflat evolution has been largely impacted by human activity directly or indirectly in the recent decades.

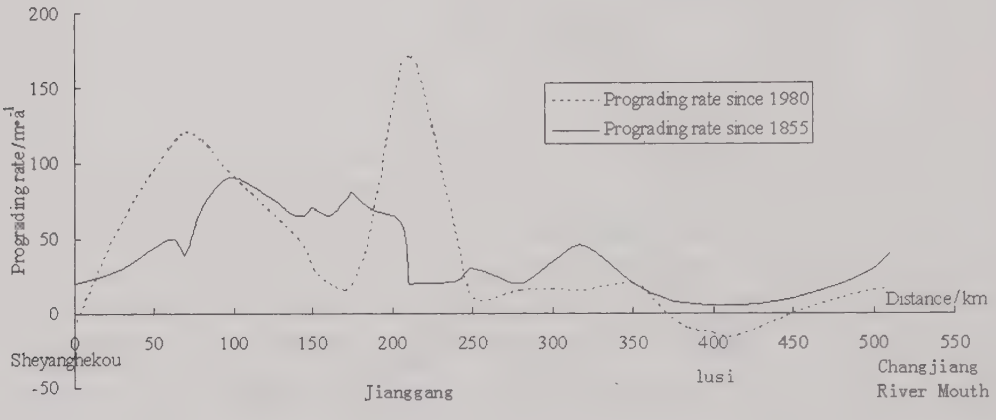

Fig. 2 Prograding rates of Jiangsu tidal flats presently and since the Huanghe River shifted back to the Bohai Sea in 1855

2 Current condition of tidal flat utilization on the Jiangsu coast

Jiangsu has a long history of coastal mudflat utilization, about 2 million hm^2 mudflat has been reclaimed since the Fan Seawall was built in the 11th century. After the People's Republic of China was founded in 1949, the large-scale reclamation could be divided into the following periods: the first is during the 1950s and 1960s, a new seawall was built along the whole coastline, and 354 thousand hm^2 mudflat was reclaimed beyond it; in the 1970s, many coastal towns were built through reclamation and immigration, but most of the reclaimed area was used for grain, cotton and salt production; in the late 1980s, the means of utilization of reclaimed mudflat transferred from the traditional use to the scientific development, from a single-crop economy to a diversified economy, from raw material production to multilevel processing and from a domestic-oriented economy to an export-oriented one. By the end of the 1980s, merchandise production and export bases of grain, cotton, fruit and fishery were formed in the reclaimed areas. By the end of the last century, more than 160 pieces of mudflat were reclaimed, more than a half million hm^2 salt land was turned into fertilized farmland inside of the old seawall. Meanwhile, about a quarter million hm^2 tidal mudflats were reclaimed outside of the old seawall.

Most of the newly reclaimed areas are used for farming, fishery, salt production, and a small portion is left for seaport use (Figs. 3, 4 and Tab. 1). Meanwhile, about 15 thousand hm^2 of reclaimed area has not been developed by now, because of the lack of auxiliary infrastructure [1].

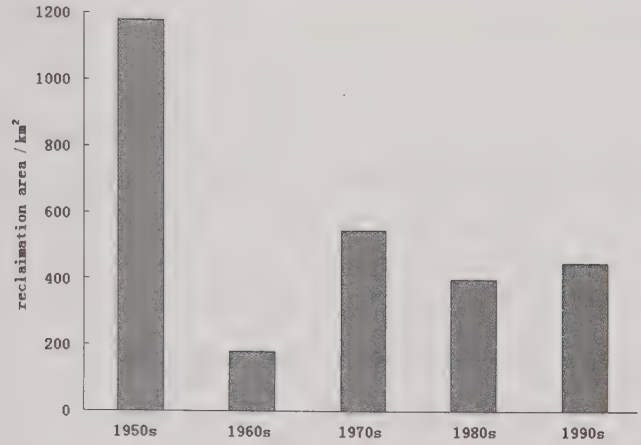

Fig. 3 Reclaimed areas of tidal flats in the recent 5 decades

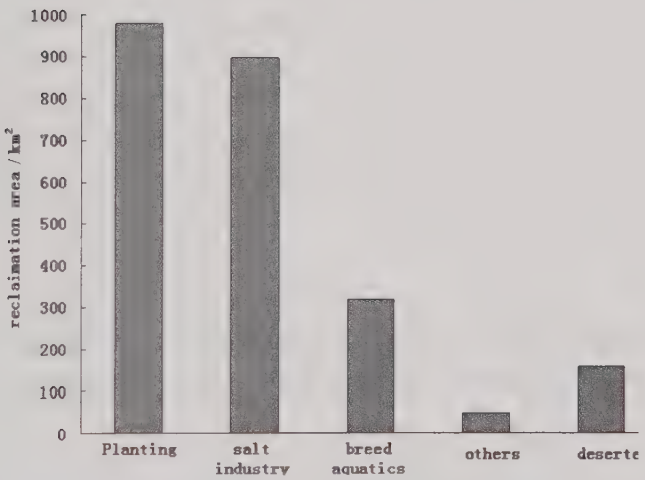

Fig. 4 Use condition of reclaimed area since 1949

Tab.1 Construction of Jiangsu coastal mudflat (10^4 hm^2)

Citys	Supra-tidal			Intertidal	Offshore sand ridges	Sum	Percentage / %
	Reclaimed	Unreclaimed	Sum				
Nantong	1.86	0.14	2.00	11.34	6.67	20.01	26.24
Yancheng	13.34	3.40	16.74	16.14	12.67	45.56	29.76
Lianyungang	8.14	0.53	8.67	2.00	0.00	10.67	14
Total	23.35	4.07	27.42	29.48	19.37	76.24	—
Percentage /%	30.63	5.34	35.96	38.67	25.37	—	100

3 Feasible rate of reclamation

The goal of mudflat reclamation is to keep a dynamic balance of gross farmland. However, the demand for farmland is far more than the natural increase in mudflat area. As a result, intemperate reclamation decreased the mudflat area gradually. A feasible rate of reclamation should also consider keeping a dynamic balance of the gross mudflat area, so as to maintain sustainable utilization and proper reservation of mudflat.

3.1 Relationship between mudflat prograding and feasible reclamation rates

Because of different regional natural conditions, the means of utilization and the benefits after reclamation are different. Tidal flat surface heights of the outer lines of reclaimed areas always differ. When the full recovery of mudflat after reclamation is considered, the time interval of reclamation (continuing to reclaim the same area of mudflat reclamation based on the same surface height of outer line of the reclaimed area) on the same stretch of coast depends on the natural increase rate of tidal flat. According to the natural condition of mudflat increase on the Jiangsu coast, the increase of mudflat on the prograding coast appears as both accreting vertically and horizontally. As a result, the gradient of cross shore tidal flat profile changed slightly during prograding (Tab. 2). Based on this, self-restoration of the tidal flat could build the same landform as before during a certain period after reclamation. Then the period could be estimated by the following expression:

$$a = \triangle H / R \qquad (1)$$

Where a is the period of self-restoration in years, $\triangle H$ is the difference of heights between the outer line of the newly reclaimed area and the old seawall foot on tidal flat, and R is the vertical accretion rate of the tidal flat on the average.

If a synchronization of vertical and horizontal accretion rates is considered, the equation (1) could be expressed as:

$$a = WG / R \qquad (2)$$

Where W is the width of reclaimed area, and G is the gradient of cross shore profile of the mudflat.

Meanwhile, the supra-tidal area is out of reach of the normal tidal circle, so reclamation of it could not greatly impact the recovery of intertidal flat. And with the enhancement of reclamation, few supra-tidal flats are left out of the seawall currently [6, 7]. Therefore, reclamation and recovery of supra-tidal flats are not discussed in the paper.

3.2 Dynamic condition and feasible rate of reclamation of mudflat on the Jiangsu coast

According to the average accretion rates of different coast stretches and the equations (1) and (2), the recovery period and feasible reclamation rates could be obtained (Tab. 2). Fig. 5 and Tab. 2 show, it is a long period for tidal flat to recover to the same condition as before the reclamation, and the feasible rate

of reclamation is very low. It will take about six yeas for recovery after a 1 km width reclamation was executed even on the quickest progtading coast stretch of Jianggang. However, the actual rate of reclamation is far more higher than the feasible one. The height of outer line flat of newly reclaimed area became lower and lower. Taking Qidong coast for example, in the 1970s, the lowest heights of reclaimed flat were around 4.0 m, but the figure declined to 3.7 m in the 1990s. And in 2004, when the Datang Lusi Port Power Station reclamation engineering was executed, the height was minimized to lower than 3.0 m.

Tab. 2 Erosion-accretion condition and feasible rate of reclamation of intertidal mudflat on Jiangsu coast

Stretches of coast	Prograding rates / $m \cdot a^{-1}$	Vertical accretion rate / $cm \cdot a^{-1}$	Profile gradient / %	Recovery period after 1 km width of reclamation / a
Sheyanghekou—Xinyanggang	13	0.42	0.032	76
Xinyanggang—Doulonggang	31	0.78	0.025	32
Doulonggang—Simaoyou	32	0.83	0.026	31
Simaoyou—Wanggang	32	0.80	0.025	31
Wanggang—Zhugang	59	2.07	0.035	17
Zhugang—Chuandonggang	59	1.48	0.025	17
Chuandonggang—Dongtaihekou	68	1.56	0.023	15
Dongtaihekou—Liangduohezha	54	1.46	0.027	19
Liangduohezha—Sancanghekou	180	4.32	0.024	6
Sancanghekou—Xinbeilinkou	120	4.68	0.039	8
Xinbeilinkou—Xyaiyangkou	33	1.39	0.042	30
Xiaoyangkou—Dongangang	37	1.26	0.034	27
Dongangang—Yaowanggang	21	0.90	0.043	48
Yaowanggang—Tuanjiegang	40	1.64	0.041	25
Tuanjiegang—Dongzaogang	1	0.04	0.040	1 600
Dongzaogang—Haozhigang	-6	-0.29	0.048	—
Haozhigang—Tanglugang	9	0.31	0.034	114
Tanglugang—Xiexingang	25	1.10	0.044	40
Xiexingang—Lianxingang	45	1.40	0.031	22

4 Conclusion

High intensity reclamation and development of tidal flats caused loss of supra-tidal flats on most of Jiangsu coast stretches. The pattern of coastal tidal flat was fundamentally transformed. Enhancement of

management is imperative under the situation. However, as a main source of farmland, reclamation of mudflat has played a great role in the economic and social development of Jiangsu Province. The contradiction between land demand and coastal environment conservation is urgently to be relaxed. According to the current condition of erosion and progradation on the Jiangsu mud coast, the following options are advanced: (1) Due to regional diversities on the economic development condition, imminence of demand for farmland, approach of utilization of reclaimed area, erosion and progradation condition, and endurable reclamation intension, the activity of reclaiming should consider both the socioeconomic benefits of reclamation and the natural coastal dynamic condition; (2) The dynamic balance of farmland gross area should be based on the precondition of the dynamic of balance of tidal flat gross area; (3) The lowest height of reclaimed tidal flat tends to be lowered in the recent years, actions of reclamation have exceeded the endurable intensities for most of the coast stretches. Therefore, tidal flat reclamation should be strictly controlled; (4) Projects with large-scale land use should be transferred to the middle part of Jiangsu coastal region with a fast prograding rate; (5) Sedimentation promotion engineering is necessary after reclamation in order to shorten the period of recovery of tidal flat.

References

[1] Bureau of Agricultural Resources Developing of Jiangsu Province, Jiangsu coastal reclamation area [Z]. Ocean Press, 1999, Beijing.

[2] Ren Mei'e. Integrated investigation on Jiangsu coastal zone and tidal flat (Report) [R]. Ocean Press, 1986, Beijing.

[3] Zhang Renshun, Lu Liyun, Wang Yanhong. Mechanism and tendency of Jiangsu coast erosion [J]. Geography Research, 2002, 4: 469-478.

[4] Wang Yanhong, Zhang Renshun et al. Dynamic and formation mechanism of muddy coast [J]. Ocean Engineering, 2003, 2: 67-71.

[5] Zhang Renshun, Wang Yanhong et al. Primary study on the process of sand island formation on off shore radiant sand ridges of Jiangsu coast [J]. Marine Bulletin, 2003, 22(4): 41-47.

[6] Wu Shuliang and Cai Xeqiang. Remote sensing analysis of the coastal shoal and tidal intet development in Jiangsu Province [J]. Marine Bulletin, 2003, 22(2): 60-68.

[7] Liu Yongxue, Limanchun and Zhang Renshun. Approach on the Dynamic change and influence factors of Spartina Slterniflora Loisel salt-marsh along the coast of the Jiangsu Province, Wetland Science, 2004, 2: 116-121.

海岸滩涂围垦的适宜速度研究
——以江苏淤泥质海岸为例

王艳红[1]，李加林[2]，王建[3]，张忍顺[3]

（1. 南京水利科学研究院 河流海岸研究所，江苏 南京 210024；2. 宁波大学 人居环境研究所，浙江 宁波 315211；
3. 南京师范大学 地理科学学院，江苏 南京 210097）

摘 要：滩涂围垦是基础设施建设占用大量耕地情况下江苏省实现耕地总量动态平衡的主要途径之一，随着社会经济的发展和对土地需求量的不断增加，滩涂围垦与海岸带环境保护之间的矛盾日渐突出。但以实现耕地总量动态平衡为目的的滩涂围垦需要以滩涂总量动态平衡为前提才能保证滩涂资源的可持续利用。通过对江苏海岸的发育和围垦历史以及淤蚀动态的分析，提出以滩涂总量动态平衡为前提的滩涂围垦适宜速度，并对江苏海岸不同岸段的适宜围垦速度进行计算分析，提出围垦活动的强度应当同时综合考虑围垦后的经济和社会效益与拟围滩涂所在岸段的自然淤蚀状况（即滩涂的承载力），以实现同时满足围垦活动与滩涂资源保护的平衡。

关键词：淤泥质海岸；滩涂；围垦

Progress in Studies on the Equilibrium Shape of Headland-bay Shoreline

LI Zhilong [1, 2], CHEN Zishen [1]

1. Department of Water Resources and Environment, Zhongshan University, Guangzhou 510275, Guangdong, China;
2. Hunan Business College, Changsha 410205, Hunan, China

Abstract: Research on the laws controlling the shoreline equilibrium shape has been one important topic of studying the evolvement and stabilization of sandy coasts. After a brief review of the progress on the equilibrium shape laws research, five models are introduced in detail. Advantages and disadvantages of these models are then discussed, which leads to the conclusion that the empirical formula integrating with analysis of mechanism should be the future direction of study on the headland-bay equilibrium shape laws. Finally, the importance of the study on the equilibrium shape of headland-bay in China is also discussed.

Keywords: headland-bay; equilibrium shape model; shoreline evolution

Introduction

Coast evolvement has an important impact on the social and economic development in coastal zones. As a consequence, research on the laws controlling the shoreline equilibrium shape has been one important topic of studying the evolvement and stabilization of sandy coasts. Discovering and applying these laws makes it possible to predict the ultimate erosion and deposit status of shorelines, hence it provides critical scientific basis for coastal resources exploitation and utilization, coastal engineering, and coastline protection.

Headland-bay beach is a ubiquitous feature on both exposed and sheltered sedimentary coasts containing headlands, which represent about 51 % of the world coastlines (Short and Masselink, 1999) [1]. Sandy beaches bounded by headlands usually develop asymmetric curvature shapes under joint processes of waves and alongshore or offshore streams. According to their planar shapes, researchers have grouped them into several categories and named them correspondingly, e.g. *Zeta- curved bay* (Halligan, 1904) [2], *Half-heart shaped bay* (Silvester, 1960) [3], *Logarithmic spiral beach* (Yasso, 1965) [4], *Crenulate shape bay* (Silvester and Ho, 1972) [5], *Curved or hooked beach* (Rea and Komar, 1975) [6], *Pocket beach* (Silvester et al., 1980) [7], and so on.

Although headland-bay beaches often exhibit various shapes, they still share some common features. If taking into account the causes of beach shape formation, a headland-bay beach can be divided into two major parts (as shown in Fig.1): 1) Shadow zone, which is a cloaked region of the upper headland. Prevalent waves diffracted by the headland and refracted by the beach often erode the beach in

Received on October 10, 2006

this region into a concave shape; 2) Tangential zone, which is a straight line region of the lower coast. Shoreline in this region is often parallel to prevalent wave fronts (Silvester, 1974) [8].

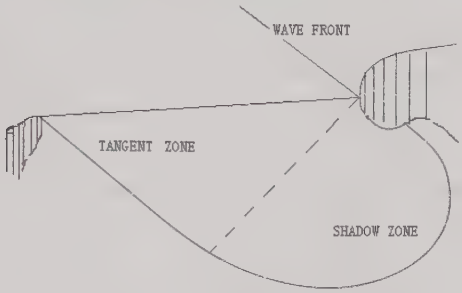

Fig. 1 The structure of headland-bay beach

In addition to the shape difference, the stabilities of sandy beaches are also different. In terms of beach stability, headland-bay beaches can be classified as *Static equilibrium beaches, Dynamic equilibrium beaches*, and *Unstable beaches* (Hsu, 2000) [9]. When a beach reaches its static equilibrium status, waves approach perpendicularly to the shoreline, breaking simultaneously. Consequently, there is no alongshore component of the incoming wave energy, which leads to an almost zero alongshore sediment transporting. At this stage, there is no long-term erosion or deposition within the embayment. However, if a beach reaches its dynamic equilibrium status, there will be a certain angle of the breaking waves approaching the shoreline. This will induce alongshore currents and alongshore drift, at the same time, there could be alongshore sediment transported from the upper coast or river to the lower coast. Littoral drift and sediment supply may reach a dynamic balance, hence maintaining a dynamic stable shoreline. When conditions of a dynamic equilibrium bays change, such as disturbance to the continuity of littoral drift, wave sheltered by coastal structures and reduction in the sediment supply from river, the balance between littoral drift and sediment supply will be broken and beaches will be eroded or accumulated. It is at this time that the beach is in its unstable stage. Because a headland-bay beach in static equilibrium was suggested as the most stable one, such a beach's structure has been recommended as the ultimate form of a stable shoreline.

1 Laws of coast evolvement and the proposing of the planar equilibrium shape model

Earlier studies on coastline shapes mainly focused on explaining their evolvement mechanisms in the view of underlying driving forces (Johnson, 1919; Davies, 1958, 1960) [10-12]. Under impacts of waves, coast will suffer erosion and retreat toward inland. If only the long-term change in erosion and accumulation is considered and the seasonal beach surface adjustment is ignored, change in shoreline position can be calculated from the sediment transporting equation

$$\frac{\mathrm{d}y}{\mathrm{d}t} = -\frac{1}{\mathrm{d}}\frac{\mathrm{d}S}{\mathrm{d}x} \tag{1}$$

Where, S is the alongshore sand-transport. Sand is assumed to be transported alongshore by the action of breaking waves. The empirical formula for the alongshore sand-transport is (Komar, 1985) [13]:

$$S = K(EC_n)_b \sin\alpha_b \cos\alpha_b \quad (2)$$

Equation 1 indicates that the change rate of shoreline position (dy/dt) is determined by the alongshore change rate of sand-transport (dS/dx). If dS/dx is positive, which indicates that the sand-transport increases along x, then dy/dt is negative, which means that shoreline will be eroded and will back off. Otherwise, if dS/dx is negative, dy/dt will be positive, which indicates that there will be sediment accumulated on the shore. On the other hand, if S remains constant, then dS is 0 and dy/dt is also 0, shoreline is stable.

Based on Eq. 1 and Eq. 2, theoretically, the shoreline location can be obtained at anytime. However, because the factors controlling the alongshore sand-transport S are very complicated, it is usually impossible to obtain an analytical resolution of Eq.1. On the other hand, numerical resolutions often induce large errors at big temporal and spatial scales. For these reasons, some researchers have proposed several empirical functions to simulate the shoreline planar form of headland-bay beaches through studying numbers of prototype beaches and laboratory simulations.

2 Equilibrium shape models of headland-bay beaches

Jennings first recognized the crenulate-shaped bay as a stable physiographic feature in 1955 (Jennings, 1955) [14]. Davies discovered the importance of wave refraction (Davies, 1958) [11]. Le Blond derived equations for littoral drift and showed that the resulting shoreline became a spiral shape in the shadow zone of the upper coast headland, but could not explain why (Le Blond, 1972) [15]. But, later he confirmed that result by calculating the arrival time of waves diffracting around the headland as shallow water waves breaking simultaneously around the periphery (Le Blond, 1979) [16]. Yasso proposed the logarithmic spiral model at first through fitting a lot of prototype bays .

2.1 Logarithmic spiral model

The logarithmic spiral bay shape equation is:

$$R_2/R_1 = \exp(\theta \cot\alpha) \quad (3)$$

Where, θ is the angle between R_1 and R_2, which are polar radii; α is the logarithmic spiral parameter, which is confirmed by obliquity of the incident wave, β. The coordinate systems are polar coordinates, where the upper coast headland B is apex and the axis is parallel to the wave front (as shown in Fig. 2).

The proposing of logarithmic spiral model provided a new way to study laws of equilibrium shoreline shapes. Results form the Logarithmic spiral model match well with prototype bays in the shadow zone of the upper coast headland, whereas, they deviate from prototype bays at the lower coast end and the

smaller the β, the larger the deviation (Hsu and Silvester, 1989)[17]. Rea and Komar commented that to make the modeled curve match well with the prototypes, the theoretical center derived from the model must be shifted (Rea and Komar, 1975)[6]. Xia pointed out that not only its centre didn't match the point where diffraction takes place, but also there was large deviation between the logarithmic spiral curve shape and that of those prototypes. For these reasons, and maybe others, it was difficult or even impossible to apply the model in real life (Xia, 1988)[18].

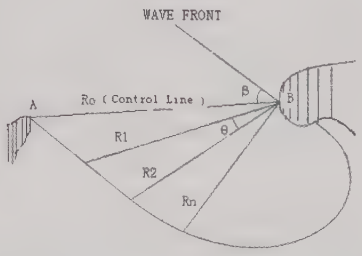

Fig. 2 The model factor of equilibrium beach

2.2 Shape-factors relation model

Comparing the shape factors of some prototype and model bays, Hus, Silvester and Xia obtained function curves that satisfied the relationship between shape factors and plotted them in diagrams. These curves serve as criteria to tell the static equilibrium status of a beach.

2.2.1 R/R_0 and θ Relation model

Polar coordinate system is used here. Upper coast headland, where wave diffraction happens, is the polar original point and the wave front is the polar axis. R_0 is the length of control line, R is the discretional polar radii, θ is the corresponding polar angle with R. Applying shape-factors data of prototype and model bays, functional relation curve of R/R_0 and θ can be obtained for the corresponding obliquity of the incident wave β (Fig.3).

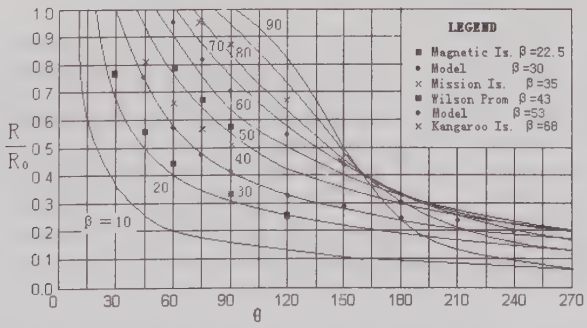

Fig. 3 Arc ratio R/R_0 versus radius angle θ for specific obliquity

The data extended over β =22.5° to 72°, which covers most natural bays. The lines have been extrapolated down to β =10° and up to β =90° in the model. We can apply it as the criterion of stability. If a beach's shape factors fall on the curve from the model, the bay is an equilibrium bay, otherwise it is unstable.

2.2.2 a/R_0 and β relation model

a is the largest bay indenting ratio, i.e. the largest distance from the control line to the bay. β is the obliquity of the incident wave. Their functional relationship was showed in Fig. 4. Similarly, if a beach's shape factors fall on the curve from the model, the bay is an equilibrium bay, otherwise, if they fall under the curve, the bay is being eroded. Dai applied the criterion to test the stability of 34 headland bays in South China (Dai, 2004) [19].

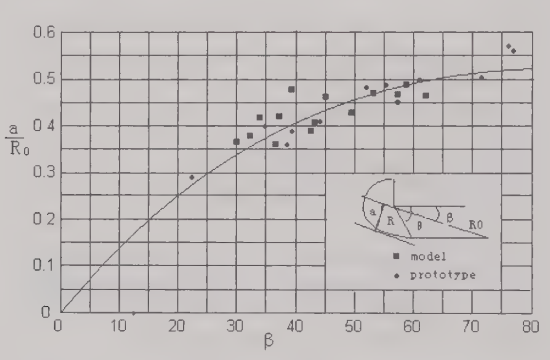

Fig. 4 Indentation Ratio a/R_0 versus Obliquity β

2.3 Hyperbolic model

Through experiments on the formation of equilibrium bays, Xia found that the shapes of equilibrium bays were completely alike among all cases with different incident wave angles. By analyzing the experimental data, Xia obtained a new static equilibrium shoreline function (Xia, 1988) [18]:

$$R^m \cdot \theta = K, \quad \text{or} \quad (R/a)^m \cdot (\theta/\beta) = 1 \tag{4}$$

Where, $m=\sqrt{2}$ (for non-static equilibrium shoreline, $m<\sqrt{2}$), R is a discretional polar radii, θ is the corresponding polar angle of R (as shown in Fig. 2). K is constant and can be expressed as:

$$k = a^m \cdot \beta$$

Where, R_0 is the length of control line, β is the obliquity of the incident wave. In the Cartesian system of coordinates, R and θ show a hyperbolic relation.

Through analyzing the data of 5 experimental bays and 9 natural bays, Xia confirmed the law. Moreover, he discussed the application of this model in the headland protection engineering (xia, 1991, 1994) [20, 21].

2.4 Parabolic model

Hsu and Evans have developed a second-order polynomial equation (namely parabolic equation) to fit the planar forms of 27 mixed cases of prototype and model bays believed to be in static equilibrium (Hsu and Evans, 1989) [17]. The equation can be expressed as:

$$R_n/R_0 = C_1 + C_2 \cdot (\beta/\theta) + C_3 \cdot (\beta/\theta)^2 \quad (5)$$

Where R_n is the discretional polar radii, θ is the corresponding polar angle of R, R_0 is the length of control line, β is the obliquity of the incident wave (as shown in Fig.2). C_1, C_2 and C_3, generated by regression analysis to fit the 27 prototypes and model bays mentioned previously, vary with the angle β (The range of angle β from 10° to 80°, which covers most natural bays). These coefficients may be expressed by fourth-order polynomials as follows:

$$C_1 = 0.0707 - 0.0047\beta + 0.000349\beta^2 - 0.00000875\beta^3 + 0.00000004765\beta^4 \quad (6)$$

$$C_2 = 0.9536 + 0.0078\beta - 0.00004879\beta^2 + 0.0000182\beta^3 - 0.000001281\beta^4 \quad (7)$$

$$C_3 = 0.0214 - 0.0078\beta + 0.0003004\beta^2 - 0.00001183\beta^3 + 0.00000009343\beta^4 \quad (8)$$

Subsequently, Silvester and Hsu produced necessary verification on this equation (Silvester and Hsu, 1993, 1997) [22, 23]. The parabolic bay shape equation has been cited in the *coastal Engineering Manual (2002)* for coastal sediment processes and shore protection projects.

Based on the parabolic model, Mauricio demonstrated the location of lower coast headland and extended the application of the parabolic model (Mauricio, 2001) [24].

2.5 Elliptic model

Prediction of the shoreline response to detached breakwaters is an important topic of studying the shoreline planar form. Detached breakwaters are the costal protecting construction parallel to and far away from shoreline. Their primary function is to protect shoreline by making wave energy dissipate and sediment accumulates. Because the hydrodynamic mechanism and sediment transport are extremely complicated along the detached breakwaters, most researchers have proposed several empirical formulas to simulate the equilibrium shoreline (Shinohara and Tsubaki, 1966, Rosen and Vajada, 1982, Mimura, Shimizu and Horikawa, 1983, Hsu and Silvester, 1990, McCormick, 1993, Ming and Chiew, 2000) [25-30].

McCormick's elliptic model is a typical one. In a Cartesian coordinate system having the origin at the center of breakwater, the equation for the shoreline is:

$$\frac{(y \mp h)^2}{a^2} + \frac{x^2}{b^2} = 1 \quad (9)$$

Where h is the distance from the center of the breakwater to the center of the ellipse, a is the semimajor axis, and b is the semiminor axis (as shown in Fig.5).

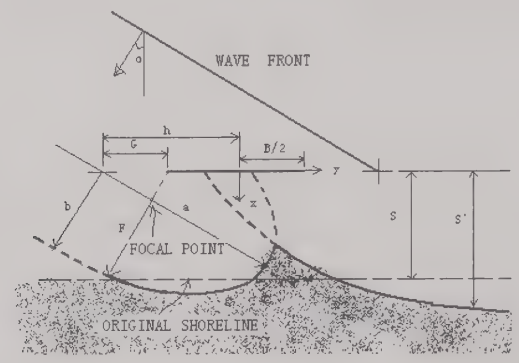

Fig.5 Elliptical shoreline response to single detached breakwater

The values of h, a, and b are assumed to depend on the deep-water wave steepness H_0/L_0, the beach slope S_b, the distance from the shoreline to the centerline of the breakwater S, and the breakwater length B. Here come the empirical equations:

$$\frac{b}{S}=1+0.2\zeta_0\sin(\chi\zeta_0) \quad (10)$$

$$\zeta=(H_0/L_0)/S_b \quad (11)$$

$$\chi=-1.92(\frac{S}{B})^2+9.92(\frac{S}{B}) \quad (12)$$

$$a=\sqrt{G^2+b^2} \quad (13)$$

$$h=G+0.5B \quad (14)$$

$$\frac{G}{b}=\exp[\ln(\mu)+\sigma\ln(\zeta_0)-\nu\zeta_0] \quad (15)$$

$$\ln(\mu)=19.4\tanh(0.91\frac{S}{B}) \quad (16)$$

$$\nu=20.0\tanh(0.99\frac{S}{B}) \quad (17)$$

$$\sigma=17.0\tanh(0.59\frac{S}{B}) \quad (18)$$

Combining Eq.9 and Eq.18, an equilibrium shoreline can be obtained. McCormick discussed the shoreline response to multiple detached breakwaters. To demonstrate its utility, the shoreline response to an 11-unit breakwater system at Bay Ridge, Md., was predicted. The predicted and actual shorelines were

shown to be in good agreement.

Hsu found more parameters having significant effects on the shoreline and modified the elliptic model (Hsu, 2003) [31].

3 Conclusions

The proposing and developing of the empirical models on the headland-bay beach planar equilibrium shape have provided the research community new thoughts and research directions to study laws of beach planar equilibrium shape. It's been almost half century since the very first Logarithmic Spiral model came into being, and models on the beach planar equilibrium shape have also evolved into their mature stage. These models not only theoretically provide new ideas and methods for researches on beaches, but also are very useful in practical applications. Predictions of static equilibrium coastlines based on models makes it is possible to avoid regions under possible erosion risks during deployment of civilian constructions in coastal zones. At the same time, empirical models on the beach equilibrium shape, especially the Parabolic model, have been widely applied in coastal engineering and have become powerful theoretical tools for coastal engineers to design economical, reasonable, and efficient coastal protection projects such as headland controlling projects, detached breakwater projects, and so forth.

However, empirical models were based on the statistical fitting; hence lack mechanism of action explanation. Although the mechanism of along-shore sediment transport has explained the mechanism of the formation of shoreline, confirmed the relationship between the shape of bay beach and the along-shore gradient of broken wave energy, stated the static equilibrium beach's characteristic that net along-shore sediment transport is zero when waves approach the shoreline perpendicularly and break simultaneously, there is still no explanation on why beaches agree with empirical equations, that is there is no mechanical explanation on why the coastline satisfies the logarithmic spiral, the 2^{nd} order parabolic functional relations. In a word, models lack of theoretical basis. Linking of mechanical analysis and empirical fitting must be the future research direction of studying laws on the planar equilibrium shape of bay beaches.

To date, there have been relative fewer researches on studying laws on the planar equilibrium shape of bay beaches. In addition to Xia's parabolic model, Chang discussed factors that affect the formation of beaches by waves through conducting the wave slot experiment (Chang, 1994) [32]; Wang explored that actions of dominant and 2^{nd} dominant waves can lead to double logarithmic spirals under the condition of monsoon (Wang, 1997) [33]. Headland-bay sandy beaches widely distribute in China, especially in southern China coasts. Recently, due to natural and human generated factors, sandy beaches is experiencing erosion and retreating. This not only provides suitable conditions for research of laws on the planar equilibrium shape of bay beaches, but also brings forward new challenges. It can be optimistic to foresee that studying laws on the planar equilibrium shape of bay beaches in China must get more and more attention from beach researchers.

Acknowledgements

This study was supported by the National Natural Science Foundation of China under the contract No. 40576041.

References

[1] Short A D, Masselink G. Embayed and structurally controlled beaches [M]. Handbook of Beach and Shoreface Morphodynamics, 1999, 230-249.

[2] Halligan G H. Sand movement on the New South Wales coast [J]. Proc. Limnology Soc. New South Wales, 1906, 619-640.

[3] Silvester R. Stabilization of sedimentary coastlines [J]. Nature, 1960, 467-469.

[4] Yasso W E. Plan geometry of headland bay beaches [J]. Geology, 73. 1965, 702-714.

[5] Silvester R, Ho S K. Use of crenulate shaped bays to stabilize coasts. Proc, 13th Inter. Conf. Coastal Eng., ASCE [C]. 1972, 1 394-1 406.

[6] Rea C C, Komar P D. Computer simulation models of hooked beach shoreline configuration [J]. Sedimentary Petrology, 1975, 866-872.

[7] Silverster R, Tsuchiya Y, Shibano T. Zeta bays, pocket beaches and headland control. Proc, 17th Inter. Conf. Coastal Eng.,ASCE [C],1980,1 306-1*319.

[8] Silvester R. Coastal Engineering, II [M]. Elsevier scientific publishing company, 1974, 71-83.

[9] Hsu J R C, Uda T. Silvester R. Shoreline protection methods Japanese experience [M]. Handbook of Coastal Engineering，New York: McGraw-Hill, 2000, 9.1-9.77.

[10] Johnson D W. Shore processes an shoreline development [M]. New York: Jone Wiley & Sons, 1919.584.

[11] Davies J L. Wave refraction and the evolution of shoreline curves [J]. Geor.Stud.,1958, 1-4.

[12] Davies J L. Beach alignment in shouthern Australia [J]. Aust.Geogr., 1960, 42-44.

[13] Komar P D. Beach processes and sedimentation. Englewood Cliffs, New Jersey: Prentice-Hall, 1976.

[14] Jenning J N. The influence of wave action on coastal outline in plan [J]. Austral.Geogr.,1955, 36-44.

[15] Le Blond P H. On the formation of spiral beaches [A]. Proc. 13th Inter. Conf. Coastal Eng. 1972,1 331-1 345.

[16] Le Blond P H. An explanation of the logarithmic spiral plan shape of headland-bay beaches [J]. J.Sedi. Petrol., 1979, 1 093-1 100.

[17] Hsu J R C, Silvester R. Member, et al. Static equilibrium bays: New relationships [J]. Journal of Waterway, Port, Coastal and Ocean Engineering. 1989, 285-298.

[18] Xia YiMing, equilibrium shape law of sandy coast [R], Nanjing Hydraulic Research Institute,1988.

[19] Dai Z J, Li C C, Zhang Q L. Fractal analysis of shoreline patterns for crenulate-bay beaches [J], Southern China, Estuarine, Coastal and Shelf Science, 2004, 65-71.

[20] Xia YiMing, study on the engineering means for coastal stability [J], The Ocean Engineering, 1991, 9(4):45-58.

[21] Xia YiMing, Headland controlling projects and equilibrium shape law [J], Journal of Hohai University, 1994, 22(1): 21-32.

[22] Silester R , Ho S K. Coastal Stabilization: Innovative Concepts [M]. Englewood Cliffs, New Jersey: Prentice

Hall,1993,578.

[23] Silvester R, Hsu J R C. Coastal Stabilization [M]. Singapore. World Scientific,1997 578.

[24] Mauricio González, Raul Mendina. On the application of static equilibrium bay formulations to natural and man-made beaches [J]. Coastal Engineering, 2001, 209-225.

[25] Shinohara, K., Tsubaki, T., Model study on the change of shoreline of sandy beach by the offshore breakwater [A]. Proceedings of the tenth International Conference on Coastal Engineering[C], ASCE, 1966, 550–563.

[26] Rosen, D.S., Vajada, M., Sedimentlogical influences of detached breakwaters[A]. Proceedings of the Eighteen Conference on Coastal Engineering [C], ASCE, (3), 1982, 130-1 940.

[27] Mimura N, Shimizu T, Horikawa K. Laboratory study on the influence of detached breakwater on coastal change [A]. Proc., Coast. Struct. [C]. ASCE, Reston, VA 83, 1983, 740-752.

[28] Hsu J R C, Silvester R, Accretion behind single offshore breakwater [J]. Journal of Waterway, Ports, Coastal and Ocean Engineering, ASCE 1990, 116 (3), 362–379.

[29] McCormick M E. Equilibrium shoreline response to breakwater [J]. Journal of Waterway, Ports, Coastal, and Ocean Engineering, ASCE 1993, 119 (6), 657–670.

[30] Ming D, Chiew Y M. Shoreline changes behind detached breakwater [J]. Journal of Waterway, Ports, Coastal and Ocean Engineering, ASCE 2000, 126 (2), 63–70.

[31] Hsu T W, Jan C D, Wen C C. Modified McCormicks model for equilibrium shorelines behind a detached breakwater [J]. Ocean Engineering, 2003, 30:1 887-1 897.

[32] Chang Reifang. The experiment research on the formation of the steady bay effected by the wave [J]. Journal of Ocean University of Qingdao, 1994, special: 62-68.

[33] Wang Wenjie. On Geomorphic-Sedimentary Features and Evolution of Spiral Bay Beaches in South China [A]. Symposium on Coastal Ocean Resources and Environment '97, 1997, Hongkong.

岬间海湾平面平衡形态研究进展

李志龙[1,2]，陈子燊[1]

（1. 中山大学水资源与环境系，广东 广州 510275；2. 湖南商学院，湖南 长沙 410205）

摘 要：岬间海湾平面平衡形态规律的研究是砂质海岸稳定与演变研究的重要内容。简要回顾了岬间海湾平面形态规律的研究进展，着重介绍了研究海湾平衡形态的五个模型。通过评述平衡形态模型的优缺点，指出机理分析和经验拟合相结合应该为以后海湾平面平衡形态规律的研究发展方向，并论述了我国岬间砂质海湾平面平衡形态研究的重要意义。

关键词：岬间海湾；平衡形态模型；海岸演变

Identification Signs and Prospects of Hydrate Gas

XU Zhenzhong [1], CHEN Shiyue [1], YANG Shuqing [2], MA Zaitian [2]

1. *College of Geo-resources and Information, University of Petroleum (East China), Dongying* 257061, *Shandong, China;*

2. *College of Marine Geology, Tongji University, Shanghai* 361005, *China*

Abstract: Gas hydrate is a kind of icy crystal body formed by water and natural gas in special conditions. The discovery of gas hydrates provides a wide sphere and a new way of thinking for finding clean and effective energy resources to replace increasingly exhausted traditional energy resources. Moreover, in our country there are a wide realm and bright prospect in the exploration of gas hydrate. This paper has summarized the progress on the study of gas hydrate. And based on the former research about gas hydrates, the integrative identification signs of gas hydrates were summarized in the aspects of seismic data, geophysical well logging, sedimentary and rock, geochemistry, topography and morphology. In the end, the author hopes it may provide some useful clues to the exploration of gas hydrate.

Keywords: integrative identification signs; gas hydrate; exploration

Introduction

The initial evidence of gas hydrate occurrence is the saturated gas hydrates coring from the exploration bore in 1967, although it was found foremost in 1778. Under conditions of STDATM, one stere methane hydrates can create one hundred sixty-four stere methane and zero point eight stere water [1]. Messoyakha is the first gas field where gas hydrates were exploitated in the world. Subsequently the drilling core containing gas hydrates was sampled from the ever frozen layer in the north of Alaska. Gas hydrates, which occur under conditions of low temperature and high pressure, is an ice-snow crystalline, in which hydrocarbon and non-hydrocarbon gases are held within rigid cages of water molecules. Gas hydrates occur in sediments of seabed in layers, dip-dyes and delfs, distributing widely in shallow (> 300 m and > 500 m) sea areas, such as continental slope, island slope, marginal sea and inland sea, and so on, of oceans in the world. There are also hydrates in the Polar Regions with high latitude, permafrost zones and deep water lake on continents, where there exist appropriate temperature and pressure environments. It was confirmed that reserves of hydrate gas was enormous on the continental slope of South Japan Sea by the drilling result in Japan from 1999 to 2000. The drilling through ODP approved that there were abundant resources of gas hydrates on the Gulf of Mexico, the Black Ridge of East Coast, and the Oregon-Cascadia Ridge of West Coast. Gas hydrates have attracted considerable attention of the Chinese geological community since 1988 [2, 3]. Chinese translated version of *Gas Hydrates* has been published [4]; An *Advance in the Research on Gas Hydrate abroad* (compiling 339 pieces of Russia and

Received on April 29, 2006

English literatures) and *Special Volume of Gas Hydrate* have been translated and edited [5]; gas hydrates were synthesized in labs of glacial frozen ground institute of Academia Sinica in 1990 [6], the application for "the research of gas hydrates in the permanent frozen ground of Qinghai-Tibetan Plateau" was proposed [7]; and Chinese Institute of Geological and Mineral Information and Mineral Bed Institute of Chinese Institute of Geology had also surveyed and studied gas hydrates and proposed suggestions of erecting items [8]. Many specialists have also paid attention to the research and exploration of gas hydrate bosoms [9-11]. That Science and Technology State of Academia Sinica formed the *21st century energy resources development strategy symposium*, the topic of which was the prospect of exploration and exploitation of gas hydrate in China, in June 1998 shows that the leaders involved prepare to regard the research and development of gas hydrates as an aspect of energy developmental strategy. Lately Shi Dou and Lei Huaiyan have thoroughly talked about research progress and exploitation prospect [12, 13]. In October 2003, in Qingdao City, more than eighty specialists and scholar from America, Canada, Gemany, Russia, the republic of Korea, India, and China took part in the symposium on the new type of energy resources in future seafloor-gas hydrate, which China Geological Survey and Earth Science Department of National Natural Science Foundation of China auspiced, and unanimously agreed that there are huge total resources of "ignited ice", which will hopefully become a new type of energy replacing oil and gas in the world. It is evaluated that the total resource of gas hydrate in oceans (with the exception of China) converted to methane is up to $(1.8\text{-}2.1)\times10^{16}$ m^3, organic carbon content of that is about two times the total resources of known coal, oil, and gas in the world [14]. So gas hydrates are generally regarded as clean energy minerals in the 21st century.

There are wide coastal areas and territorial seas and Qinghai-TIbetan Plateau claimed as the third almighty in the world in our country [15, 16]. And in the continental slope of the South China Sea alone, the resource of gas hydrates amounts to 845×10^8 t oil equivalent, which is more than that of oil and gas on land and offshore of our country [17]. It is deduced that there are huge resources of gas hydrates in wide sea area and the Qinghai-Tibetan Plateau. Moreover, it becomes an important assignment of our geological workers how to find and locate potential resources of gas hydrates. So it is of important theoretic and practical significance for the quick foundation of gas hydrates to generalize a series of synthetical identification signs of gas hydrate by use of preexisting data at home and abroad. In this article identification signs are analyzed aiming at proposing some clues to the gas hydrate research.

1 Identification sign of hydrate gas

1.1 Identification sign on the seismic section

Gas hydrates occur under specific conditions of pressure and temperature, but the temperiture-pressure gradient is quite immobile in limited regions. So the gas hydrate stability zone is limited to the regions of same depth in sea floor. There are mainly the following features.

1.1.1 The bottom-simulating reflector (BSR)

The reflection from the bottom of the gas hydrate stability zone approximately parallels the seafloor, usually being named a bottom-simulating reflector (BSR), which is the first signature of hydrate gas occurrence.

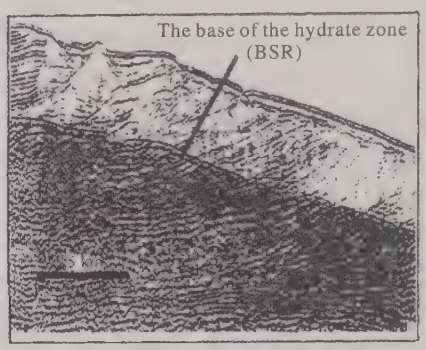

Fig. 1 BSR in a typical seismic reflection

A high-amplitude, negative polarity reflector, which approximately parallels the seafloor bathymetry, cuts discordantly across the stratigraphic section, and is irrelevant to the real sedimentary formation reflection, coincides with the base of the hydrate zone [18] (Fig.1). In addition, the hydrated layer usually displays "blanking" effects of the sedimentary section, i.e., reduced acoustic impedance contrasts caused by the cementation of the host sediments by the gas hydrate molecules. At present, BSRs are the most credible, intuitionistic and widely used indicators. This is becaused the heretofore affirmed hydrate gas in the ocean has been diagnosed from seismic sections. BSRs are generally interpreted as a very apparent transitional zone between the sediments containing gas hydrates (the P-wave velocity increase) and the underlying unhydrated strata frequently containing free gas. And in this zone there is likely free methane, as a result, the velocity of seismic wave may fall down. BSR is easily identified with the following obvious features: (1) it often parallels approximately the seafloor, and cuts discordantly across the stratigraphic section; (2) it shows a high-amplitude and negative polarity reflector as compared with the surrounding sediments, and that it is a reflective sign of interface, of which the velocity drops from high to low; (3) it presents a twig "bright trace" zone and the underlying reflection blind zone is commonly observed for the screening effect of strong reflection interface; (4) it often distributes under highland in seafloor and continental slope; and (5) its scale extends from several kilometres to several hundred kilometres.

BSRs can be used to diagnose the hydrate gas, but the following need to be noticed: (1) there does not exist the one-to-one corresponding relation between hydrate gas and BSR; (2) BSR is affected by tectonism, sedimentation, carbon contents, hydrate content ,and so on, so that both 20 % hydrated content of layers and not less than 10 % free gas content of layers beneath it are needed if BSRs can be observed; and (3) tectonic uplift, high depositional rate, high carbon content, and high hydrated content help the occurrence of BSR [19, 20].

1.1.2 Amplitude scotoma

The second feature of hydrate gas occurrence is seismic amplitude "blanking" effects, i.e., reduced acoustic impedance contrasts within the hydrated sediments, presumably due to the cementation of the stratal interfaces by the gas hydrate molecules. The effect is always observed in deposits containing gas hydrate.

The phenomenon that the seismic amplitude above BSRs is greatly reduced due to the evenly blend of deposit and hydrate continuously appears in the deposit containing hydrate gas is named blanking reflection [21]. This zone appears on the seismic data as a layer with reduced amplitudes and pronounced high velocity relative to the surrounding sediments.

1.1.3 Velocity reversal

The third feature of hydrate gas occurrence is the reversion of compressional wave velocity. That is to say, the compressional wave velocity abruptly decreases when the compressional wave spreads from a consolidated or "frozen" layer (the gas hydrated sediments) to a zone of unconsolidated sediments (under BSR).

1.2 Identification sign of geophysical logging

Now data concerned with stable zones of hydrate gas may qualitatively be acquired from several types of geophysical logging data, most of which helps qualitatively denote the hydrate gas occurrence in a specific area. In the course of drilling hydrate in NWEileenState-2 well of the Prudhoe Bay Oilfield in Alaska province, Collett T S put forward four conditions of identifying special layers utilizing geophysical logging methods [22-24]: (1) high resistivity (approximately 50 times more than water); (2) short time of acoustic waves propagating (131μs/m lower than water); (3) obvious emission of gases during the exploration drilling (the volume content of gas ranges from 5% to 10%); and (4) the features above occurring in two wells or more two wells .

Fig. 2 shows the logging curve of NWEillenState-2 core of the Prudhoe Bay Oilfield in Alaska [23]. It shows the following features in the reservoir hydrate gas occurrence (C, D, E): (1) relatively higher deviation of resistivity than the strata saturated with water; (2) relatively lower negative deviation of gamma curve than the strata saturated with water; (3) relatively lower acoustic travel time than the strata saturated with water or free gas; (4) gentle rise of neutron porosity just contrary to the strata with free gas (a marked decrease of neutron porosity); and (5) gentle decrease of density as compared with the strata saturated with water.

Tab. 1 shows the physical properties, which are measured by the ordinary well logging, of the massive hydrate, deposit containing hydrate, deposit saturated with water, and deposit containing gas. Generally because the hydrate displaces the seawater with high resistivity in hole, the resistivity from resistivity log of strata containing hydrate is greater than that of strata saturated with water. As the cement between the deposit of hole with high velocity and the particle, the hydrate stiffens the deposit, the P-velocity and S-velocity of which will increase. If there exists free gas, the value of acoustic logging and VSP-velocity will decrease, and the value of gamma, neutron porosity, and volume density well logging will

decrease by a small margin.

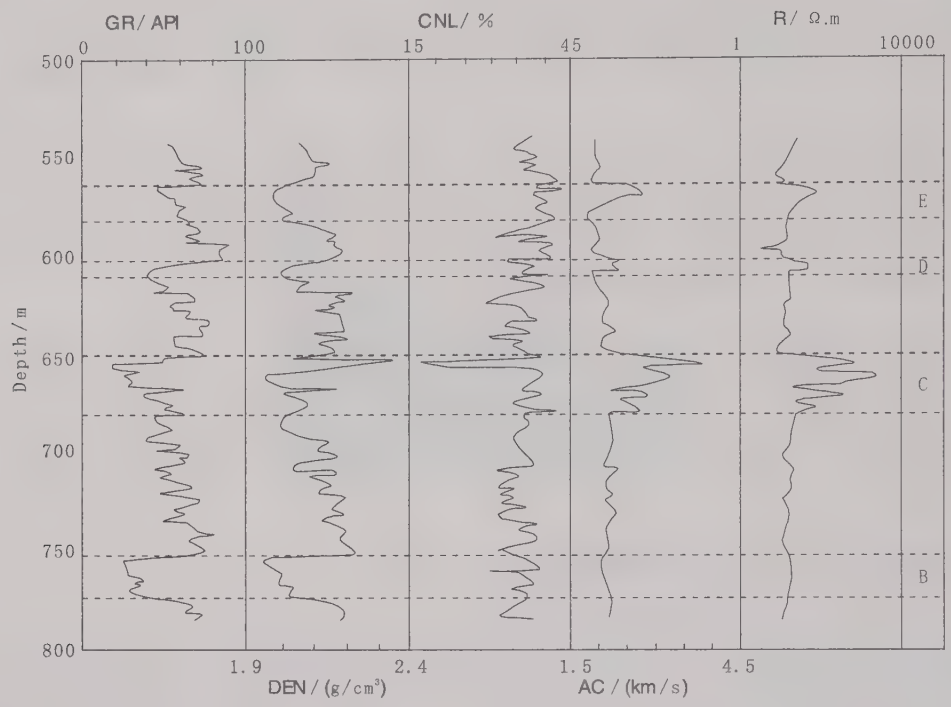

Fig. 2 Logging curve of NWEillenState-2 core of the Prudhoe Bay Oilfield in Alaska (Collett,1998)

Tab. 1 Common ranges of in situ log properties [25]

	Massive hydrate	Deposit containing hydrate	Deposit saturated with water	Deposit containing gas
V_p / km·s^{-1}	3.2 - 3.6	1.7 - 3.5	1.5 - 2.0	1.4 - 1.6
V_s / km·s^{-1}	1.6-1.7	0.4 - 1.6	0.75 - 1.0	0.4 - 0.7
R / Ω·m	150 - 200	1.5 - 175	1.0 - 3.0	1.5 - 3.5
P / g·cm^{-3}	1.04 - 1.06	1.7 - 2.0	1.7 - 2.0	1.1 - 1.5
Φ / %	20 - 50	35 - 70	35 - 70	50 - 90
γ / API	10 - 30	30 - 70	50 - 80	30 - 80

1.3 Sedimentary and lithologic identification signs

1.3.1 Composition and color

The hydrate gas found in nature generally presents white, canary, amber, and dust-colours in the form of sub-equidimensional, formational, spiculate, and scattered crystal [26-29]. It may exist in ambient temperature from below zero centigrade to above zero centigrade. Judging from the core samples

acquired, hydrate gases may occur in following forms: (1) occupation of large pore space among rock particles; (2) the spherulitic scattered in the granule rock; (3) solid filled in fissure; and (4) solid hydrate in concomitance with a little deposit.

1.3.2 Lithologic features

By far, the hydrate gas found in the sea area in the world mainly distributes in the fine graded deposit in lentoid, tubercular, particle, and flaky shapes [30, 31]. The lithology of deposit containing hydrate gas is mainly siltstone and clay. The sedimental character controls the formation and distribution of hydrate gas [32].Part of findings shows that diatom fossil is abundant in deposit from stable zones of hydrate gas [33].It is presumed that there is more hole space, which makes the hole space and permeability of deposit increases in the diatom fossil. Because the deposit with more diatom fossil occurs in the environment of palaeoclimatic optimum and higher palaeoproductivity, it is also a source of organic carbon. So lithologic features may also denote hydrate gas occurrence.

1.3.3 Sedimentation rate

Sedimentation rate, which is the main factor controlling the accumulation of hydrate gas, is generally higher than 30 m/Ma [34, 35]. Because sedimentary areas, where sedimentation rates are higher, easily form the undercompaction region, where the favorable fluid conducting system will form. This will favor the formation of hydrate gas.

1.3.4 Sedimentary environments and sedimentary facies

The sites of gas hydrate distribution suggest that many types of sedimentation of gravity flows, such as delta, fan delta, turbidity fan, slope fan, contour currents, and so on, where there are higher sedimentation rate, thick sediments accumulation, and moderate ratio of sandstone to mudstone, are the more favourable facies for gas hydrate development. High ratio of sandstone to mudstone and pore space and more pore water favour gas hydrate development. If the ratio of sandstone to mudstone is too high, the sealing ability will become weak, which is disadvantageous to the gas hydrate accumulation. As to the thickness of deposits, it is generally larger in sites with higher sedimentation rates. But in the site with the thickest deposits (sedimentary center), the ratio of sandstone to mudstone is too low, so there is little pore space and pore water, which is disadvantageous to the development of gas hydrate. Contour currents, which present the features, such as coarse grained lithologies, well pore space, ample gas source, excellent fluid migration condition, and etc, favour the development of gas hydrate, so the sites, where sedimention of contour currents is more intensive, is always the favourable area of gas hydrate concentration. Blake outer ridge is the famous area containing hydrate gas. Now it is proved that there is a close relation between the deposits containing hydrate gas and the contour currents in seafloor, and the deposits containing hydrate gas are formed by the activity of contour currents (the sedimentary rate was about 350 m/Ma) [38,39].

1.4 Geochemical identification sign

The geochemical anomalies of pore water chlorinity, oxygen isotope, and sulfate concentration

gradient in sediments prove to be excellent indicators of the presence of gas hydrates. Many successful examples show the obvious pore water chlorinity decrease, and the $\delta^{18}O_{SMOW}$ increase downward, linear and sharp sulfate gradient, and shallow sulfate-methane interface（SMI）are all the signs of gas hydrate occurrence.

1.4.1 Chlorinity in pore water of sediments

Chlorinity in pore water of sediments is one of the indicators of the presence of gas hydrates. Measurements of chlorinity for samples of gas hydrate from Guatemala offing show porewater chlorinity values of 0.051 % to 0.32 %, and that of 0.18 % to 0.82 % from Peru sea [40]. These are greatly lower than the average seawater chlorinity (1.98 %).

1.4.2 Organic carbon content in sediments

Organic carbon content in sediments is the key element of gas hydrate formation. In the littoral zone of Guatemala, organic carbon content is 2.0 % to 3.5 % in sediments containing gas hydrate [41]. In Black outer ridge, organic carbon content is 1 % on the average in sediments containing gas hydrate. So it is presumed that organic carbon content in sediments might be higher in the time of gas hydrate formation.

1.4.3 Indicator of oxidation-reduction electric potential, sulfate content, and oxygen isotope in pore water of sediments

Some indicators, such as low oxidation-reduction electric potential, low sulfate content, high oxygen isotope, and so on in pore water of sediments, may be depended on to guess the presence of gas hydrates [42, 43].

1.4.4 Typomorphic minerals

Typomorphic minerals, which can indicate the presence of gas hydrates, are generally some specially designated constituents and morphologic carbonate, sulfate, and sulfide, which are a series of typomorphic minerals which form in the interaction of mineralizing fluid with seawater, porewater, and sediments in the course of sedimentation, diagenesis, and post-diagenesis [44]. After the gas hydrate decomposes, for example, carbonate will subside. Then whether gas hydrate occurs or not may be suspected by the specially isotopic geochemical character. And that some characteristic fossil aggregations, such as the presence of Calyptogena generic mollusca occur, occur in rock is a proof of presence of gas hydrates.

In the 1990s, the discovery of authigenic carbonates minerals one after another in marine bottom sediments from offshore Oregon of western North America, the western Indian continental margins, and United Nations sea plateau of the Mediterranean, aroused people's great attention to the authigenic minerals. As a result, the distribution of gas hydrate is linked with the presence of authigenic carbonates, which serves as the symbol of gas hydrate formation. Generally, these authigenic minerals are in the form of carbonate buildup, carbonate crusts, carbonate nodules, and carbonate chimney, in associated with which there are also Mussels, Tube Shape Worms, Fungus, and Methane Air Bubble. All these are the

result of the fluid body containing wealthy methane venting upward [45]. So they often occur in clay diapirs and mud volcanos.

1.4.5 Thermoluminescence of offshore sediments

Thermoluminescence of offshore sediments is a potential method for gas hydrate exploration. As one of the nucleus-exploration technics, detection objects of thermoluminescence are typomorphic minerals generated by the formation and decomposition of hydrocarbons. The number, shape, and absorptivity of thermoluminescence peaks are not the same for the minerals which form in different enviroments. After the gas hydrate forms and decomposes, some typomorphic minerals will occur and serve as a good clue to prospecting. Moreover, some carbonate minerals, such as calcite and aragonite, are the main components of the shell of marine organisms, and there is a relation between some molluscs and gas hydrate.So the prescence of gas hydrate may be suspected by the exploration method of thermoluminescence [46].

1.4.6 Anomalously increased sea-surface temperature

During the instantaneous tectonic activities, seafloor gas hydrate and conventional gas reservoirs may decompose and vent gaseous hydrocarbon, for example, mathane, which upward migrates and diffuses to sea surface due to the pressure decrease and temperturte increase. These gaseous hydrocarbons may act as a heat-carrying agent due to the effort of instantaneous mother earth electric field and sun [47]. According to the observation of the sea-surface temperature scanned by the satellite-based thermal infrared,the seafloor gas vent may be qualitatively investigated, so that the potential regions for gas hydrate formation may be preliminarily delineated in the early stage of investigation.

1.5 Topography and morphology identification signs

Gas hydrate distributes not only in the polar zone and continental permafrost but also in the ocean floor. In-depth study shows gas hydrate is generally found in sediments from continatal slope, island slope, offshore seafloor and seamount, and marginal basins along active and passive continental margins, inland seas, and lakes [48]. Moreover there is a relation in terms of space and formation condition between gas hydrate and some specially designated typical geological structures, such as plate subduction zones, slumps, accretional wedges, clay diapirs, and so on.

1.5.1 Slip block

The development of slip block contributes a situable environment of temperature and pressure for gas hydrate occurrence. First, slump results in rapid deposits in local area, so that local pressural screening effects come into being. Then, gas hydrate easily forms if there exists ample water and gas in the interior of screening body. Moreover, the slump in itself may be the tectonic effects resulted from the decomposition of gas hydrate (As the pressure increases, gas venting from the underling stable zones makes the upper of gas hydrate break, which causes suspended deposit in the continental slope to glide along the gentle boundary).The alteration of sea level causes a series of incidents to happen repeatedly,

so that the thick chaotic melange forms in the continental slope toe [49]. During the marine regression in Late Pleistocene (about 220-170 ka), the sea level decreased by about 100-120 m, so that total pressure loadings of seafloor decreased by about 1 000 kPa. Moreover, the decrease of total pressure caused the gas hydrate to discompose, venting a large amount of methane and water and causing submarine slides. So it is guessed that submarine slides, which took place during the last glacial maximum period in the late Pleistocene, serves as an important clue to searching the gas hydrate.

In the 1980s, the large submarine landsliding relevant to the gas hydrate was found on the continental shelf in the west of Norway [50]. It was mainly made of three slides in different periods, whose total area amounts to 5 580 km^2. The scale of No.2 slide (8-5 ka), which extends from the continent slope to deep sea basins (the slippage distance exceeds 800 km and the water depth being influenced reaches 3 500 m), is the largest among the slides. It should be noted that BSR is found around the slides. Investigations show the earthquake and the decomposition of gas hydrate caused by the earthquake are the main reasons for the occurrence of the above large types of submarine slides.

1.5.2 Clay diapirs

There is a relation between clay diapirs and gas hydrate: firstly, clay diapirs itself may be the result of the sealed gas venting due to pressure release; secondly, clay diapirs can serve as the passage of gas migration upward, which helps the gas release; finally, clay diapirs can also form a local high pressure, which helps the formation of gas hydrate. Gas hydrate was found in five samples containing clayey breccia from the Sonokin Trough in the northern part of the continental slope of the Black Sea during TTR-6 Cruise of Gelendzhik (1996) [51], which demonstrates the relative relation between clay diapir and gas hydrate.

The combination of sediment loading and methane promotes the mud volcanic development and helps the evolution of clay diapirs around the detachment zone, while the accumulation of mathane results in the formation of gas hydrate [52]. So there is a close relation between mud volcano (Clay diapirs) and gas hydrate. But it should be noticed that gas hydrate does not always coincide with BSR. By now samples containing gas hydrate have been gathered from sediments in the Gulf of Mexico, Okhotsk Sea, Caspian Sea, Black Sea, Mediterranean Sea, and off Nigeria, where BSRs were not detected. The research on the distribution of gas hydrate in these sites shows gas hydrate is universally situated around the top of mud volcano and clay diapers [1].

1.5.3 Accretional wedges

The geologic body formed by the stripped sediments growing into the fault zone is named accretional wedges in the subduction process of oceanic plate with certain thickness sediment. Accretional wedges, which have a close relation to its typical mineralizational geologicl enviroment, is the commonly special structure of gas hydrate development. That gas hydrate formsa in stable shallow strata needs two preconditions: (1) The ocean crust containing organic substance is continuously stripped down and accumulates in the deformed front due to structure underplating of subducting plate, so that the deep attains the ample gas source; and (2) sediment thickening, loading increase, and tectonic compression

result in sediment dehydration, deaeration and the formation of imbricate thrust fault, then the pore fluid taking along the deep mathane quickly vents upward [53] .

2 Conclusion

a) Gas hydrates can be identified by the sign of BSR, seismic "blanking" effect, and velocity reversal in the seismic section.

b) Gas hydrate mainly shows three electric features: high resistivity (approximately 50 times more than water), short time of acoustic waves propagating (131 μs/m lower than water), and obvious emission of gases during the drilling (the volume content between 5 % and 10 %).

c) Gas hydrates mainly distribute in granule deposits in the lentoid, tubercular, particle, and flaky shapes. And that many types of sedimentation of gravity flows, such as delta, fan delta, turbidity fan, slope fan, contour currents, and so on where there higher sedimentation rate, thick sediment piles, and moderate ratio of sandstone to mudstone (35 % - 55 %), are the more favourable facies in which the gas hydrate forms.

d) Many geochemical abnormalities, such as obvious chlorinity decrease, $^{18}O_{SMOW}$ increase downward of the pore water, linear and sharp sulfate gradients, shallow sulfate-methane interface (SMI), idiographic concomitant carbonate mineral (calcium carbonate and siderite etc), thermoluminescence of offshore sediments, and anomalously increased sea-surface temperature, can all indicate the gas hydrate occurrence.

e) There is a relation in terms of space and formation conditions between the gas hydrate and some specially designated typal geological structures, such as plate subduction zones, slumps, accretional wedges, clay diapirs, and so on.

f) Gas hydrates occurrence, which cannot be judged neither only by some identity symbol, or is negated due to lack of some identity symbol, should be synthetically analyzed and judged during the exploration of gas hydrates.

References

[1] Kvenvolden K A. Gas hydrates geological perspective and global change [J]. Reviews of Geophysics, 1993, 31(2): 173-187.

[2] Chen Yongshu. Natural Gas Geology [M]. Wu Han: China University of Geology Press,1989.

[3] Xu Yongchang, Shen Ping, Liu Tianhui, et al. Theory and Application of Natural Gas [M]. Bei Jing: Scieng Press, 1994.

[4] John L (Zeng Shaoyi, Lu Deben translate).Gas Hydrates [M]. Bei Jing: Petroleum Indusrty Press,1988.

[5] Gas hydrate special [J]. Natural Gas Geoscience, 1999, 9(3-4).

[6] Shi Dou, Sun Cheng Quan, Zhu Yuenian. Research Advance of Gas Hydrate External [M]. Lan Zhou: Lan Zhou University Press, 1992.

[7] Xu XueZu, Cheng Guodong, Yu Qihao. Research prospect and proposal of gas hydrates in forever frozen area of Qinghai-Tibetan Plateau [J]. Advances In Earth Science, 1999, 14(2): 201-204.

[8] Yang Tinghuai, Liu Juhai. Resource prospect, exploration, and exploitatin of seafloor gas hydrates [J]. External Geological Science and Technology, 1998, (2): 17-21.

[9] Qin Tongluo. A few suggestion for widening resource of oil and gas [J]. Petroleum Exploration and Development, 1998, 25(4): 1-2.

[10] Qin Qinghuan. Strengthen of exploration and development of oceans and resource guarantee for the sustainable development of economy in our country [J]. External Geological Science and Technology, 1998, (2): 1-6.

[11] Wang Xianbin. Thinking and selection of energy resources exploitation [J]. Chinese Science Bulletin, 1999, 44(5): 550-559.

[12] Shi Dou, Zheng Junwei. Development situation and preview of gas hydrate in the world [J]. Advances In Earth Science, 1999, 14(4): 330-339.

[13] Lei Huiyan, Wang Xianbin, Fang Xuan, et al. Development situation and future challenge [J]. Acta Sedimentologica Sinica, 1999, 17(3): 493-498.

[14] Kvenvolden K A. US geological survey professional paper, 1993, 1570: 555- 561.

[15] Bernard B B, Brooks J M, Sachett W M. National gas seepage in the Gulf of Mexico [J]. Earth and planetary Science Letters, 1976, 31: 48-54.

[16] Galimov E M, Kvenvolden K A. Concentrations and carbon isotopic compositions of CH_4 and CO_2 in gas from sediments of the Black Outer Ridge, Deep Sea Drilling Project Leg 76[A]. Sheridan R E, Gradstein F ,et al. Initial Reports of the Deep Sea Drilling Project [C]. Washington D C : U.S. Government Printing Office, 1983: 403-407.

[17] Zhang Guangxue, Huang Yongyang, Chen Bangyan. Seismology of Gas Hydrate in Sea Area [M]. Bei JIng: Ocean Press, 2003.

[18] Shipley T H, Houston M H, Buffler R T, et al. Seismic reflection evidence for the widespread occurrence of possible gas-hydrate horizons on continental slopes and rises [J]. American Association of Petroleum Geologists Bulletin, 1979, 63: 2 204-2 213.

[19] Lerche I, Bagirov E. Guide to gas hydrates stability in various geological settings [J]. Marine and Petroleum Geology, 1998, 15(5): 427-438.

[20] Roland von Huene, Ingo A Pecher. Vertical tectonics and the Origins of BS Rs along the Peru margin [J]. Earth And Planetary Science Letters, 1998, 116(1-2): 47-56.

[21] Dillon W P, Lee M W, Felhaber K, et al. Gas hydrates on the Atlantic continental margin of the United States-Controls on the concentration [A]. Howell D G.The Feature of Energy Gases [C]. U. S. Geological Survey Professional Paper 1570, 1993: 313-330.

[22] Collett T S. Detection of gas hydrate with downhole logs and assessment of gas hydrate concentriond(saturations) and gas volumes on the Blake ridge with electrical resistivity log data [A]. In:Proceedings of the Ocean Drilling Program, Scientific Results, 164 [C]. College Station, TX, 2000.179-191.

[23] Collett T S. Well log evaluation of gas hydrate saturations [A]. SPWLA 39th Annual Logging Symposium [C].1998.

[24] Collett T S. Natural gas hydrates of the Prudhoe Bay and Kuparuk River area, North Slope,Alaska [J]. AAPG Bulletin, 1993, 77(5): 793-812.

[25] Goldberg D S, Collett T S, Hyndman R D. Ground truth: in-situ properties of hydrate [A]. In: Max, M. D. (ed).

Natural gas hydrate in oceanic and permafrost environments [C]. Klumer Acad. Publ. Dordrecht, 2000: 295-310.

[26] Zhou Huaiyang. Gas Hydrate [M]. Bei JIng: Ocean Press, 2000.

[27] Qi Xuegui, Chen Zeshao. Progress of gas hydrate investigation [J]. Natural Journal, 2001, 23(2): 79-82.

[28] Brown K M, Bangs N L. The naturee, distribution, and origin of gas hydrate in the Chile triple junction region [J]. Earth and Planetary Science Letters, 1996, 139: 471-483.

[29] Person C F, Halleck P M, McGuire P L, er al. Natural gas hydrate deposits: a review of in situ propertyes [J]. J. Phys. Chem., 1983, 87: 4 180-4 185.

[30] Brooks J M, Anderson A L, Sassen R, et al. Hydrate occurrences in shallow subsurface cores from continental slope sediments [J]. Annals of the New York Academy of Science, 1994, 715: 381-391.

[31] Ginsburg, G. Challenging the presence of natural gas hydrate in the Messoyakha pool, Poster presentation at the 1993 American Association of Petroleum Geologists Conference at The Hague, the Netherlands, 1993 .

[32] Kraemer L M, Owen R M and Dickens G R. Lithology of the upper gas hydrate zone, Blake Outer Ridge: a link between diatoms, porosity, and gas hydrate. *In* Paull C K, Matsumoto R, Wallace P J, and Dillon W P (Eds.), Proc. ODP, Sci. Results, 2000, 164, 229-236.

[33] Kraemer R R, Acevedo E O, Dzewaltowski D A, et al. Effects of low-volume resistive exercise on beta-endorphin and cortisol consentrations [J]. International Journal of Sports Medicine, 1996,17, 12-16.

[34] Kvenvolden K A & McMenamin M A. Geol. Surv. Circ.(U. S.), 1980, 825: 1-11.

[35] Claypool G E and Kaplan I R. Origin and distribution of methane in marine sediments [R]. In: Natural gases in marine sediments [C]. Plenum Press, Kalpan, I. R. (ed), 1974, 99-144.

[36] Collet T S, Ladd J. Detection of gas hydrate with down hole logs and assessment of gas hydrate concentrations(saturations) and gas volumes on the Blake Ridge with bbbb electrical resistivity log data, 1999, Proceedings of the Ocean Drilling Program [J]. Scientific Results, 1999, 164: 179-192.

[37] Matveeva T, Mazurenko L, Soloviev V, et al. Gas hydrate accumulation associated with fluid discharge structure in Lake Baikal. J EUG XI Conf Abstr, 2001, 6(1): 154.

[38] Matveeva T V and Solov'ev V A. Geological control over gas hydrate accumulation on the Blake outer ridge [J]. Geologiya I Geofizika, 2002, 43(7): 658-668.

[39] Matveeva T V, Mazurenko L L, Soloviev V A, et al. Gas hydrate accumulation in the subsurface sediments of Lake Baikal (Eastern Siberia). Geo-Mar Lett 23(3/4), 2003.

[40] Kvenvolden K A, Kastner M. Gas hydrates of the Peruvian outer continental margin .In: Suess E, ed. Proceedings of the Ocean Drilling Program, Scientific Results,Vol.112 [R]. Ocean Drilling program, College Station, Tex., 1990, 517-526.

[41] Hesse R, Harrison W E. Gas hydrates(clathrates) causing pore – water freshening and oxygen isotope fractionation in deep – water sedimentary sections of terrigenous continental margins [J]. Earth and Planetary Science Letters, 1981, 55: 453-562.

[42] Hyndman R D, Yuan T, Moran K. The concentration of deep sea gas hydrates from downhole electrical resistivity logs and laboratory data [J]. Earth and Planetary Science Letters, 1999, 172: 167-177.

[43] Kvenvolden K A, Barnard L A. Hydrates of natural gas in continental margins [A]. in Studies in Continental Margin Gelogy, edited by Watkins J S and Dralz C L, Am. Assoc. Pet. Geol. Mem., 1983, 34: 631-640.

[44] Makogon Y F. Hydrates of Natural Gas [M]. Pennwell, Tulsa, Okla, 1981.

[45] Hovland M, Gallagher J W. Gas hydrate and free gas volumes in marine sediments: Example from the Niger Delta front [J]. Marine and Petroleum Geology, 1997, 14(3): 245-255.

[46] Liu Haisheng. Thermoluminescence of offshore sediments-A potential method for gas hydrate exploration [J]. Geophysical and Geochemical Exploration, 2002, 26(4): 264-267.

[47] Lu Zhenquan, Qiang Zuji, Wu Bihao. Exploring gas hydrate by satelite-based themal-Infrared remote sensing [J]. Acta Geologica Sinica, 2002, 76(1): 100-106.

[48] Yang Tinghuai, Liu Juhai. Resouces prospect and exploration of gas hydrate in seafloor [J]. External Geological Science and Technology, 1998, (2): 17-21.

[49] Kayen R E, Lee H J. Pieistocene slope instability of gas hydrate laden sediment on the Beaufort Sea Margin [J]. Marine Geotechnology, 1991, 10: 125-141.

[50] Jansen E et al. Large submarine slides on the Norwegian Continental margin: sediments, transport and timing [J]. Marine Geology, 1987, 78(1-2): 77-107.

[51] Henriet J P, Mienert J. Gas Hydrates:Relevance to World Margin Stalitity and Climate change [M]. Geological Society, London Special Publications, 2000, 137, 215-222.

[52] Reed D L et al. Relations between mud volcanoes, thrust deformation, slope sedimentation, and gas hydrate, offshore north Panama [J]. Marine and Petroleum Geology, 1990, 7(1):44-45.

[53] Zhang Guangxue. Review of seismic investigation of gas hydrate in world sea area [J]. Marine Geology, 2001, 1: 1-18.

天然气水合物的识别标志及研究进展

徐振中[1]，陈世悦[1]，杨淑卿[2]，马在田[2]

（1. 中国石油大学（华东）地球资源与信息学院，山东 东营 257061；2. 同济大学，上海 200092）

摘 要：天然气水合物是天然气和水在特定条件下形成的一种透明的冰状结晶体。天然气水合物的发现为寻找清洁高效的新型能源，以取代日益枯竭的传统能源提供了一个广阔的领域和新的思维方式。我国天然气水合物具有广阔的勘探领域和良好的勘探前景。本文对天然气水合物的研究现状进行了综述。在总结前人关于天然气水合物研究的基础上，总结归纳了天然气水合物的地震、地球物理测井、沉积岩石、地球化学、地形地貌等识别标志。企望对加速天然气水合物的勘探提供一些有益的线索。

关键词：天然气水合物；识别标志；勘探

Marine Science Bulletin

Marine Science Bulletin publishes papers on marine science and technology including physical oceanography, chemical oceanography, marine biology, marine geology, environmental oceanography, estuarine & coastal sciences, marine technology, digital ocean, coastal zone management, ocean engineering, marine economics, etc., and aims to promote international academic exchange.

Editor-in-Chief: LIN Shaohua (林绍花)

Associate Editor-in-Chief: HE Guangshun (何广顺) YANG Ying (杨 鹰)

Executive Editor: LIN Baofa (林宝法) HE Xuewu (何学武) ZHANG Deshan (张德山)
ZHANG Xiaoxian (张潇娴) WANG Zhankun (王占坤)
CHENG Xiuchun (程秀春)

Marine Science Bulletin **(Vol. 9 No. 1 May 2007)**

Responsible Institution:
State Oceanic Administration of China
Edited and Published Semi-annually by:
National Marine Data and Information Service
Address: 93 Liuwei Road, Hedong District, Tianjin 300171, China
E-mail: msb@mail.nmdis.gov.cn

ISSN1000-9620
CN12-1271/N